CERN-THESIS-2010-277

UNIVERSITÀ DEGLI STUDI DI SALERNO

FACOLTÀ DI SCIENZE MATEMATICHE FISICHE E NATURALI
DOTTORATO DI RICERCA IN FISICA, VIII CICLO

PhD Thesis

Pb-Pb collisions in the ALICE experiment: development of tools for a study of the azimuthal anisotropy parameter

PAOLA PAGANO

Advisor:
Prof.
SALVATORE DE PASQUALE

PhD Coordinator:
Prof.
MARIO SALERNO

Salerno, Italy, 2010

To Matteo

Contents

List of Figures

List of Tables

Introduction

According to the latest cosmological theories, a few millionths of a second after the Big Bang our Universe was in a state characterized by high temperature and extremely high density. Under these conditions it is assumed that there was a state of nuclear matter called Quark Gluon Plasma in which these building blocks were free to move on relatively large distances. After 5 seconds, the temperature of the Universe had decreased enough to lead to the formation of protons and neutrons, within which are confined quarks and gluons.
To recreate and study that primordial plasma the ALICE experiment has been conceived: it currently operates at the Large Hadron Collider at CERN. With an increase in centre-of-mass energy, with respect to previous colliders, of a factor almost 30, LHC ($\sqrt{s_{Pb-Pb}} = 5.5 TeV$) is the new frontier for the study of the quark-gluon plasma. The drastic increase in energy means that LHC will create hotter and longer-lived drops of QGP matter, therefore enabling a better comparison between data and theory.
The first chapter provide an introduction to the theoretical models leading to the hypothesis of the Quark Gluon Plasma creation and to the observables that could constitute the probes of its formation. In addition a review on the latest experimental results is supplyied to each argumentation. One of the newest signature of Quark Gluon Plasma is the **elliptic flow** that, according latest experimental results, should be an evidence of partonic collectivity. In the second chapter the ALICE experiment is introduced and its setup and components are illustrated. In order to investigate the formation of this new phase of matter, a very performance apparatus is needed and, in particular, a particle identification over large part of the phase space has been an important design feature.
Chapter 3 contains the description of the largest detector system for the PID in ALICE: the Time-Of-Flight (TOF) detector. It cover a cilindrical surface of $\sim 170 m^2$ in the central acceptance region $|\eta| \lesssim 1$. The detector exploits the novel technology based on the Multigap Resistive Plate Chamber (MRPC) which guarantees the

excellent performance required for a very large time-of-flight array. The construction of the ALICE TOF detector has required the assembly of a large number of MRPC detectors which has been successfully carried out thanks to a careful mass production controlled by strict quality assurance procedures. Its performance has been succefully tested during Cosmic Rays tests and during the first operations at LHC: a first result on the resolution is presented in Chapter 3.
As before introduced, detailed elliptic flow measurements provide indispensable about high energy density matter. Such measurement are characterized by the magnitude of the second armonic coefficient v_2 of the Fourier expansion of the azimuthal distribution of emitted particles.
In particular, a measure of ϕ **meson** elliptic flow can lend unique insight on reaction dynamics because its mass is similar to that of the proton even being a meson, so its v_2 should be additive with respect to the v_2 of its two constituent quark: it should provide an important benchmark test for partonic collectivity. Chapter 4 illustrates a Monte Carlo simulation study on ϕ meson elliptic flow measurement with the invariant mass method in the ALICE experiment.

Chapter 1

Introduction to Heavy-Ion Physics

1.1 The Standard Model

The Standard Model (**SM**) is a gauge theory of three of the four known fundamental interactions, *strong*, *weak* and *electromagnetic*, - gravity has not been incorporated in the SM -, and the elementary particles that take part in these interactions. Proposed and developed since the 1960's, the Standard Model is a comprehensive theory to which apper to be consistent all the hundreds of particles and complex interactions; today it's well established thanks to a large variety of experiments that has confirmed its prediction; for example the discovery of W and Z bosons and the precise measurements on their masses.
In this model, the last constituent of matter can be classified in two groups: fermions and gauge vector bosons. The fermions are defined as elementary particles having spin of 1/2 and are divide into two families: six *quarks* (up (u), down (d), charm (c), strange (s), top (t) and bottom (b)) and six *leptons* (electron (e), muon (μ), tauon (τ), and their corresponding neutrinos), each with a corresponding antiparticle.
Pairs from each classification are grouped together to form a generation, as shown in Fig 1.1, with corresponding particles exhibiting similar physical behavior.

Quarks have a property called **color** playing the role of charge in the strong force. The color can take one out of three possible values (conventionally *red*, *green*, and *blue*). They do not appear freely: they are confined and appear associatedc in hadrons that are colorless (also called white), i.e. in the corresponding $SU(3)$-algebra the colors of the constituent quarks sum to 0. Hadrons are categorized into two families: *baryons* and *mesons*. Baryons consist of three quarks,

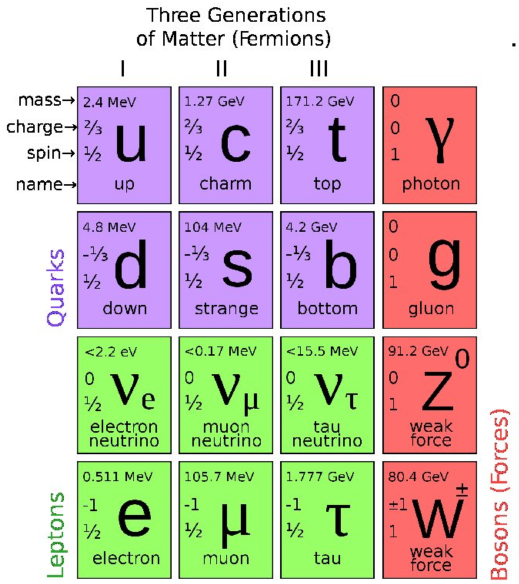

Figure 1.1: Constituent of matter in the Standard Model. [1, 2]

qqq or $\overline{qqq}$ (e.g. the proton: uud). Mesons consist of two quarks, $q\overline{q}$ (e.g. the K^{+}:$u\bar{s}$). Quarks are affected by the strong, weak, and electromagnetic force. The remaining six fermions do not carry color charge; e, μ and τ carry electric charge thus interact electromagnetically. The three neutrinos do not carry electric charge so their motion is directly influenced only by the weak nuclear force.

The forces between these fermions are mediated by the gauge vector bosons (the last column of Fig. 1.1). The electromagnetic force between electrically charged particles is mediated by photons, which is massless and well described by the theory of quantum electrodynamics (QED). The weak interactions between particles of different flavors are mediated the massive gauge bosons $W\pm$ and Z^0. These interaction is described by the electroweak theory that includes the electromagnetic force: it is the first successful theory that treats some of the fundamental forces that are different at low energies on an equal footing. The strong or color force interaction between quarks is described in terms of the gauge particles of $SU(3)$. These gauge vector bosons are 3^2- 1 = 8 and are called gluons. This multiplicity of gluons is labelled by a combination of color and an anticolor charge. Because the $SU(3)$ symmetry of the color interaction is believed to be exact, the gluons are massless particles. The effective color charge of gluons allow them to interact among themselves. The gluons and their interactions are described by the theory of **Quantum Chromodynamics** (**QCD**).

However the Standard Model has also limitations that has required extensions to keep the theory consistent. The most prominent example has been that the masses of the electroweak gauge bosons, evaluated to zero within the theory. Something that is clearly inconsistent with experiment.
This situation has been solved by an additional gauge boson added to the theory, the Higgs boson [3, 4, 5]. The Higgs mechanism generates the masses for the $W\pm$ and Z^0 while the photon remains massless. The scientific community is looking for this boson since more than two decade; the **ATLAS** and **CMS** experiments at the **LHC** will try to catch up it since this year.

1.2 Quantum Chromodynamics

Quantum Chromodynamics is the fundamental theory which describes the strong nuclear interaction [6, 7, 8].
The QCD Lagrangian is closely analogous to the Lagrangian of Quantum ElectroDynaimics **QED**, the theory which governs atomic interactions. It is given by

$$\mathscr{L} = \Sigma_q \overline{\Psi}_{q,a}(i\gamma^{\mu}\partial_{\mu}\delta_{a,b} - g_s\gamma^{\mu}t^C_{a,b}A^C_{\mu} - m_q\delta_{a,b})\psi_{q,b} - \frac{1}{4}F^A_{\mu\nu}F^{A\mu\nu} \tag{1.1}$$

where repeated indices are summed over. The γ^{μ} are the Dirac γ-matrices. The $\psi_{q,a}$ are quark-field spinors for a quark of flavor q and mass m_q, with a color-index a that runs from a=1 to N_C=3, *i.e.* quarks come in three colors. The final term, absent in QED, represents the interaction of the gluon field with itself. This term is responsible for the qualitatively different nature of matter at the subnuclear scale than at the atomic one. As mentioned anticipate, the fundamental symmetries of QCD are described mathematically by the SU(3) group. Physically, this group corresponds to a theory in which there is a quantum number which can take three values, the above introduced color flavor, the other quantum number of the theory, gives rise to the six different known quark states (labeled by the subscript q in the Lagrangian) each with a mass and (fractional) electric charge. The three lightest quarks, up, down and strange, also obey approximate SU(3) symmetry. This is responsible for the particular pattern of hadronic bound states, called the *Eight-Fold Way* by Gell-Mann [9], which inspired the parton model in which the fundamental particles are no longer the hadrons but the partons inside them. QCD has two peculiar properties: *asymptotic freedom* and *confinement*.

1.2.1 Asymptotic freedom

QCD is characterized by a scale dependent coupling: as a consequence of the gluon self-coupling, QCD implies that the coupling strenght α_s, the analogue of the fine-structure constant α in QED, becomes bigger at large distances or, equivalently, at low momentum transfers. [1]

QCD does not predict the actual value of α_s, it definitely predicts the functional form of the *energy dependence* of α_s. While an increasingly large coupling at small energy scales leads to the *confinement* of quarks and gluons inside hadrons, the coupling becomes small at high-energy or short-distance reactions; quarks and gluons are said to be *asymptotically free*, i.e. $\alpha_s \to 0$ for momentum transfers $Q \to \infty$. The effective QCD coupling constant $\alpha_s$is dependent on the renormalization scale; it can be written as:

$$\alpha_s(Q^2)) = \frac{1}{\beta_0 ln(\frac{Q^2}{\Lambda^2})} \tag{1.2}$$

The β_0 was evaluated at leading order by Gross, Wilczek and Politzer in 1973 [7]. They found that

$$b = -\frac{33 - n_f}{12\pi} \tag{1.3}$$

where n_f is the number of quark flavors at the energy scale Q. Λ is an important parameter, technically identical to the energy scale Q where $\alpha_s(Q^2)$ diverges to infinity. The α_s has to be determined from experiment: its world average value is $\alpha_s(M_Z^0) = 0.1184 \pm 0.0007$ and for the QCD scale $\Lambda = 213 \pm 9$MeV. Fig. 1.2 shows α_s at different energy scale [10].

Due to the asymptotic freedom, the QCD is handled with different energy scale. The QCD can only be calculated perturbatively in high momentum transfer or short distance approach (**pQCD**). At the strong coupling case, pQCD is irrelevant and some other methods are needed, for example **Lattice QCD** and **AdS/CFT** (*Anti-de-Sitter Space/Conformal Field Theory*).

- **pQCD**
  Since at high momentum transfer, the $\alpha_s \ll 1$ and decrease logarithmically

[1]"Large distances" Δs correspond to $\Delta s > 1$ fm, "low" momentum transfers to $Q < 1$ GeV/c

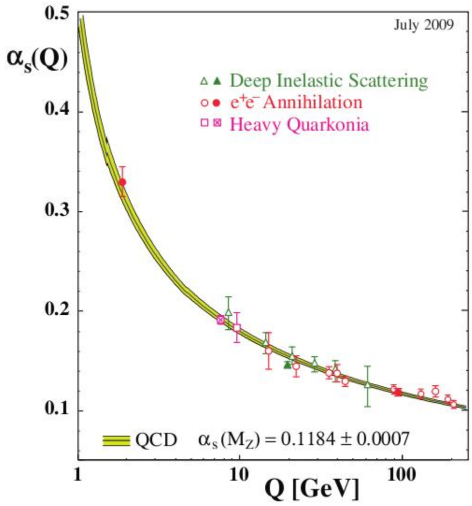

Figure 1.2: The QCD coupling, α_s as a function of the momentum scale, Q. The data is extracted from data from different observables at two different orders in perturbation theory (open and closed symbols) and compared to a purely perturbative calculation (see next paragraph). [10]

(very slowly), physics quantities, such as cross sections, can be calculated to a truncated series with different α_s dependence ($\alpha_s^{(n+2)}$). Since α_s is very small, the terms with lowest power n ($n = 0$) is usually have the largest contribution and called *Leading order* (**LO**). The higher order terms usually have smaller contribution and involves more complicate diagrams which cause the calculation more diffcult. Depend on the power n, the corrections are called *Next-to-Leading Order* (**NLO**), $n = 1$, *Next-to-Next-to-Leading Order* (**NNLO**), $n = 2$, etc. But this is only on parton level. What concern for the process on hadron level, the hadron structure which involved nonperturbative nature has to be take into account. A QCD factorization theorem was develop to calculate the cross section on hadron level, which separate the cross section into 2 parts: the process dependent pQCD calculate short distance parton cross section, and the universal long distance functions. For example, the cross section for a process $A+B \rightarrow C+...$ where A, B and C are hadrons, can be written as:

$$\sigma_{AB\rightarrow\ C} = f_{a/A}(x_a,\mu_F^2) f_{b/B}(x_b,\mu_F^2) \otimes \hat{\sigma}_{ab\rightarrow c}(\hat{s},\mu_F^2,\mu_R^2,/alpha_s) \otimes D_{c\rightarrow C}(z,\mu_F^2) \tag{1.4}$$

Only the middle term $\hat{\sigma}_{ab\rightarrow c}$, the parton cross section, can be calculated in pQCD from Feynman diagrams.
The first term $f_{a/A}(x_a,\mu_F^2)$ or $f_{b/B}(x_b,\mu_F^2)$ is the hadron *Parton Distribution Function* (**PDF**) and the last term $D_{c\rightarrow C}(z,\mu_F^2)$ is the *Fragmentation Function* (**FF**) that describes the transition from a parton to a hadron. For leptons, these two terms don't contribute in this formula.
Hence, we can measure PDFs through lepton-nucleon DIS interactions and FFs through high energy e^+e^- collisions. μ_R is the renormalization scale, originate from the need to regularize divergent momentum integrals in calculating high order diagram loops; μ_F is the factorization scale, at which the parton density are evaluated; $\hat{s}$ is the squared partonic center of mass energy.

- **Lattice QCD**
  At low momentum transfer, the QCD coupling constant α_s approach unity quickly as decreasing momentum transfer. In this case the high order processes will have large contributions and can not be neglected. The pQCD is not valid any more. Instead, the Lattice QCD is the most well established approach in this case. In Lattice QCD, space time is represented not as continuous but as a crystalline lattice, vertices connected by lines. Quarks may reside only on vertices and gluons can only travel along lines. As the spacing between vertices is reduced to zero, the theory will approach continuum QCD. As this is computationally impossible, lattice QCD calculations often involved analysis at different lattice spacing to determine the lattice-spacing dependence, which can then be extrapolated to the continuum. This technique is only applicable in the domain of low density and high temperature. At higher densities, the fermion sign problem renders the results useless. [11]

- **Other Non Perturbative QCD**
  There are some other non perturbative methods, such as 1/N expansion and Effective theories. The 1/N expansion, a well known approximate scheme, starts from the premise that the number of colors is infinite, and makes a

series of corrections to account for the fact that it is not. The **AdS/CFT** is one of the popular 1/N expansions. It is the conjecture equivalence between a string theory defined on one space, and a quantum field theory without gravity defined on the conformal boundary of this space, whose dimension is lower by one or more. In some special case, the QCD Lagrangian can be systematically expanded in some parameters. For example the heavy quark effective theory which expands around heavy quark mass near infinity. [12]

1.2.2 Confinement

In contrats with the values obtained in the regime of asymptotic freedom, it turns out that at large distances (or small momentun transfer) the strong coupling constant α_s is large. It is believed that in this regime the quark are confined in coulorless particles. [2] Confinement, as it is known, is expected to increase as the distance between two quarks becomes larger. This QCD phenomenon is responsible for the fact that hadrons have yet only been observed either as quark-antiquark pairs (known as mesons) or bound together in groups of three (known as baryons). However, QCD does not exclude the existence of other types of hadrons; such as pentaquarks (five-quark systems). From a theoretical point of view, the study of confinement is not a negligible task as hadron spectra (i.e. masses and particle widths) are governed by non-perturbative aspects of the strong interaction. At present, their description is based mainly on numerical methods inspired by QCD models. [13]

1.3 Chiral Simmetry

In addition to the onset of deconfinement, another phenomenon may become realized at high temperature: the *chiral symmetry restoration*. The chiral symmetry is the invariance of the Lagrangian under an axial transformation of the fermion field. A Lagrangian with massless fermions possesses chiral symmetry, allowing a decomposition of the quarks into independent left- and right-handed massless spin $1/2$ states, which for massive fermions become mixed. When confined in hadrons, the basic quarks *dress* themselves with gluons to acquire an effective constituent quark mass of about 300 MeV(roughly corresponding to $1/3$ of the

[2] It is not possible to derive confinement from the QCD Lagrangian; the same applies to asymptotic freedom

proton or $1/2$ of the ρ mass). This leads to a spontaneous breaking of the chiral symmetry. On the other hand, after the transition to a deconfined phase, the quarks would recover the *bare* mass appearing in the Lagrangian, and the symmetry is restored [20]. The chiral symmetry restoration is expected to affect the spectral features of the light vector mesons ρ, ω and ϕ, which therefore constitute an interesting investigation field for experiments.

1.4 Quark Gluon Plasma

At ordinary condition, the quarks are confined and can not be isolated by pulling them apart; the potential energy between the quarks increases with the distance. Once the energy is above the threshold for $q\overline{q}$-pair production, such a pair is created (see e.g. [2]). But at extreme conditions like high temperature and high energy density, the Lattice QCD predicted a phase transition from normal QCD matter to a new matter, called *Quark Gluon Plasma* (**QGP**). In this new phase, the mesons and baryons lose their identities and dissolve into a fluid quarks and gluons. Long-range interactions are screened; quarks and gluons are only subject to short-range interactions, so they can move around in a large distance rather than confined in hadrons: this condition is called deconfinement. The coupling constant at short distances is small leading to just weak coupling between the quarks and gluons. Lattice QCD calculations predict the phase transition to the QGP for the chemical potential, which measures the baryon number density, $mu_B \approx 0$ at approximately 150 MeV [14] to 190 MeV [15] and at energy density of $\varepsilon \sim$1GeV/fm^3.
In order to describe the transition to QGP, an heuristic approach is the so-called *bag model*; in particular the MIT *bag model* [16] contains the essential characteristics of the phenomenology of quark confinement. In this model, quarks are treated as massless particles inside a bag of finite dimension, and are infinitely massive outside the bag. In the model, the confinement is the result of the balance of the bag pressure B , directed inwards, which mimic the fundamental effect of non-perturbative QCD, and the stress arising from the kinetic energy of the quarks. The deconfinement occurs when the pressure of the quark matter inside the bag is increased to become greater than the inward bag pressure. The increase can arise when the temperature of the matter is high and (or) when the baryon number density is high. The latter case is a consequence of the Pauli exclusion principle: the requirement that no more than one fermion can populate a state with a

definite set of quantum numbers leads to the restriction that, as the density of the quarks increases, the quarks must populate states of greater momentum. This is the condition expected in neutron stars. On the other hand, the QGP formation in a high temperature and low baryon density medium is the expected scenario for high-energy heavy-ion collisions and will therefore be discussed in more details in the following. At very high energies the coupling constant of QCD becomes weak and a gas of particles should, to a good approximation, become an ideal gas. If such gas is in thermal equilibrium at the temperature T , its energy density ε_{gas} can be easily inferred from the Fermi-Dirac and Bose-Einstein statistics (see for example [17]), resulting:

$$\varepsilon_{gas} = g\frac{\pi^2}{30}T^4 \tag{1.5}$$

where g is the number of particle degrees of freedom. For massless fermions and bosons, the pressure P_{gas} is related to the energy density by

$$P_{gas} = \frac{\varepsilon_{gas}}{3} \tag{1.6}$$

hence, from Eq. 1.6:

$$P_{gas} = g\frac{\pi^2}{90}T^4 \tag{1.7}$$

The total energy density and pressure of the system, taking into account the bag pressure, are therefore given by:

$$\varepsilon_{gas} = g\frac{\pi^2}{30}T^4 + B \tag{1.8}$$

and:

$$P_{gas} = g\frac{\pi^2}{90}T^4 - B \tag{1.9}$$

At sufficiently high temperature, the quark matter inside the bag will have a pressure which is bigger than that of the bag pressure: when this happens the quark matter becomes deconfined. In the model, quark matter at temperatures below deconfinement is assumed to be constituted by (massless) pions. For an ideal gas of pions, the number of degrees of freedom is 3 (the possible values of the third component of the isospin), while for a Quark-Gluon Plasma it is:

$$g_{QGP} = g_g + \frac{7}{8} \times (g_q + g_{\bar{q}}) \tag{1.10}$$

where g_g , g_q and $g_{\overline{q}}$ are the degeneracy number of the gluons, the quarks and the antiquarks, respectively. The 7/8 factor arises from the Fermi-Dirac statistics. The gluon contribution can be evaluated by accounting for the existence of 8 gluons with two possible polarization each, hence:

$$g_g = 8 \times 2 \tag{1.11}$$

The degeneracy number g_q of the quarks depends on the number of colors ($N_c = 3$), the spin states ($N_s = 2$) and the number of flavors taken into account (N_f), which is three if the temperature is below the charm quark mass, hence:

$$g_q = g_{\overline{q}} = N_c \times N_s \times N_f = 3 \times 2 \times 3 \tag{1.12}$$

The total number of degrees of freedom is thus $g_{QGP} = 47.5$, i.e. more than an order of magnitude greater than the equivalent number for a pion gas: this results in a steep rise of the energy density (Eq. 1.5) in the narrow region of temperature corresponding to the phase transition from hadron gas to QGP.
The QCD phase diagram is schematically shown in Fig. 1.3. The vertical axis is the temperature T, while the horizontal is the quark Fermi level, or chemical potential μ_B, which measures the baryon number density. The solid line represents a first order phase transition, the dashed line a rapid crossover while the black point between the two lines is the second order phase transition. We recall that an n^{th} order phase transition is characterized by a discontinuity in the n^{th} derivative of the free energy with respect to a thermodynamic variable, while a crossover is a rapid but continuous transition. The phase diagram region explored by high-energy heavy-ion collisions and by neutron stars is also shown.

Order of the transition

From the QCD predictions, the phase transition should be of second order in the chiral limit of 2-flavour QCD, and of first order for 3-flavour QCD; on the other hand, in the case of the physically realized quark-mass spectrum, it is likely to be only a rapid crossover. This crossover can however take place in a narrow temperature range, which makes the transition between the hadronic and plasma phases still well localized. For this reason, the energy density rises rapidly near the crossover temperature. In Fig.1.4 the results of the lattice calculations are shown for what concerns the energy density in the limit of 2 and 3 zero mass quarks, as well as of 2 light and a heavier quark [10].

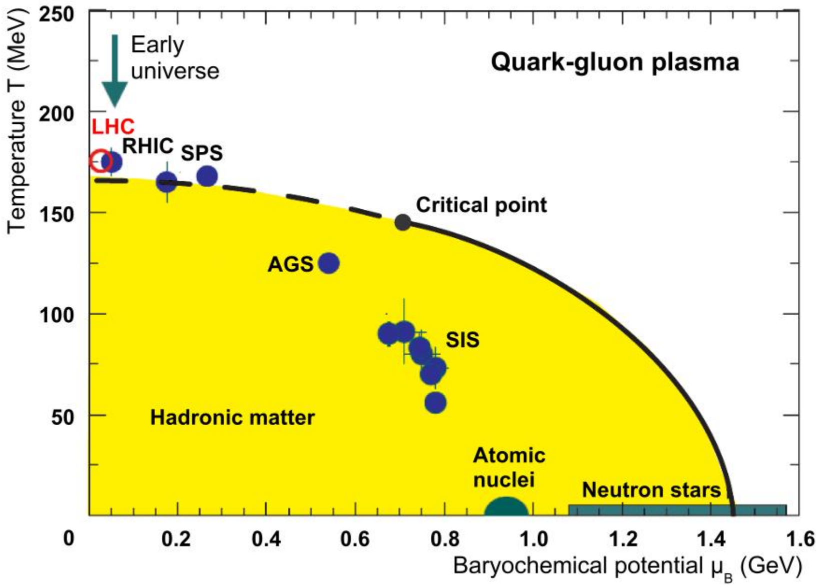

Figure 1.3: Phase diagram of hadronic and partonic matter. Chemical freeze-out points measured by various experiments are also shown. The existence and position of the critical point as well as the nature of the phase transition are only indicative and still under intensive study and discussion. [18]

1.5 Hunting QGP: Heavy-Ion Collisions

The study of nuclear collisions is not a new endeavor and, in fact, anticipate the parton model. The history of the field can be traced back to the **HILAC** (*Heavy Ion Linear Accelerator*) at Berkeley, the first dedicated heavy-ion accelerator, which began operation in 1957. The objectives of the research at the time were the creation of new elements by nuclear transmutation and the investigation of radiation damage to human tissue for space travel [21].

During the 1970s a new paradigm began to emerge in which heavy-ion collisions were viewed as a tool to study the equation of state of matter at high temperature and density, conditions thought to govern the behavior of matter inside neutron stars.

In fact, relativistic heavy-ion collisions can be used to excite the vacuum since the almost simultaneous collisions of the nucleons in the two nuclei releases a large amount of energy over a very short time interval, within a volume approximately

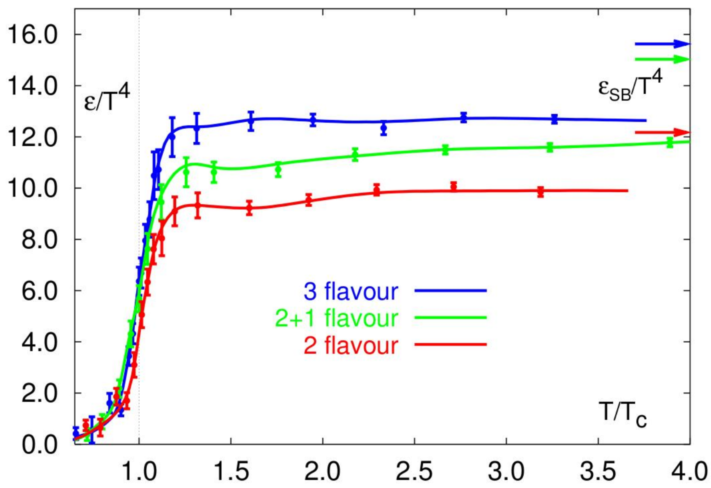

Figure 1.4: Lattice QCD results [11] for the energy density $\varepsilon/\ T^4$ as a function of the temperature scaled by the critical temperature T_C . Note the arrows on the right side indicating the values for the Stefan-Boltzmann limit. [19]

the size of the nucleus, which may create energy densities above that required for a phase transition $\sim$1GeV/fm^3.
Heavy-ion experiments involving nucleus-nucleus collisions started in the early 1970s at the **Bevalac** at *Lawrence Berkeley National Laboratoy* (**LBNL**) to study the nuclear matter equation of state at densities several times higher than the nuclear ground state density. Various species of nuclei were used at center of mass energies up to $\sqrt{s_{NN}}$ = 2.32 GeV at the Bevalac.
With the discovery of QCD, and the predicted existence, at high temperatures, of a deconfined state of matter consisting of free quarks and gluons, experimental facilities were built to run at higher center of mass energies. A large number of nucleus-nucleus collision experiments have been run at various facilities. For example, the *Alternating Gradient Synchrotron* (**AGS**) at *Brookhaven National Laboratory* (**BNL**) and the *Super Proton Synchrotron* (**SPS**) at **CERN** have run fixed target heavy-ion collision experiments at top center of mass energies of $\sqrt{s_{NN}}$= 4.86 GeV and $\sqrt{s_{NN}}$ = 17.3 GeV respectively.
So far, the highest energy nucleus-nucleus collisions have been run at the *Relativistic Heavy-Ion Collider* (**RHIC**) at BNL which is also the first machine to col-

lide beams of heavy-ions. RHIC has collided *Au-Au* and *Cu-Cu* beams at $\sqrt{s_{NN}}$ = 22.4, 62.4, 200 GeV and large amounts of data have been analysed by the four RHIC experiments (**BRAHMS**, **PHENIX**, **PHOBOS** and **STAR**) at these high energies.
Actual plans for the field include the highest energy nucleus-nucleus collisions yet, which are planned to be run at the *Large Hadron Collider* (**LHC**) at CERN with first collisions of ***Pb-Pb*** up to $\sqrt{s_{NN}}$ **= 5.5 GeV** starting from fall 2010. In particular **ALICE** is the unique LHC experiment that has been optimized to investigate the hot and dense matter that is supposed to be create through *Pb-Pb* collisions at LHC.

1.6 Phenomenology of heavy-ion collisions

The heavy ions experiments, like ALICE at the LHC, are aimed to detect the possible the creation of the QGP phase through the collision of heavy nuclei at very high energy. In the collisions, the density of matter is increased as far as possible beyond the ordinary nuclear matter density ($\rho_0 = 0.17$ nucleons/fm^3); while the energy increases, the nuclei penetrate each other bringing the matter form highly excited states to a quark gluon plasma: at the LHC energies, the colliding nuclei pass through each other, leaving behind them the hot and dense matter that eventually hadronize. After the collision, the high energy density allows to turn on the degree of freedom normally hidden in the ordinary nuclear matter that successively turn off during the expanding and cooling down phase. The different stages of the event evolution can be qualitatively described by the picture formulated by Bjorken [11, 12].
In Fig.1.5 it's possible to follow this space-time representation of the event, from the collision to the final state:

1. At t = 0 the two nuclei *collide*: they are Lorentz contracted, thus the longitudinal coordinate of all the nucleons is the same (Fig.1.6).

2. During the *pre-equilibrium* phase (t$<$1fm/c) the system reaches the maximum energy density, forming a not yet thermalized system of quark and gluons into a volume of some tens of fm^3 ; prompt leptons and photons can be emitted.

3. Then, thanks to the interactions among the partons, the system starts to thermalize: in these conditions and before the energy density drops below the

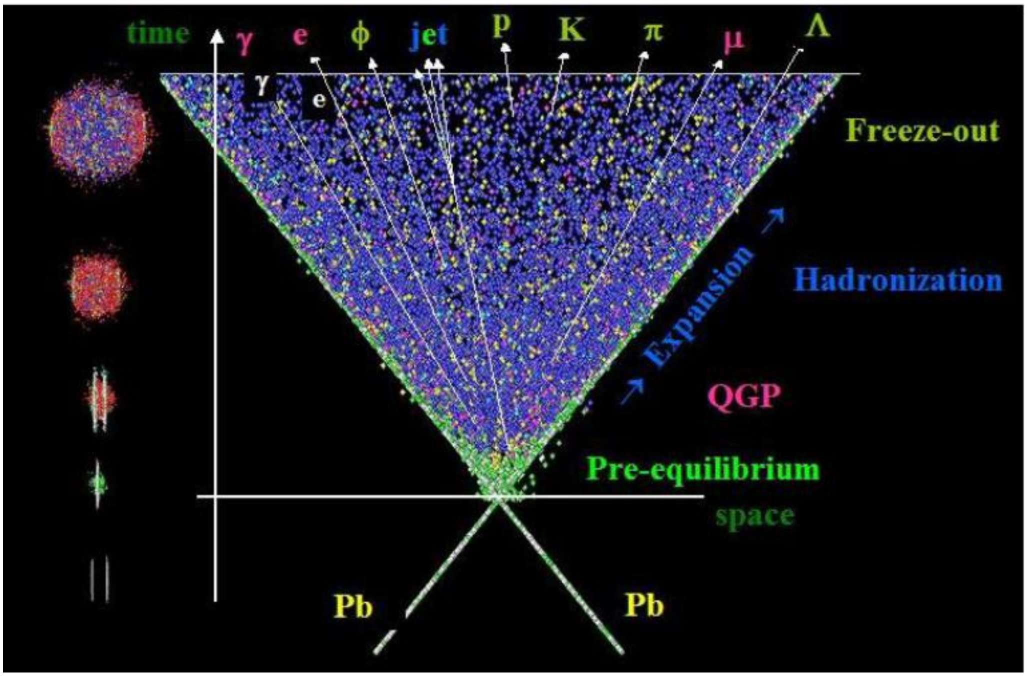

Figure 1.5: The space-time evolution of the heavy-ion collision. The various stages of the collision, drawn on the left part of the figure, are described, moving along the down-up direction, by the space-time representation and indicated with the conventional names on the right; on top, the particle types produced in the different stages of the evolutions are summarized. See the test for a more detailed description of the process as predicted by Bjorken.

critical value, the quark-gluon plasma is formed and the matter deconfinement takes place, at a time estimated of order 1 fm/c after the collision (*QGP phase*); direct leptons and photons and hard jets are produced.

4. The partons from different nucleon-nucleon collision rescatter leading to local thermal equilibrium and generating a thermodynamic pressure which brings to a collective expansion of the matter; the system cools down and the surface, already at a temperature below T_c evaporates into a hadron gas (*hadronization stage* , t$\sim$20 fm/c).

5. At the *freeze-out stage*, the expansion and the temperature fall lead first

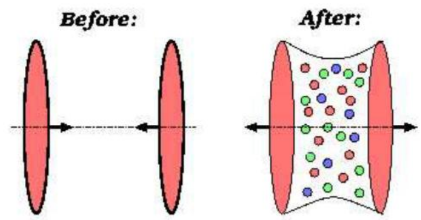

Figure 1.6: Two nuclei approach one another at almost the speed of light. Travelling at relativistic speeds causes them to look flat rather than spherical.

to a reduction of the inelastic processes among hadrons, until the relative abundance of hadron species is fixed (*chemical freeze-out*), and finally to the turn-off of any interaction which fixes the kinematic spectra (*kinetic freeze-out*). This is the stage at which particles (denoted by the arrows in the Fig.1.5) are measured in experimental detectors.

The strong interactions among the partons and hadrons before freeze-out wipe out much information about their original production processes. Extracting information about the hot and dense early collision stage thus requires to exploit features which are either established early and survive the rescattering and collective expansion or can be reliably back-extrapolated. Correspondingly, one classifies the observables into two classes: early and late signatures. The abundances and spectra of hadrons made of light quarks (u and d) belong to the latter category and can provide useful information on the hadronization and freeze-out of the collision. On the other hand, thermal photons produced in the plasma and heavy flavors and quarkonia constitute early probes of the medium.

1.7 The QGP Signature

Since it is impossible to directly observe this short lived QGP system, the Heavy Ions experiments like ALICE take the challenge to study the different typologies of observables that would confirm the existence and the properties predictions by the theory for this matter phase and for the event evolution described before. The signatures of the QGP can be divided in different categories, related to the different stages considered by the evolution picture described before: the *deconfined* *medium* (QGP), a possible *interacting hadronic medium*, and the final *hadronic state* [24]. The main direct hard probes of the creation of the QGP phase are:

- **Hard emission of thermal dileptons and photons** [25, 26]. These are a sort of internal probe: they are produced by the QGP itself and are not affected by the subsequent states of the medium, since they undergo only weak and electromagnetic interactions after their formation; therefore, they bear the imprints of the bulk properties of the early stages of the interaction and can be used as a thermometer of the medium, since they are produced also by the confined matter. It is very difficult to separate thermal dileptons and photons from the abundant hadronic production; moreover, the presence of a *prompt* component produced by early hard parton interactions in the primary and pre-equilibrium stages, has to be taken into account and separated as well.

- **Production of quarkonium states (J/Ψ,Υ) in the primary parton collisions** [29, 30]. These states are produced before the existence of any medium but their dissociation is possible only in a deconfined medium; their observed behaviour indicates therefore whether the subsequent medium was deconfined or not, resulting in a sort of external probe.

- **Jet quenching** [27, 28]. The energy loss of partons passing through the hot deconfined medium is expected to be larger than through the hadronic matter.

Informations about the evolution of the hadronic system, in particular about its last stage, where the hadrons are still interacting, can be provided by:

- **In-medium modifications of resonances observable in their decays** [31, 32, 33]. The changes of their masses or widths can originate from the large rescattering cross section in the medium, where the final state interactions influence in particular the hadronic decays. The study of these changes should be useful to distinguish between different *expansion* and *freeze-out* scenarios.

The expected QGP probes produced in the hadronization phase, the so called *soft probes*, which appear when the density of the medium has dropped sufficiently to allow the existence of hadrons, are:

- **Strangeness enhancement** [34, 35, 36]. A hot QGP should contain the different quark species in almost equal amounts, which, if preserved up to hadronization, should result in more abundant strangeness production than observed in *p-p* interactions, where the strange quark abundance is suppressed.

- **Collective flow and transverse momentum broadening** [37, 38]. Compared to *p-p* interactions, a hot initial QGP could lead to more pronounced expansion and specific expansion patterns.

In this sections, the main heavy-ion observables that will be measured and studied by the ALICE experiment as probes and signatures of the QGP are discussed, giving an overview of the present results, achieved by the previous experiments at SPS and at RHIC, and the perspectives for these topics research. Where necessary, the measurements of the same observables in proton-proton collisions will be discussed as a reference for nucleus-nucleus collisions.

1.7.1 Electromagnetic probes: photons and dileptons

The importance of the observation of collision products that undergo only electromagnetic and weak interactions has been stressed in the introduction of this overview of the QGP observables: probes with such characteristics can provide information about the different stages of the event evolution without being influenced by the traversed matter. The yields of dileptons and photons are compared between heavy-ion and *p-p* collisions to extract signals from the early collision phase.

Photons

The photons are produced in all the different stages of a heavy-ion collision and, owing to their small electromagnetic coupling, they do not interact strongly with the fireball [63, 64]. In particular the different production stages can be summarized qualitatively as follows:

- The *prompt* photons are produced early in the pre-equilibrium stage of the collision, by parton-parton scattering in the primary nucleus-nucleus (or nucleon-nucleon) collisions. In the high p_T domain ($p_T > 10$ GeV/c), the photons are produced in QCD hard-scattering processes. Although their

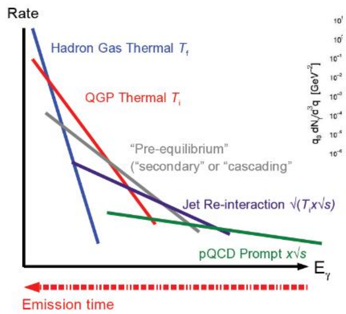

Figure 1.7: Sources of photons in relativistic heavy ion collisions. [65]

rate decreases as an inverse power of p_T , photons up to several hundred GeV are expected to be detected at LHC: their yield should be suppressed by the nuclear shadowing and the in-medium parton energy loss, but should be increased thanks to the partonic transverse momentum and to the photon radiation induced by the medium. The production nuclear effects and the medium effects have to be disentangled comparing the *Pb-Pb* observations with the *p-p* and the *p-p*b ones. The data from Tevatron experiments on *p-p* events and from RHIC appears to be well described by perturbative QCD. It has to be stressed that an important background to direct photon production is the decay $\pi^0 \to \gamma\gamma$, produced in similar hard partonic processes.

- In the equilibrium stage of the collision, the quark gluon plasma is expected to be formed with a temperature of up to 1 GeV. In the thermal bath, photons are radiated off the quarks which collide with other quarks and gluons. This production adds to the prompt photons in the low p_T domain ($p_T < 10$ GeV/c).

- After the QGP phase, the plasma expands and cools. At the critical temperature a hadronic phase is formed. In this phase, photons can be produced in the scattering of π,ρ,ω or in resonance decays. This mechanism continues until the resonances stop to interact, when the freeze-out temperature is reached. The theoretical predictions of the direct thermal photon spectra are based on two step calculations: the photon production rates from an equilibrated QGP and hadron gas are calculated and then convoluted with a model for the space-time evolution of the fireball.

- After freeze-out, further photons can be produced by the decay of π ,η and higher resonances, with energies in the range of up to a few hundred MeV. Photons produced by π decays, either from the primary collisions or final-state contribution, constitute a large but reducible background to direct photon production over the whole p_T range. Thus they can be subtracted from the data. Instead, the prompt photons provide an irreducible background but its estimate is necessary to extract the rate of thermal photons.

Dileptons

Dileptons e.g. lepton pairs, are a signal of medium modifications of hadronic matter. Furthermore, dileptons from charm decay allow the total charm yield to be accessed, which is important for the measurement of the total production cross-section of the J/Ψ.

Even for the dilepton production, as for the photons, it's possible to distinguish among prompt, thermal and freeze-out decay components:

- considering the dilepton mass range, above pair mass M $\sim$ 2 GeV the prompt contribution is dominated by semi-leptonic decays of heavy-flavour mesons and by the Drell-Yan process ($q\bar{q}$). Since these leptons originate from hard scatterings, their rates can be calculated in perturbative QCD;

- at lepton pair masses above $\sim$ 1.5 GeV , since the thermal radiation is very sensitive to temperature variations, it is expected to originate from the early hot phases, probably from $q\bar{q}$ annihilation. Similarly to the photon case, the thermal QGP radiation has to be discriminated of from the large prompt background;

- at low masses, less than 1.5 GeV, thermal dilepton spectra are dominated by the radiation process from the hot hadronic phase.

1.7.2 Quarkonia

Quarkonia (J/Ψ,Ψ', Υ, Υ' , Υ") are made of $c\bar{c}$ and $b\bar{b}$ pairs that are created in the initial phase of the collision. Color screening in the deconfined phase leads to melting of quarkonia states [29, 91]. The freed c and b quarks are unlikely to recombine to quarkonia states during freeze-out if their concentrations are small. At much high energies c and b quarks are produced in large abundances and statistical hadronization may even lead to enhanced quarkonia production at freeze-out.

So, among the hard probes that could provide direct information on the deconfined medium produced in the heavy-ions events, charm and bottom quarks are very suitable to understand the dynamics of the collisions: their production takes place on a timescale of the order of 1/m_Q where m_Q is the heavy-quark mass. On the other hand, thanks to their long lifetime, charm and bottom quarks can live through the thermalization phase and be affected by its presence.
In order to extract information about the plasma from the features of heavy-quark production in A-A collisions it's very important to well understand their production in *p-p* and p-A interactions and compare some observables like the total production rates, the transverse momentum distributions and the kinematic correlations between the heavy quark and antiquark.
Both the productions of bound states of $c\bar{c}$ and $b\bar{b}$ (*quarkonia*) and of open charm and bottom will be extensively studied by ALICE, either as different probes of the event evolution and as interrelated topics. The study of the correlations between the properties of open charm and bottom and quarkonia spectra will allow to understand the dynamics of the dense medium: in the very low p_T region, which will be accessible to ALICE, the production of heavy quark-antiquarks pairs should increase the probability of forming quarkonia. In the region of perturbative production, i.e. at large p_T , the quarkonium suppression should take place.
Moreover, the different effects of enhancement in the productions of quark-antiquark pairs and of the quarkonium suppression should be disentangled by the study of the correlations between quarkonium and open heavy-quark momentum spectra.

Open charm and open beauty

The measurement of open charm and open beauty production allows one to investigate the mechanisms of heavy-quark production, propagation and, at low momenta, hadronization in the hot and dense medium formed in high-energy nucleus-nucleus collisions. The open charm and open beauty cross sections are also needed as a reference to measure the effect of the transition to a deconfined phase on the production of quarkonia: a direct measurement of the D and B mesons yields would provide the normalization for charmonia and bottomonia production.
Finally, the measurement of B meson production is necessary within the search for the quarkonia suppression, which will be further discussed, in order to estimate the contribution of secondary J/Ψ (from $B \to J/\Psi + X$) to the total J/Ψ yield: B mesons decay into J/Ψ mesons with a branching ratio of about 1%. Since B

mesons are produced by a factor of 5 more abundantly than J/Ψ mesons, and since direct J/Ψ production might be further suppressed by QGP effects, secondary J/Ψ mesons are plausibly contributing a large fraction to the observable J/Ψ signal.
The measurement of charm and beauty production in proton-proton and proton-nucleus collisions, besides providing the necessary baseline for the study of medium effects in nucleus-nucleus collisions, is intrinsically interesting as a test of both perturbative and non-perturbative sectors of QCD in a new energy domain.

Charmonium

Suppression of heavy quarkonia is one of the earliest and most striking proposed signatures of deconfinement. The suppression mechanism follows directly from the Debye screening expected in the medium, which reduces the range of the potential between charm quark and anti-quark pairs [29].
A particular attention have been dedicated to Charmonium: the bound states of charm quark and anti-charm quark. The first charmonium discovered is J/Ψ , which is discovered by two independent groups in November 1974. The discovery of J/Ψ play a very important pole in the development and evolution of the Standard Model, causing the introduction of charm quark into the Standard Model. From that time, more and more charmonium states were discovered.
In the presence of the medium, the Charmonium production in high energy heavy ion collisions is different with that in hadron collisions. The J/Ψ has long been thought of as the probe that could definitively prove the formation of a QGP in relativistic heavy ion collisions. Both calculations performed by Matsui and Satz in the 1980s and Lattice QCD results (of the time) predicted that charmonium bound states would 'melt' in the QGP due to the color screening effect, and that this process would lead to a suppression of charmonium yields when compared to nominal pQCD calculations. This suppression was proposed as one of the signature of the formation of QGP. But there are other medium effects that can influence this probe and that have to be considered.
Nowadays scientists believe that the medium effects on the charmonium production in heavy ion collisions can be categorized into two parts:

1. the effects from the QGP, called as *final state effect*;
2. the effects from the nuclear matter before the QGP formation; these initial state effects don't require the formation of QGP thus usually referred as

cold nuclear matter effects (CNM).

As the final state effects, the possible contributions are:

- Color screening by the abundance of thermal partons in QGP.

- Recombination from uncorrelated $c\bar{c}$ pairs in QGP at the phase boundary.

- Interaction of charmonium with secondary comoving hadrons (comovers).

For the CNM effects, the possible contributions are:

- Modification of gluon distribution function in heavy nuclei such as gluon shadowing, gluon anti-showing and etc.

- Interaction of pre-resonance $c\bar{c}$ state with the projectile or target nuclei, usually referred as nuclear absorption.

- Multiple interactions of partons inside the nuclei, usually referred as *Cronin* effect.

The **NA38** and **NA50** experiments have carried out a systematic study of J/Ψ and Ψ' at the CERN-SPS in *p-p*, *p-A*, light ion, and *Pb-Pb* collisions providing some of the most intriguing results of the relativistic heavy ion program for more than ten years.
The NA50 experiment observed an anomalous suppression of J/Ψ in central *Pb-Pb* collisions at $\sqrt{s_{NN}}$= 17.2 GeV [66]. The suppression, which is of the order of 25% with respect to the normal suppression in nuclear matter, has been interpreted by the NA50 authors as evidence for deconfinement of quarks and gluons. Although this interpretation is not universally shared [67], the results of NA38 and NA50 demonstrate the utility and great interest in understanding the fate of charmonium in dense nuclear matter.
The NA60 experiment [68] has studied J/Ψ production in*In-In* collisions at 158 GeV/nucleon at the CERN SPS, through its decay into two muons. In Fig. 1.8 the comparison between the J/Ψ centrality distribution with the expectation from a pure nuclear absorption scenario is showed: an anomalous suppression that sets in for more than 80 participant nucleons and saturates for more central events has been found. The statistical errors are negligible (of the order of 2%). Most of the systematic errors are centrality independent and therefore do not affect the measured shape of the J/Ψ suppression pattern [69]. This result is in qualitative

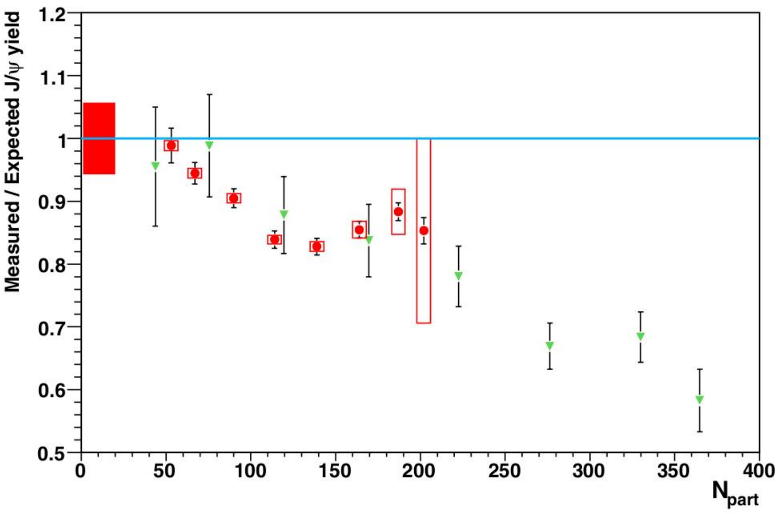

Figure 1.8: Comparison between the *In-In* (NA60, circles) and *Pb-Pb* (NA50, triangles) suppression patterns. The box on the left shows the 6% systematic error related to the normalization procedure of the *In-In* points. [69]

agreement with previous *Pb-Pb* measurements by the NA50 experiment, but no theoretical explanation is presently able to coherently describe both results.

Latest results at RHIC show that the suppression of the J/Ψ as a function of centrality (the number of participants) is similar to that observed at the SPS, even though the energy density reached in collisions at RHIC is significantly higher [70, 71]. Possible mechanisms such as sequential suppression [72], $c\bar{c}$ recombination [73, 74, 75, 76] were proposed to explain this.
Recent Lattice QCD calculations indicate that direct J/Ψ is not dissociated in the medium created at RHIC while the suppression observed for J/Ψ comes from the dissociation of χ_c and Ψ' [77].

However, the direct J/Ψ might be dissociated at RHIC at high p_T , which was predicted in the *Hot Wind* dissociation picture, in which the AdS/CFT approach was used and the dissociation temperature for J/Ψ was predicted to decrease as a function of p_T [78]. The AdS/CFT approach was applied to hydro framework and predicted that J/Ψ nuclear modification factor R_{AA} decreases versus p_T [79].

Figure 1.9 shows J/Ψ R_{AA} as a function of p_T in 0-20% and 0-60% *Cu-Cu* collisions from STAR [37] and 0-20% *Cu-Cu* collisions from PHENIX [80].

The average of two STAR 0-20% data points at high p_T is R_{AA} = 1.4±0.4(stat.) ±0.2(syst.). Compared to low p_T PHENIX measurements, their results indicate that R_{AA} of J/Ψ increases from low p_T to high p_T at 97% confidence level. [81]

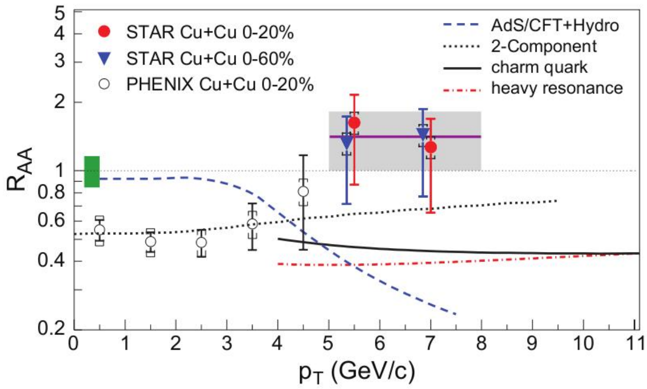

Figure 1.9: J/Ψ R_{AA} versus p_T . STAR data points have statistical (bars) and systematic (caps) uncertainties. The box about unity on the left shows R_{AA} normalization uncertainty, which is the quadrature sum of *p-p* normalization and binary collision scaling uncertainties. The solid line and band show the average and uncertainty of the two 0-20% data points. The curves are model calculations (AdS/CFT+hydrodynamic). The uncertainty band of 10% for the dotted curve is not shown. [81]

The R_{AA} of high p_T J/Ψ is in contrast to strong suppression for open charm [82, 83]: the experimental results are reproduced with next-next-to-leading order (NNLO) pQCD calculations with color singlet model except to high p_T part [40]. This problem is expected to be solved by the LHC statistics. Moreover, at LHC, the much higher energy offers the possibility of measuring with significant statistics the bottomonium yields providing another probe for QGP studies. In fact, the spectroscopy of the ϒ', whose dissolution energy can not be reached at RHIC, should reveal at LHC energies new information on the characteristics of the QGP.

1.7.3 Jet Quenching

Jet production in hadronic collisions is a paradigmatic hard QCD process. An elastic (2 → 2) or inelastic (2 → 2 + X) scattering of two partons from each one of the colliding hadrons (or nuclei) results in the production of two or more

partons in the final state. At high p_T , the outgoing partons radiate gluons and/or split into quark-antiquark pairs.
At this point, the produced partons fragment non-perturbatively materialize into a set of final-state hadrons.

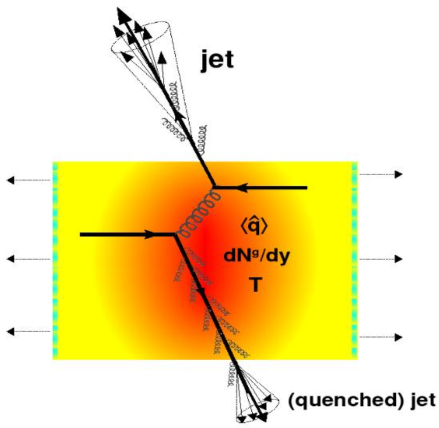

Figure 1.10: *Jet quenching* in a head-on nucleus-nucleus collision. Two quarks suffer a hard scattering: one goes out directly to the vacuum, radiates a few gluons and hadronises, the other goes through the dense plasma created (characterised by transport coefficient q, gluon density dN_g /dy and temperature T), suffers energy loss due to medium-induced gluonstrahlung and finally fragments outside into a (quenched) jet. [84]

The characteristic collimated spray of hadrons resulting from the fragmentation of an outgoing parton is called a *jet*.

One of the first proposed 'smoking guns' of QGP formation was *jet quenching* [22] i.e. the attenuation or disappearance of the spray of hadrons resulting from the fragmentation of a parton having suffered energy loss in the dense plasma produced in the reaction (Fig.1.10). The energy lost by a particle in a medium, ΔE , provides 'tomographic' information on its properties: In a general way, ΔE depends both on the characteristics of the particle traversing it (energy E , mass m, and charge) and on the plasma properties (temperature T , particle-medium interaction coupling α, and thickness L), i.e. ΔE (E , m, T , α, L).

The dominant mechanism of energy loss of a fast parton in a dense QCD plasma is of radiative nature (*gluonstrahlung*): the parton loses energy mainly by medium-induced multiple gluon emission [84].

Medium-induced parton energy loss in *A*-*A* reactions results in various observable consequences compared to the same measurements in proton-proton collisions. The presence of jet quenching manifests itself via :

1. a suppression of the spectrum (dN_{AA} /d p_T) of high- p_T hadrons [85]
2. unbalanced back-to-back high- p_T dihadron azimuthal correlations (dN_{pair} /dΦ) [86].

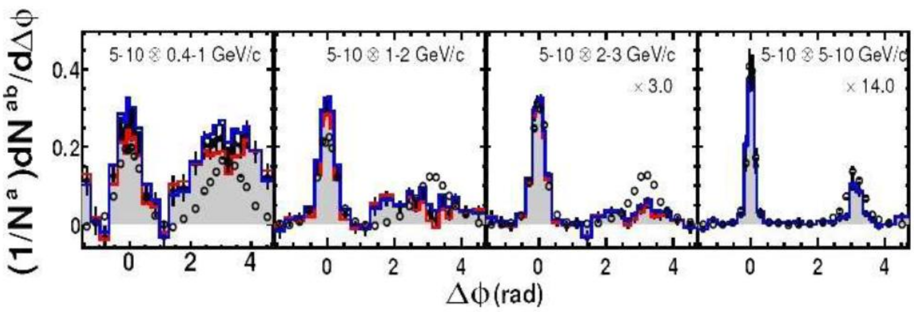

Figure 1.11: Comparison of the azimuthal di-hadron correlation dN_{pair} /d $\Delta\Phi d\eta$ for pp (open symbols) and central AuAu (histograms) at $\sqrt{s_{NN}}$ = 200 GeV for p_T = 5-10 GeV/c and increasingly smaller (right to left) values of p_T^{assoc}. [88]

Fig. 1.11 shows the increasingly distorted back-to-back azimuthal correlations in high- p_T triggered central AuAu events as one decreases the p_T of the associated hadrons (p_T^{assoc}) (right to left). Whereas, the AuAu and pp near-side peaks are similar for all p_Ts, the away-side peak is only present for the highest partner p_Ts but progressively disappears for less energetic partners [87, 88]. Early STAR results [89] showed a monojet-like topology with a complete disappearance of the opposite-side peak for p_T^{assoc} ∼2-4 GeV/c.

3. modified energy-particle flow (softer hadron spectra, larger multiplicity, increased angular broadening, ...) within the final jets [90].

In addition, due to a hierarchy of flavour-dependent radiative energy losses,

$$\Delta E(gluons) > \Delta E(lightquarks) > \Delta E(heavyquarks) \tag{1.13}$$

all these medium effects are expected to be larger for gluons and u, d , s quarks than for c or b quarks. [84]

At the upcoming LHC energies, the detailed analysis of jet spectra, jet shapes and the extraction of medium-modified parton-to-hadron fragmentation functions promise to fully unravel the mechanisms of parton energy loss in QCD matter.

1.7.4 Strangeness enhancement

Strangeness enhancement was one of the main pieces of evidence for CERN's claim to have produced deconfined matter [34].
Essentially, if a QGP phase was formed in nuclues-nucleus collisions, the yields of strange particles produced, such as those that contain one or more strange quark or antiquark, are expected to increase compared to a non-QGP scenario. In other words, the density of strange quark pair is predicted to be unusually high compared to that for an hadron gas phase [93].
The mechanism for strange quark-pair production can be described by thermal reactions in the plasma such gluon fusion ($gg \rightarrow s\bar{s}$), which turns out to be the dominant process of $s\bar{s}$ pair production.
One of the features of this signature is that, if deconfinement occurs, the reactions that lead to strangeness production have to be partonic. At the partonic level, strange particles have lower thresholds and higher cross-sections. This is particularly so if the strange quark mass reduces owing to the associated partial restoration of chiral simmetry.
The bare mass of strange quark is about 150 MeV and, with a plasma temperature of about 200 MeV, it becomes energetically casy to produce large numbers of strange quark-antiquark pairs [95]. Multistrange hadrons, i.e. hadrons with more than on a strange quark, and their antiparticles will be particularly enhanced. Their single-step production in a hadron gas has a higher energy threshold. Strange antiparticles can only be produced after a sequence of many reactions(e.g. $\pi\overline{\Lambda} \rightarrow K\overline{\Xi}, \pi\overline{\Xi} \rightarrow K\overline{\Omega}$). They are particularly difficult to produce in a baryon-rich environment since baryon number conservation indicates they can only be created with an accompanying baryon. However at central rapidities at the LHC there should be equal numbers of baryons and antibaryons, since the valence numbers cannot shift enough in rapidity.

Experimentally one can study the strangeness enhancement by looking for an increase in the production of hadrons containing strangeness with increasing number of participants from proton-proton to nucleus-nucleus collisions. Experimental data, both at SPS and RHIC, shown in Fig. 1.12 , confirm the theoretical expectations [92, 96, 97, 98].

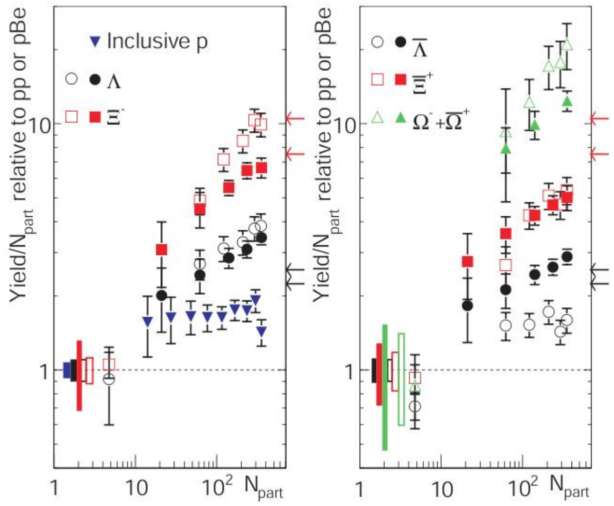

Figure 1.12: Enhancement of strange and multi-strange baryons at SPS and RHIC [92]. The solid symbols are for *Au-Au* at $\sqrt{s_{NN}}$ =200 GeV and the open symbols are for *Pb-Pb* at $\sqrt{s_{NN}}$=17.3 GeV. Boxes at unity show the combined statistical and systematic uncertainties in the *p-p* (*p-Be*) data. Error bars on the data points represent those from the heavy ion data. The arrows on the right (red for Ξ, black for Λ) mark canonical model predictions, see text for details.

There is no enhancement observed in *p-Pb* collisions, while in *Pb-Pb* and *Au-Au* collisions one sees a clear enhancement of the strange and multi-strange baryon yields, which are found to increase with centrality and strangeness content. In central *Au-Au* collisions the yield per participant is a factor of ~ 10 higher compared to that in *p-p*.
The features observed in the experimental data can be interpreted using the *statistical model* for particle production imposing the canonical constraints of *strangeness conservation* in small systems [99, 100]. The model predictions agree with the beam energy dependence and the strangeness content dependence observed in the data, but fail to reproduce the absolute amounts and the centrality dependence of the enhancements.
Althought strangeness production has been historically a relevant QGP signature,

the role it would play at the LHC may be different from that at SPS energies. This is mainly because lifetime of the fireball is much higher, which means that even in hadron gas this enhancement effect might be seen. The discussion on strangeness enhancement at LHC is still ongoing [94, 93].

1.7.5 Collective Flow

Radial flow is caused by the matter-density gradient between the center of the fireball and the boundary region. Additionally, elliptic flow occurs in non-central collisions due to the asymmetric, almond shaped, collision region which results in an anisotropic expansion. This effect is self-quenching in the sense that the expansion reduces the anisotropy and thus the elliptic flow. Therefore, the measurement of elliptic flow carries signatures of the earlier collision stages [104].
RHIC results on elliptic flow agree with *hydrodynamic* calculations (see chapter 4) that assume an ideal relativistic fluid consisting of strongly-interacting matter with very short mean free paths that shows free of viscosity [53, 49]. Contrarily, calculations assuming a pure hadron gas (and no deconfined phase) underpredict the measured elliptic flow. The level of flow that is measured at RHIC and the fact that the measured elliptic flow of identified hadrons scales with the constituent quarks is at present one of the strongest arguments for the discovery of the QGP.
A detailed overview and study on elliptic flow and on phi meson's elliptic flow will be presented on chapter 4 and 5.

1.7.6 Particle yields and transverse momentum distributions

Particle yields can provide information about the system from the time of chemical freeze-out when the inelastic collisions cease and the chemical abundances become fixed. Statistical models [51] allow the calculation of hadron yields of an equilibrated system. In turn, the measured yields can be used to calculate the parameters of the equilibrated system, in particular the chemical freeze-out temperature and the baryochemical potential. *Statistical Thermal Models* (in a number of variations) [48], have been very successful in describing the experimental particle ratios (observed at RHIC) using only a few model parameters (i.e. chemical freeze-out temperature , baryon and strangeness chemical potentials μ_B and μ_S and strangeness suppression factor γ_s) extracted from fitting to particle yield ratio data. In Fig. 1.13 a comparison of statistical model results to data from the STAR experiment is showed.

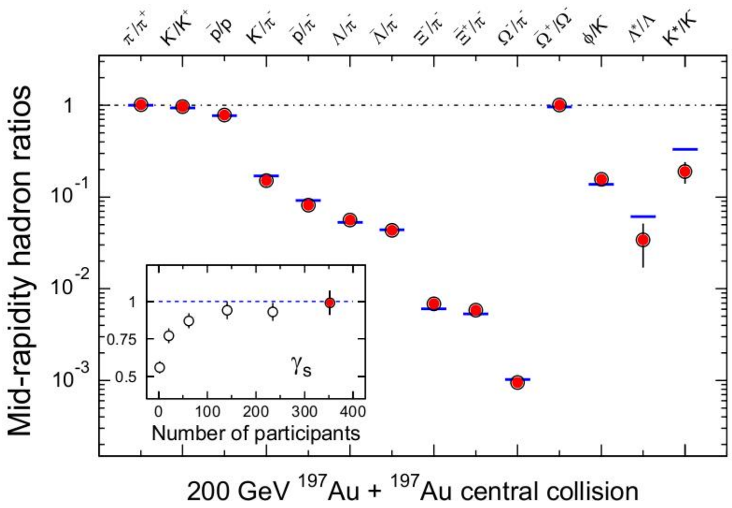

Figure 1.13: Ratios of the mid-rapidity p_T-integrated yields for different hadron species measured by the STAR experiment for *Au-Au* collisions at $\sqrt{s_{NN}}$ = 200 GeV (circles). The horizontal lines represent statistical model fits to the measured particle yield ratios. The inset shows the extracted variation of γ_s as a function of centrality. [49]

The plot shows the integrated p_T particle yield ratios (circle markers) measured by the STAR experiment in *Au-Au* collisions at $\sqrt{s_{NN}}$ = 200 GeV. The horizontal lines show the statistical model fits to the particle ratios using only 3 parameters (T_{ch} = 163 ± 4 MeV, μ_B = 24 ± 4 MeV, γ_s = 0.99 ± 0.07). These values are similar to values obtained using different variations of the statistical model [51, 50] for RHIC data. Shown in the inset in Fig.1.13 is the evolution of the strangeness suppression factor γ_s which is a measure of how far the system is from chemical equilibrium. For the most central collisions, the γ_s value obtained from the statistical model fits is γ_s = 0.99 ± 0.07 [52] i.e. consistent with unity, providing a strong argument in favour of the system, which is created in central collisions at RHIC, being in chemical equilibrium.

On the other side, measurements of particle transverse momentum distributions provide information on the properties of the system at thermal or kinetic freeze-out when all elastic collisions have ceased.
The idea of a common collective outward expansion velocity (β_T) of particles in the system is consistent with the observations that the p_T of heavier particles is larger than for lighter particles (i.e. for the same outward velocity, more mas-

sive particles will have a larger momentum) and that p_T increases as a function of centrality [49, 53].

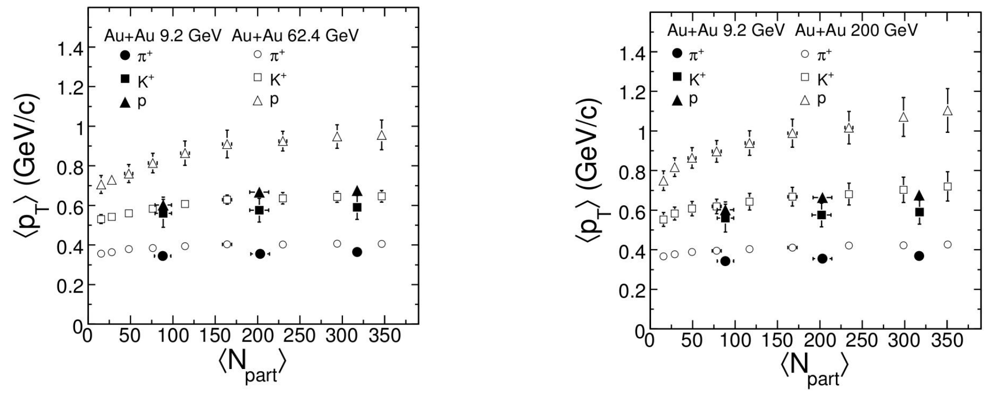

Figure 1.14: $<p_T>$ for π^+, K$^+$ and p plotted as a function of $<$ N$_{part}$ $>$ for *Au-Au* collisions at $\sqrt{s_{NN}}$ = 9.2 GeV and compared to corresponding results at $\sqrt{s_{NN}}$ = 62.4 GeV (left) and 200 GeV (right). The errors shown for $\sqrt{s_{NN}}$ = 9.2 GeV data are statistical. The corresponding systematic errors for pions, kaons, and protons are $\sim$12%, 18%, and 21% respectively, and similar for all the collision centralities studied. Errors shown for $\sqrt{s_{NN}}$ = 62.4 and 200 GeV data are the quadrature sum of statistical and systematic uncertainties.

Figure 1.14 shows the increase of p_T for π^+, K^+ and p as a function of centrality as measured by the STAR experiment for *Au-Au* collisions at $\sqrt{s_{NN}}$ = 9.2, 62.4 and 200 GeV. [53].

In order to gain further information and attempt to quantify the transverse expansion of the system, particle spectra, measured by the STAR experiment, have been plotted with a hydrodynamics-inspired parameterization of a thermal expanding source (so-called *blast-wave model*) [55] with fit parameters including the thermal freeze-out temperature (T_{fo}) and the mean collective expansion velocity (β_T).

Fig. 1.15 [49] shows the results from fitting the spectra for π, K, p simultaneously, as a function of centrality. The extracted p_T is highest for most central collisions while T_{fo} is lowest. This implies that the system created in central collisions expands faster and cools down to a lower temperature ($T_{fo} \sim$ 80 MeV) before thermal freeze-out with respect to systems created in more peripheral collisions ($T_{fo} \sim$ 140 MeV).

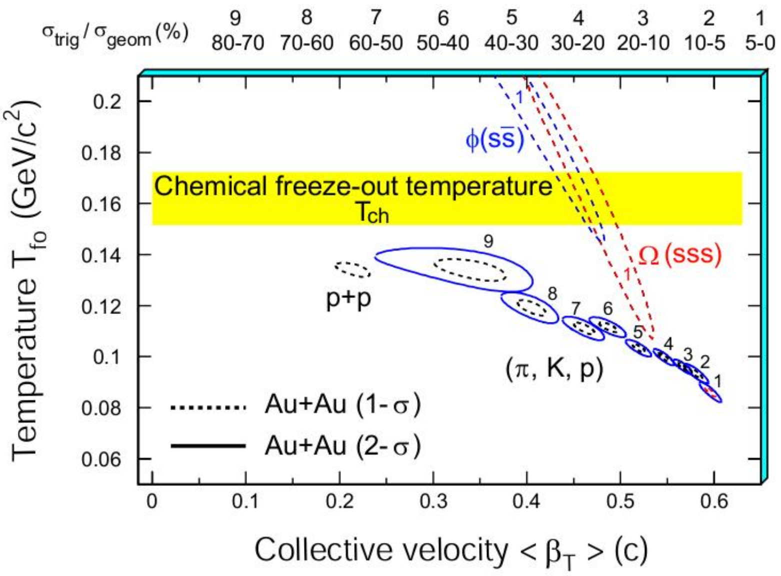

Figure 1.15: The χ^2 contours, extracted from thermal + radial flow fits (without allowance for resonance feed-down), for copiously produced hadrons π, K and p and multi-strange hadrons ϕ and Ω. On the top of the plot, the numerical labels indicate the centrality selection. For π,, K and p, 9 centrality bins were used for $\sqrt{s_{NN}}$ = 200 GeV *Au-Au* collisions . The results from *p-p* collisions are also shown. For ϕ andΩ, only the most central results are presented. Dashed and solid lines are the 1-σ and 2-σ contours, respectively. [49]

On the other hand, even for the most central collisions, the spectra for multi-strange particles ϕ and Ω appear, albeit with still large uncertainties, to reflect a higher temperature [52]. The ϕ and Ω results suggest diminished hadronic interactions with the expanding bulk matter after chemical freezeout [59, 52, 60, 61, 62] as predicted [56, 57, 58] for hadrons containing no valence u or d quarks. If this interpretation is correct, the substantial radial flow velocity inferred for ϕ and Ω would have to be accumulated prior to chemical freeze-out, giving the multi-strange hadrons perhaps greater sensitivity to collective behavior during earlier partonic stages of the system evolution.

1.7.7 Particle multiplicity

One of the most important observables that ALICE has measured already from the first days of LHC *p-p* collisions is the charged particles multiplicity. The quantities related to the event geometry, like the impact parameter *b*, the number of participant nucleons in the interaction N_{part} and the number of nucleon-nucleon collisions, can be extracted from the measurement of the multiplicity in a rather model-independent way. Reconstructing the centrality of the collisions, it is possible to select and study in particular the collisions where the maximum energy density is reached; moreover, once determined the centrality of the collision, it's possible to study the physics observables as a function of *b* or N_{part} in order to locate the onset of the phase transition from the hadronic to the deconfined matter. A complete characterization of the event will be finally provided by the information about the temperature and the energy density reached in the collision, that can be inferred from the charged particle rapidity density dN$_{ch}$ /dy and the p_T distributions. However, the multiplicity and another important global observable like the total transverse energy can not be calculated starting from the QCD Lagrangian, because the soft non-perturbative QCD and the processes on the large scale dominate these observables. Due to these causes, it is also difficult to extrapolate the expected multiplicity in the ALICE events from previous results obtained at SPS or even at RHIC. As already experienced before the start-up of RHIC, the extrapolations from SPS measurements at $\sqrt{s}$ = 20 to the 200 GeV RHIC energy varied widely [39], as shown in Fig.1.16 , mostly overestimating the result.

In the following paragraphs the expectations of the particle multiplicity in proton-proton and in nucleus-nucleus collisions will be discussed.

p-p collisions: First ALICE measurement

The ALICE experiment has measured the charged particle multiplicity in proton-proton events, as a benchmark for the further study in *A-A* events but also to extract informations about the phase transition to QGP from the multiplicity fluctuations.

The very first proton-proton collisions at Point 2 of the CERN Large Hadron Collider (LHC) [40] occurred on 23rd November 2009, at a centre-of-mass energy $\sqrt{s}$ = 900 GeV, during the commissioning of the accelerator. The 284 events recorded in the ALICE detector [41] on that day, without magnetic field, has made possible the determination of the pseudorapidity density of charged primary particles (prompt particles produced in the collision and all decay products, except products from weak decays of strange particles such as K^0_S and Λ): $dN_{ch}/d\eta$

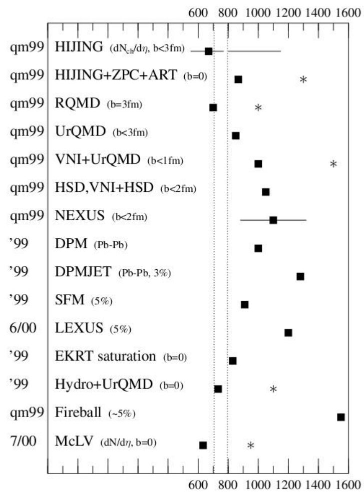

Figure 1.16: Predictions for dN_{ch} /dy in *Au-Au* collisions at y =0, $\sqrt{s_N N}$ = 200 AGeV, from different models before the appearance of the first RHIC data. The extrapolations vary widely, mostly overestimating the experimental result of less than 600 charged particles. The table is here shown to emphasize the variety of the extrapolations of the charged particle multiplicity, depending on the used model. For certain predictions (those marked by an asterisk), the 2/3 correction is applied to the total multiplicity prediction in order to obtain the charged particle one (boxes). [49]

with $\eta \equiv$ -ln $tan\theta/2$, where θ is the polar angle with respect to the beam line in the central pseudorapidity region. This measure has been performed in order to compare with previous measurements for proton-antiproton ($p\overline{p}$) collisions at the same energy [44], and to establish a reference for comparison with forthcoming measurements at higher LHC energies. In Fig. 1.17 and Fig. 1.18 are showed the first experimental results. In order to compare ALICE data with those of other experiments, the result are provided with two different normalizations: the first one (**INEL**) corresponds to the sum of all inelastic interactions and corrects the trigger bias individually for all event classes, by weighting them, each with its own estimated trigger efficiency and abundance; the second normalization (non-single-diffractive or **NSD**) applies this correction for non-diffractive and double-diffractive processes only, while removing, on average, the single-diffractive contribution.

The charged primary particle pseudorapidity density distributions obtained for

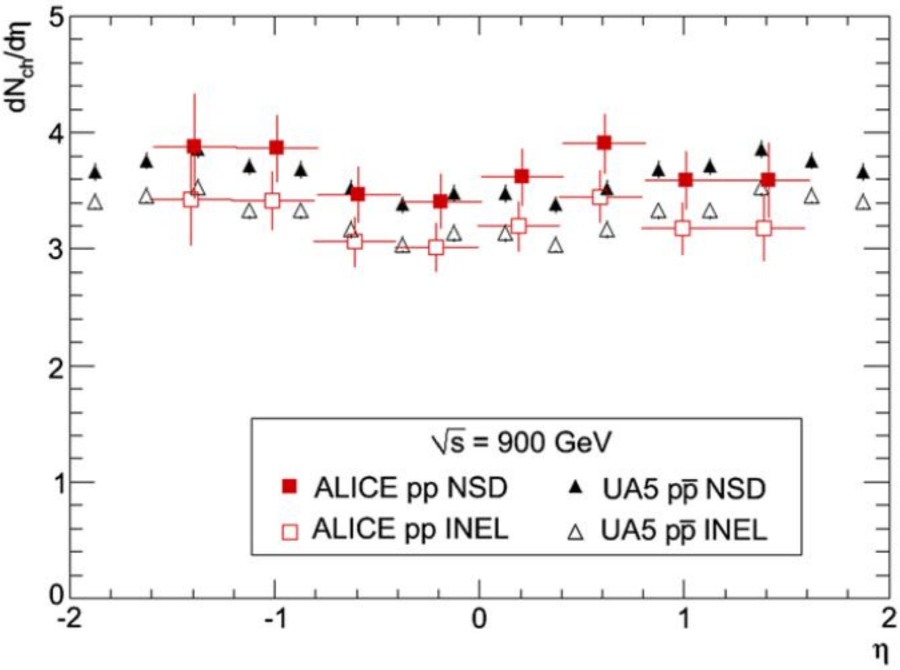

Figure 1.17: Pseudorapidity dependence of $dN_{ch}/d\eta$ for INEL and NSD collisions. The ALICE measurements (squares) are compared to UA5 data (triangles). The errors shown are statistical only. [42]

INEL and NSD interactions in the range $|\eta| < 1.6$ are showed in Fig.1.17.

The pseudorapidity density obtained in the central region $|\eta < 0.5$ for INEL interactions is 3.10 ± 0.13(stat.) $\pm$ 0.22(syst.) and for NSD interactions is 3.51 ± 0.15(stat.) $\pm$ 0.25(syst.). Also shown in Fig. 1.17 are the previous measurements of proton-antiproton interactions from the UA5 experiment [44]. The results obtained for proton-proton interactions are consistent with those for proton-antiproton interactions, as expected from the fact that the predicted difference (0.1-0.2%) is well below measurement uncertainties. In Fig.1.18 the centre-of-mass energy dependence of the pseudorapidity density in the central region ($|\eta| < 0.5$) is shown.

The data points are obtained in the $|\eta| < 0.5$ range from this experiment and from references [44, 45, 46, 47] and are corrected for differences in pseudorapidity range where necessary, fitting the pseudorapidity distribution around $\eta = 0$. As

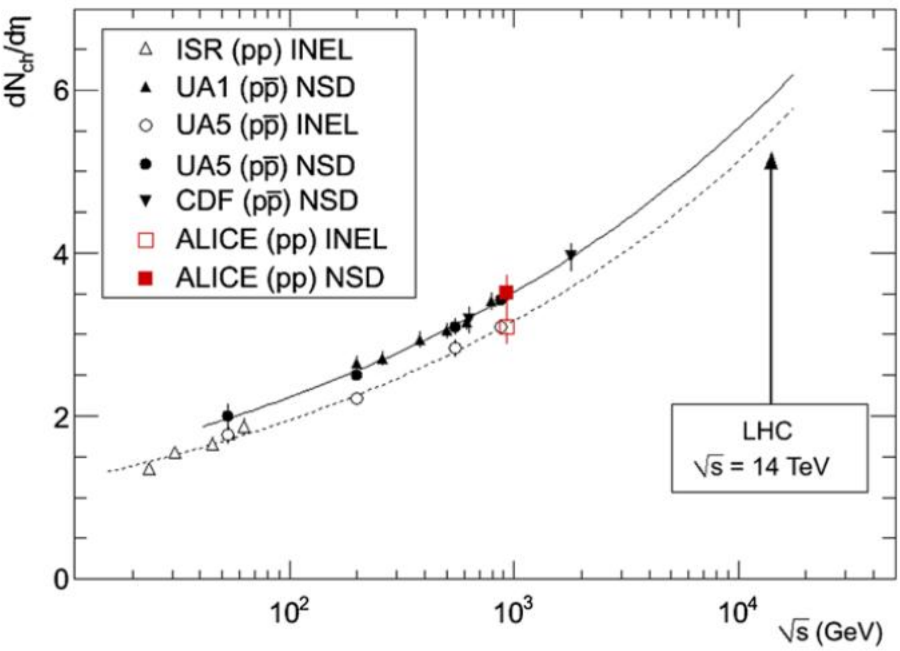

Figure 1.18: Charged-particle pseudorapidity density in the central rapidity region in proton-proton and proton-antiproton interactions as a function of the centre-of-mass energy. The UA5 and ALICE data points at 900 GeV are slightly displaced horizontally for clarity. The dashed and solid lines (for INEL and NSD interactions respectively) indicate the fit using a power-law dependence on energy. [42]

noted above, there is good agreement between p-p and p-$\overline{p}$ data at the same energy. The dashed and solid lines (for INEL and NSD interactions respectively) are obtained by fitting the density of charged particles in the central pseudorapidity region with a power-law dependence on energy. Using this parametrization, the extrapolation to the nominal LHC energy of $\sqrt{s}$ = 14 TeV yields $dN_{ch}/d\eta = 5.5$ and $dN_{ch}/d\eta = 5.9$ for INEL and NSD interactions respectively. During 2010, the LHC come back to operate with$p$-p collision at $\sqrt{s}$ = 2.36 TeV and 0.9 TeV. This new data has been used to study the distribution of multiplicity of charged particles in the central pseudorapidity region ($|\eta| < 1.4$) as showed in Fig. 1.19.

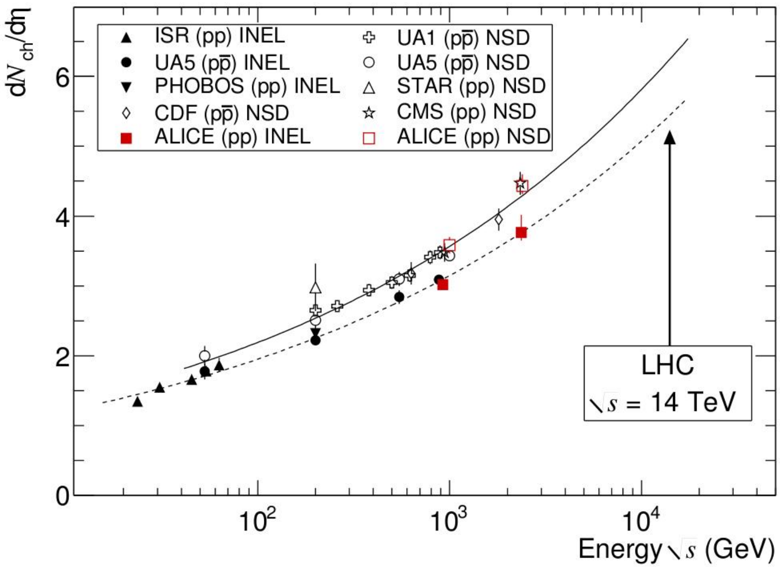

Figure 1.19: Charged-particle pseudorapidity density in the central rapidity region in proton-proton and proton-antiproton interactions as a function of the centre-of-mass energy. The dashed and solid lines (for INEL and NSD interactions, respectively) show a fit with a power-law dependence on energy. Note that data points at the same energy have been slightly shifted horizontally for visibility.[43]

Pb-Pb collisions : prediction for ALICE

Charged particle multiplicity at mid-(pseudo)rapidity is a first-day observable at the LHC. Many groups have produced such predictions for *Pb-Pb* collision, see a compilation in Fig.1.20 where 24 predictions are shown.

A rough classification, for mere organizational purposes, can be made into the following items:

1. Monte Carlo simulators of nuclear collisions. These models include many different physical ingredients to be combined in a consistent manner. They all take into account energy-momentum and quantum number conservation in a detailed way. While sometimes the physical ingredients are similar between different models, the details of the implementation lead to different results.

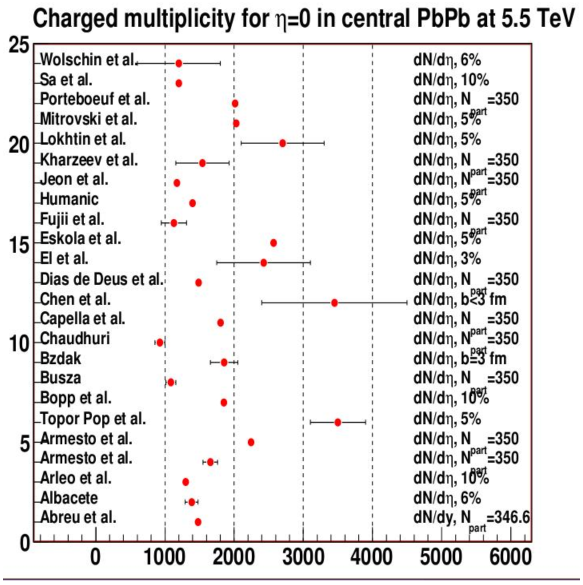

Figure 1.20: Predictions for multiplicities in central *Pb-Pb* collisions at the LHC. On the left the name of the authors can be found. On the right, the observable and centrality definition is shown. The error bar in the points reflects the uncertainty in the prediction. See the text for explanations. [101]

2. Models based on saturation ideas.

3. Data-driven predictions.

From the plots one can conclude that most predictions lie in the range 1000 $\div$ 2000. It should be noted than a value lower than 1000 could be, depending on the corresponding value for pp collisions , in conflict with participant scaling. On the other hand, a value larger than 2000 will be a challenge for saturation effects. Monte Carlo simulators, due to their complexity, do not include yet many recent theoretical developments, e.g. none implements saturation effects. This might be the reason why they tend to give the largest values [101]. Finally, multiplicities show a decreasing tendency with time from 1995 [102], through pre-RHIC predictions [103], until now.

Chapter 2

A Large Ion Collider Experiment

In order to study the elementary constituents of matter, and the interactions between them, particle physicists need to build machines that can accelerate and collide particles at increasingly higher energies. The *Large Hadron Collider* (**LHC**) [40], constructed at CERN, in the border region of France and Switzerland near Geneva, is the most powerful instrument ever built to investigate particles properties. The LHC is built into a tunnel with a circumference of approximately 27 km which was excavated for the Large Electron-Positron collider (LEP) which has been shut down in 2000. A schematic diagram of the LHC is shown in Fig. 2.1. The use of the LEP tunnel has been the main constraint for the 7 TeV beam energy for protons. The LHC can accelerate protons and ions.

2.1 Colliders features

In circular particle colliders, intense magnetic fields keep the particles in a circular trajectory. The particles are accelerated by radio frequency cavities where the particles pass by at each cycle. Two beams of particles are accelerated in opposite directions and brought to head-on collisions in the center of the experiments. The advantage over linear collisions is that the beam is stored and a high luminosity can be achieved. Compared to fixed target experiments colliders achieve a higher center-of-mass energy for the same beam energy. At particle colliders the experiments have to cover typically 4π steradians, since the produced particles are covering all directions. Particles moving in circular trajectory loose energy due to synchrotron radiation. While this effect has been very large at LEP, where electrons and positrons have been accelerated, it is much smaller at the LHC, since

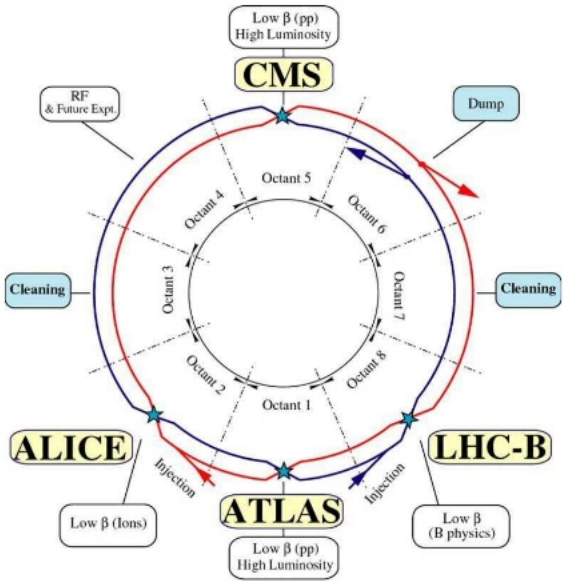

Figure 2.1: Schematic layout of the Large Hadron Collider (LHC). The four large LHC experiments (ATLAS, CMS, ALICE, LHCb) are shown. At their positions the two beams can be brought to collision. [40]

the proton mass is about 1800 times higher than the electron mass. The two main parameters for a particle accelerator are *luminosity* and *energy*.

2.2 The Large Hadron Collider

The LHC ring is made of eight sections. At the center of four of these sections are located the four major experiments. Two of these experiments are located at diametrically opposite high-luminosity insertion points: ATLAS at point 1 and CMS at point 5. The other two experiments are located at point 2 (ALICE) and point 8 (LHCb).
The tunnel houses 1232 superconducting dipole magnets that produce the magnetic field of 8.33 T necessary to circulate the beams. In order to achieve such a high magnetic field, the (N_bT_i) magnets are cooled to less than 2 K with superfluid helium at 1.9 K. What are the accelerating steps? First an ion source injects protons into an *Radio-Frequency* (**RF**) *cavity* where they are accelerated to 750

keV. These protons are then transmitted to a Linear Accelerator (**LINAC**) where they attain an energy of 50 MeV before being injected into the 1.4 GeV *Proton Synchroton* (**PS**) *Booster*. The PS accelerates the protons to 25 GeV and deliver a beam of 135 bunches with a 25 ns spacing (7.48 m) and containing 10^{11} protons each. The *Super Proton Synchroton* (**SPS**) takes over and accelerates the protons to 450 GeV before injection into the LHC as 2835 bunches of 10^{11} particles with the same bunch spacing. The two proton beams, which circulate in opposite direction, are combined in a *two-in-one* design whereby the beam pipes along with their corresponding coils are inserted in a single cryostat as shown in Fig. 2.2.

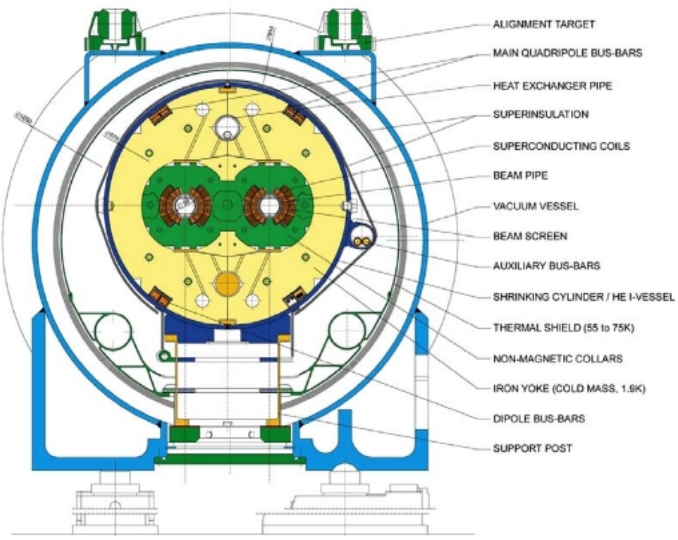

Figure 2.2: Cross-sectional view of an LHC dipole. The two beam pipes are seen in the center, each surrounded by superconducting coils in orange. [40]

Different phases are foreseen for the operation of the LHC. For protons, during the first few years of operation (called the *low luminosity* phase), the nominal luminosity is expected to reach $2\times\ 10^{33}\ \mathrm{cm}^{-2}\mathrm{s}^{-1}$. The luminosity should then increase to its designed nominal value of $10^{34}\ \mathrm{cm}^{-2}\mathrm{s}^{-1}$(*high luminosity* phase). Heavy ion collisions were included in the conceptual design of the LHC from an early stage, and collisions between beams of fully stripped lead ions ($^{208}Pb^{82+}$) are scheduled for fall 2010. These ions will have a beam energy of 2.76 TeV/nucleon, yielding a total center-of-mass energy of 1.15 PeV and a nominal luminosity of $1.0\times10^{27}\text{cm}^{-2}\text{s}-1$. Collisions between ion beams willbe provided principally at Interaction Point 2 for the specialized ALICE detector. While the major hardware system of the LHC ring appear compatible with heavy ion operation, the beam dymanics and performance limits with ion beams are quite different from those of protons. The LHC also enters new territory where, for example, the copius nuclear electromagnetic interaction in peripheral collisions of the ions can directly limit luminosity and beam lifetime: this phenomena become critical in the LHC because of the combination of its unprecedented energy and superconducting magnet tecnology.

LHC parameters for lead ions

Some aspects of heavy ions beams are similar to those of proton beams. For example, the nominal emittance of the ions has been choosed so that the ion beams have the some geometric size as the nominal proton beams (at beam energies corresponding to the same magnetic field in the dipole magnets). Thus, the most basic considerations of beam size and aperture will be the same as for protons, implying that this is a safe operational value. Despite this, the physics of ion beams is qualitatively and quantitatively different from that of proton and the values of some parameters are necessarily very different. For lead ions programs there are two foreseen scheme : *Nominal* and *Early*. A peak luminosity of $1.0\times 10^{27}\text{cm}^{-2}\text{s}^{-1}$ has been the overall performance goal for lead ions for some time but the first period of operation of the LHC as a lead-lead collider will be carried out with fewer bunches and a lower luminosity. These relaxed parameters will provide more margin against some of the performance limitations, namely those that depend on the total beam current. The reduced luminosity will nevertheless give access to important physics. The parameters at collision energy for the two schema are given in table 4.8.2.

2.2.1 LHC experiments

The two particle beams circulating with opposite directions in the LHC rings collide in 4 different locations, where the scattering products are detected by six experiments:

- **ALICE** (*A Large Ion Collider Experiment*), the only experiment specifically dedicated to heavy-ion collisions. It will be deeply described in the next chapter.

Beam Parameter	Nominal	Early
Lead ion energy [TeV]	574	574
Lead ion energy per nucleon [TeV]	2.759	2.759
Number of ions per bunch	7.0×10^7	7.0×10^7
Number of bunches	592	62
RMS beam size at IP2 [μm]	15.9	22.5
Peakluminosity at IP2 [$cm^{-2}s^{-1}$]	1.0×10^{27}	5.4×10^{25}

Table 2.1: LHC beam parameters in Nominal Ion Scheme and Early Ion Scheme. [40]

- **ATLAS** (*A Toroidal LHC ApparatuS*), a general purpose experiment focused on the searching of the Higgs boson, as well as on physics beyond the Standard Model.
- **CMS** (*Compact Muon Solenoid*), with analogous purposes of ATLAS.
- **LHCb** (*Large Hadron Collider beauty*), focusing on beauty detection for precise measurements of CP violation and rare decays.
- **LHCf** (*Large Hadron Collider forward*), an experiment sharing the interaction point with ATLAS and using the forward particles created at the LHC as a source to simulate cosmic rays in laboratory conditions.
- **TOTEM** (*TOTal and Elastic Measurement*), an experiment sharing the interaction point with CMS for total cross sections, elastic scattering and diffractive dissociation measurements.

2.3 ALICE

The **ALICE** [41] experiment is the unique that has been optimized for heavy ion collider physics. It is a multi purpose experiment and its project was driven by the requirement of having a good particle identification from low momenta ($\sim$100 MeV/c) up to high momenta ($\sim$100 GeV/c) in a high multiplicity scenario ($\sim$8000 particle per unit rapidity at midrapidity). The layout of its structure is shown in Fig. 2.3.

Its has a central barrel with a full azimuthal coverage and a rapidity coverage in the interval $|\eta| \leq 1$ and a series of detectors which cover part of the large

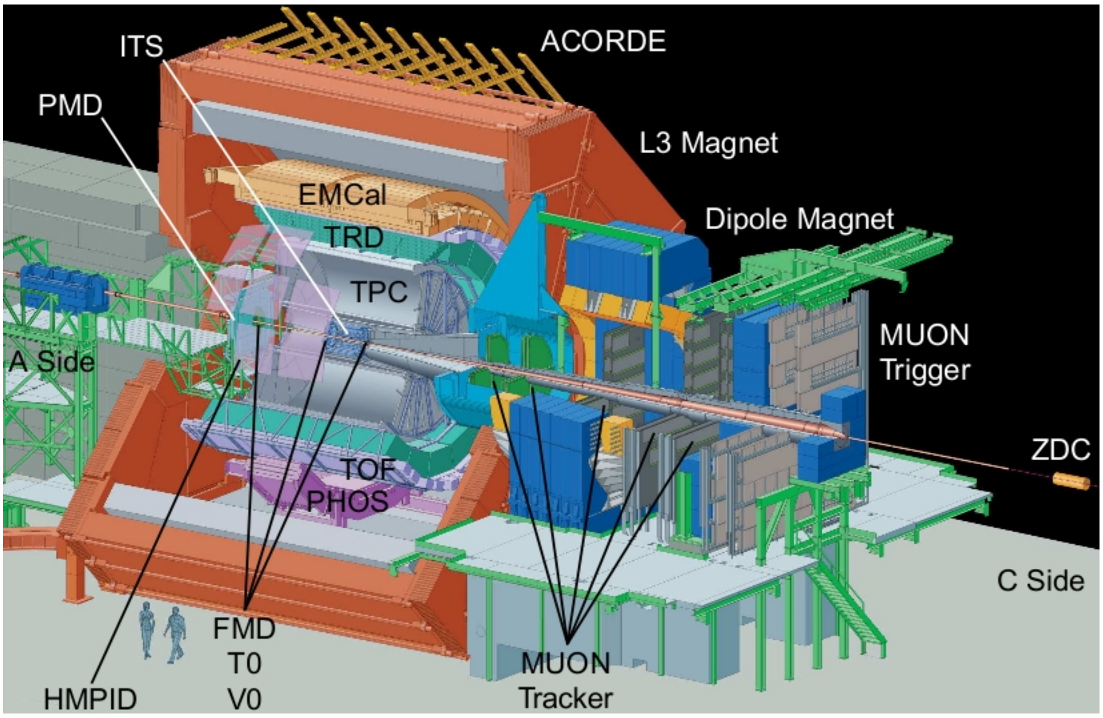

Figure 2.3: Layout of ALICE detector.

rapidity region. In the central part, starting from smaller to bigger radii, there are the *Inner Tracking System* (**ITS**), the *Time Projection Chamber* (**TPC**), the *Transition Radiation Detector* (**TRD**) and the *Time Of Flight* (**TOF**). This central system has other two small area detectors in the outer part : the *HIgh Momentum Particle IDentification* (**HMPID**) in the solid angle $|\eta| < 0.6$ and $\Delta\phi = 60°$, and the *PHOton Spectrometer* (**PHOS**) in the solid angle $|\eta| < 0.12$ and $\Delta\phi = 100°$. The remaining large rapidity detectors are the *Muon Spectrometer* at $-4.0 < |\eta| < -2.4$ and, on the opposite site, in the large rapidity region (up to $\eta = 5.1$) *a Photon Multiplicity Detector* (**PMD**) and a *Forward Multiplicity Detector* (**FMD**). The innermost and the outermost detectors provide the rapidity coverage shown in Fig. 2.4.

Other detectors were designed to give fast trigger signals (**T0** and **V0**) or to measure the impact parameter of an ion-ion collision as the *Zero Degree Calorimeter* (**ZDC**, an hadronic calorimeter) and the very forward electromagnetic calorime-

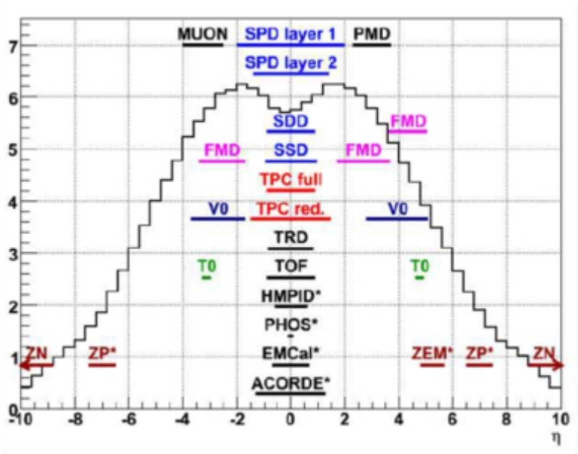

Figure 2.4: Pseudo rapidity coverage of the ALICE detectors.

ter (**ZEM**). Several measured observables are related to the event centrality and such hadronic and electromagnetic calorimeters will provide the measures for it.
The whole central part of the ALICE experiment is inside the *L3 magnet*, that is a magnet yoke earlier installed for the L3 experiment at LEP. It can provide a magnetic field up to 0.5 T. Another magnet is present in the ALICE experiment for muons, named *Muon Dipole*, that can provide a magnetic field of 3 T.
The experiment will have a unique capability of identifying particles and will be given a small description of the ALICE detectors as well as their contribution to its physics program in the next sections. A summary of the particle identification potential with the ALICE detectors can be found in Fig. 2.5 .

ALICE and LHC

One of the most important experimental issues in the design of the ALICE experiment and of its physics programme is the luminosity for *Pb-Pb* collisions. It depends on the limitations imposed by both the detector and the accelerator. Among the sub-detectors, the most constraining limits come from the main tracking device, the Time-Projection Chamber (TPC), and the forward muon spectrometer. The TPC limits the maximum usable luminosity because of event pile-up during the 88 μs drift time. The TPC is expected to be operated even at luminosities above 10^{27} cm^{-2} s^{-1} , given that the multiplicity in the *Pb-Pb* collisions will re-

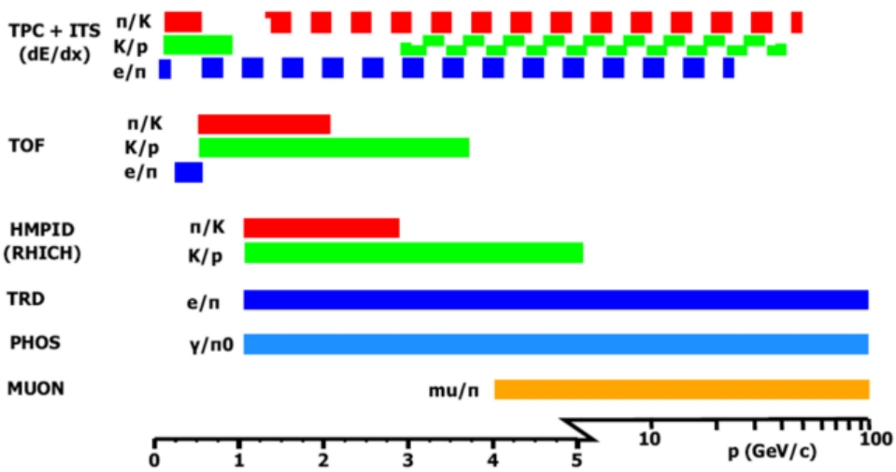

Figure 2.5: Momentum identification ranges with ALICE, for different charged particles.

main around 4000 per unit of pseudo-rapidity. On the other hand, the maximum acceptable rate capability of the muon spectrometer trigger chambers limit the luminosity to (2-4) $\times$ 10^{28} cm^{-2} s^{-1}. However, the limitations of the LHC are stronger than those imposed by the sub-detectors technologies.

2.3.1 The Inner Tracking System

The Inner Tracking System [**?**] , shown in Fig. 2.6 is placed close to the interaction point and it has been designed to accomplish some tasks which result crucial for the ALICE physics programme. These task are:

- to reconstruct the primary vertex with a resolution better than 100 μm; to reconstruct the secondary vertices and to measure the impact parameter for the decays of hyperons and D and B mesons;
- to track and identify the low-p_T ($<$ 100M eV) particles, which are not seen from the outer detectors;
- to improve the TPC momentum resolution for the high-p_T particles;
- to track and identify the particles traversing the dead zones of the TPC.

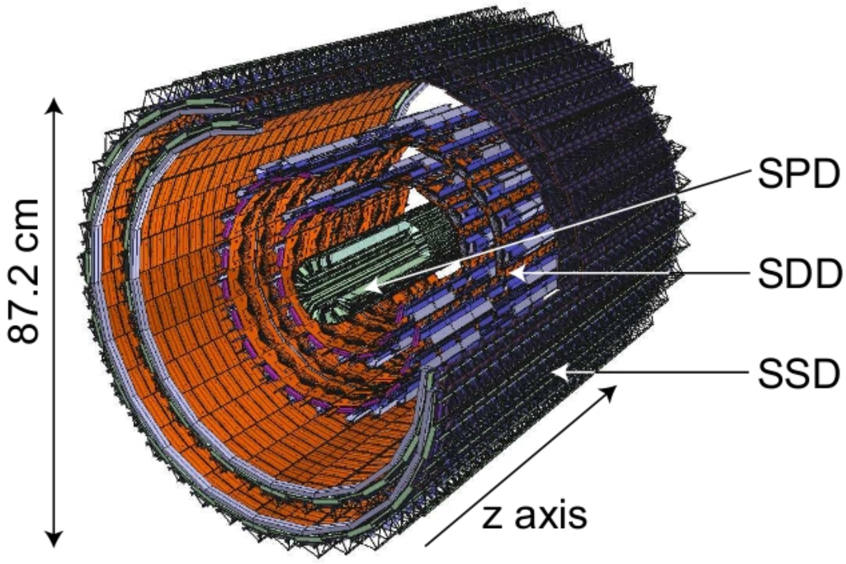

Figure 2.6: Layout of ITS. [105]

Moreover, in cooperation with the other detectors, the ITS characteristics allow to improve the performances in the study of many ALICE physics topics: the global observables of the heavy-ion collisions, like the charged particle multiplicity and the particle spectra and correlations; the resonance production and possible variations in their parameters; a precise mass measurement of the heavy-quark states to improve the signal-to-background ratio for the observation of the quarkonia suppression; the jet observation, covering also the TPC dead zones.
These tasks will be accomplished by the ITS thanks to its design and construction characteristics, which are described hereafter: it consists of six concentric cylindrical layers of silicon detectors, the innermost of them located at a radius r = 3.9 cm, the outermost at r = 43.9 cm (Fig. 2.3.1), and it is placed inside the Time Projection Chamber.
The number, position and segmentation of the layers are optimized for efficient track reconstruction and high impact parameter resolution. In particular, the overall ITS dimensions are constrained by the geometry of the neighbouring parts of the ALICE apparatus: the inner radius is the minimum allowed by the beam pipe, a 800 μm-thick beryllium cylinder of 6 cm outer diameter, coaxial with the ITS

detector layers; the outer radius is instead determined by the necessity to match the reconstructed tracks with those from the TPC.
The layers dimensions along the beam axis allow to cover a rapidity range of $|\eta| < 0.9$ for all vertices located within the length of the interaction diamond, i.e. $\pm 1\sigma = \pm 10.6$ cm along the beam direction. The first layer covers a more extended range ($|\eta| < 1.98$) in order to provide, together with the FMD, a continuous coverage in rapidity for the measurement of the charged-particles multiplicity.
The two innermost layers, called *Silicon Pixel Detector* (**SPD**), have to sustain a very high rate of up to 50 particles per cm^2 are based on hybrid silicon pixels which consist of silicon detector diodes with a thickness of 200 μm. The first and the second layer are placed at 3.9 cm and 7.6 cm, respectively. In total 9.8 million channels are read out in a binary fashion, thus no energy loss information is available and therefore the SPD does not contribute to particle identification. The information from the SPD alone is sufficient to form so-called ***tracklets*** and thus to measure the charged-particle multiplicity.
The third and fourth layer, called *Silicon Drift Detector* (**SDD**), consist of a 300 μm thick layer of homogeneous high-resistivity silicon. Contrarily to the first two inner layers, the readout is analog, therefore energy-loss information for particle identification is provided. The SDD has 133 000 channels. The detector employs a drift time measurement resulting in a similar granularity as the SPD and SSD. The two outermost layers, called *Silicon Strip Detector* (**SSD**), consist of sensors equipped on both sides with silicon micro-strips. These are arranged under a stereo angle of 35 mrad allowing for a two-dimensional measurement of the track position together with an energy-loss measurement for particle identification. The SSD has about 2.6 million channels.
In Fig. 2.7 one of the first *p-p* collisions events as recorded in the six layers of ITS detector on 23th November 2009. [106]

2.3.2 The Time Projection Chamber

The foreseen ALICE physics program determined the performance requirements as well as the design details and the technical construction of the ALICE TPC [107]. To improve the knowledge of hadron physics the following challenges had to be engaged:

- The dE/dx resolution should be at least 8% or better to properly identify particles.

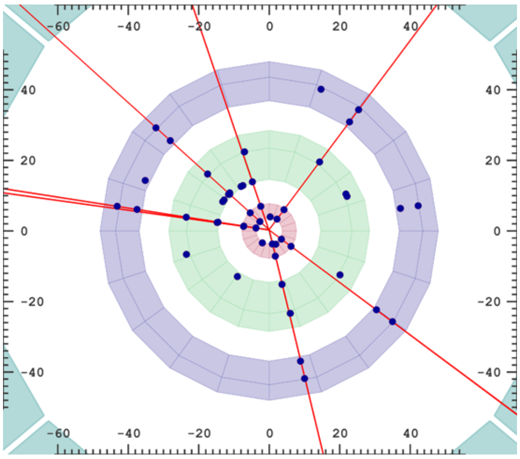

Figure 2.7: ALICE first *p-p* event recorded in ITS. [106]

- The two track resolution has to be sufficient to allow measurements with a resolution in relative momentum of a few ($\leqslant$ 5) MeV.
- For fast decaying particles a proper (85% - 95%) matching capability of the TPC to ITS or/and TOF is needed.
- A tracking efficiency of at least 90 % for tracks of higher momentum ($\geqslant$ 1 GeV) should be achieved.
- To get a good mass resolution ($\leqslant$ 100 MeV) for heavy mesons, the momentum resolution for electrons of about 4 GeV should be at least 2.5 %.
- Due to the high luminosity of heavy-ion collisions, the TPC has to operate at 1 kHz or more.

These demands lead to a design of a conventional TPC, but with many new features and novel solutions. The major improvements are [107]:

Material budget: In order to minimize the effect of multiple scattering and secondary particle production, the amount of material between the inner TPC cylinder and the ITS detector was minimized. This has determined the light field cage material and influenced the gas choice.

Rate capability: The dead time (between read out) of the TPC had to be optimized. This influenced again, the gas choice, the drift field configuration and therefore the field cage.

Acceptance: For event-by-event studies as well as for all rare observables a reasonably big acceptance was necessary to collect enough statistics. This has led, in combination with the reused L3 magnet, to the biggest TPC *ever* built.

Read-out: The concept of signal handling has been significantly improved by the novel development of a specially designed read-out chip.

The ALICE TPC is placed inside a L3 magnet parallel to the drift field in z direction. It has an inner radius of 80 cm, defined by the maximum acceptable hit density of 0.1 cm^{-2} and the outer diameter of the ITS detector.

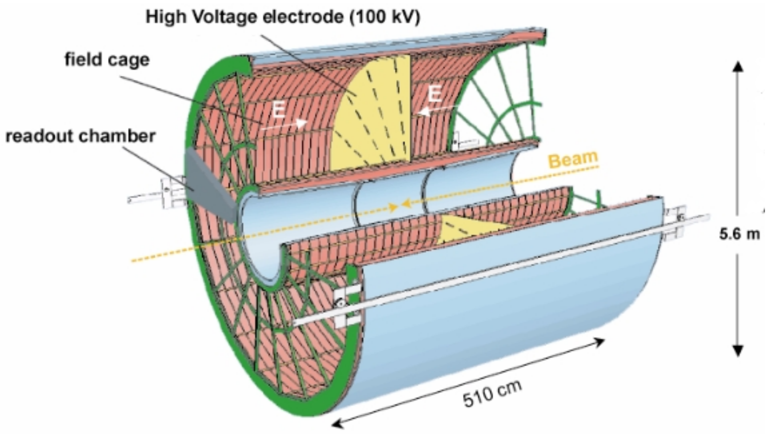

Figure 2.8: Layout of the ALICE TPC.

The outer radius of 250 cm is given by the length required for the desired dE/dx resolution as well as the required momentum resolution in the frame of the available magnetic field. To fulfill the desired position resolution ($\sigma_{r\phi} \approx 150\ \mu$m and $\sigma_z \approx 200\ \mu$m) special precautions had to be taken when planning the field cage as well as the inner and outer containment vessels. The total length of the TPC is 500 cm.
The drift gas of Ne-CO_2-N_2 is optimized for drift speed, low diffusion, low radiation length and multiple scattering and aging properties. The drawback of this

mixture is that it has an unusually high dependence of drift velocity on temperature. Thus, the ALICE TPC is aiming for a thermal stability of $\Delta T \leqslant 0.1$ K. The drift gas requires a high drift field (400 V/cm) to secure an acceptable drift time of 96 μ which defines the dead-time of the detector and therefore the rate capability. To reach this high drift field the central electrode must be at 100 kV. Multi-wire proportional chambers with cathode pad readout are mounted into 18 trapezoidal sectors of each end-plate.

2.3.3 The Transition Radiation Detector

The task of the ALICE Transition-Radiation Detector [108] is to provide electron identification in the central barrel for momenta greater than p = 1 GeV/c, where the pion rejection capability through energy loss measurement in the TPC is no longer sufficient.
TRD covers in pseudo-rapidity the same region of the other central barrel detectors, $|\eta| \leqslant 0.9$. The TRD fills the radial space between the TPC and the TOF detectors. For quality of electron identification, the TRD consists of six individual layers. To match the azimuthal segmentation of the TPC, there are 18 sectors. There is a 5-fold segmentation along beam direction. In total there are $18\times5\times6$ = 540 detector modules. Each module consists of a radiator of 4.8 cm thickness, a multi-wire proportional readout chamber, and the front-end electronics for this chamber. In Fig. 2.9 the cross-sectional (r- z plane) view of one TRD chamber showing the passage of a pion/electron has been shown.

Each chamber has 144 pads in the direction of the amplification wires, r, and between 12 and 16 pad rows in the z direction. The pads have a typical area of 6-7 cm^2 and cover a total active area of about 736 m^2 with 1.16×106 readout channels. The gas mixture in the readout chambers is Xe/CO_2 (85%/15%). Each readout chamber consists of a drift region of 3.0 cm separated by cathode wires from an amplification region of 0.7 cm. The drift time is 2.0 μs, requiring a drift velocity of 1.5 cm/μs. The nominal drift velocity will be reached with an electric field of 0.7 kV/cm. In this gas mixture a minimum ionizing particle liberates 275 electrons cm^{-1} .

2.3.4 Time-Of-Flight detector

The TOF detector is a large area array for particle identification in the intermediate momentum range through the measurement of the time that particle spend to come

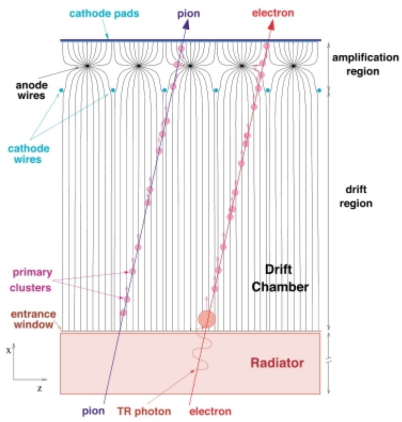

Figure 2.9: Cross-sectional (r- z plane) view of one TRD chamber showing the passage of a pion/electron. [109]

from the interaction point to the detector sensible surface. Coupled with the ITS and TPC it provides an event-by-event identification of large samples of pions, kaons and protons. A comprehensive review of the Time-Of-Flight detector of ALICE will be given in next chapter.

2.3.5 High-Momentum Particle Identification Detector

The High-Momentum Particle Identification Detector [110], is dedicated to inclusive measurements of identified hadrons for $p_T > 1$ GeV/c. The HMPID was designed as a single-arm array with an acceptance of 5 % of the central barrel phase space. The geometry of the detector was optimized with respect to particle yields at high-p_T in both pp and heavy-ion collisions at LHC energies, and with respect to the large opening angle (corresponding to small effective size particle emitting sources) required for two-particle correlation measurements. HMPID will enhance the PID capability of the ALICE experiment by enabling identification of particles beyond the momentum interval attainable through energy loss and time-of-flight measurements . The detector was optimized to extend the useful range for π/K and K/p discrimination, on a track-by-track basis, up to 3 and 5 GeV/c respectively.
The HMPID is based on proximity-focusing *Ring Imaging Cherenkov* (RICH) counters and consists of seven modules of about $1.5\times1.5\text{m}^2$ each, mounted in

an independent support cradle, that will be fixed to the space frame in the two o'clock position. The radiator is a 15 mm thick layer of low chromaticity $C_6 F_{14}$ (perfluorohexane) liquid with an index of refraction of n = 1.2989 at λ = 175 nm corresponding to β_{min} = 0.77 (i.e. a momentum threshold p_{min} = 1.21 m, where m is the particle mass).
Cherenkov photons, emitted when a fast charged particle traverses the radiator, (see Fig. 2.3.5) are detected by a photon counter which exploits the technology of a thin layer of CsI deposited onto the pad cathode of a Multi-Wire Pad Chamber. The photo-detector, filled with pure methane and operated at ambient temperature and pressure, is closed on one side by an end-flange which supports six independent CsI photocathode boards, 64×40 cm^2 large, segmented into pads of 8×8.4mm^2 . On the opposite side, a honeycomb panel supports three $C_6 F_{14}$ radiator vessels placed at a distance of 80 mm from the anode wire plane and separated from CH_4 by a quartz window. The photo-converter is a 300 nm thick layer of CsI deposited onto printed circuit boards with a copper layer.
Each HMPID module consists of a stack of five independent frames made out of a stabilized aluminium alloy (peralumin) which minimizes out-gassing into the chamber active volume. The thickness and size of the materials have been carefully optimized by investigating the best compromise between the detector total radiation length and the perfluorohexane hydrostatic pressure.
The total HMPID gas volume of 1.4 m^3 of pure CH_4 is split into the seven independent RICH modules of 0.2 m^3 by supplying each of them individually with a gas flow rate providing five volume changes per day and maintaining an operating pressure of some mbar above ambient pressure. With the help of Monte Carlo simulation and test beam measurements, it was demonstrated [111] that a radiator thickness of 15 mm will enable operating the detector at a lower gain, keeping unchanged the performance and improving the stability of operation.

2.3.6 The PHOton Spectrometer

The PHOton Spectrometer [41] is a high-resolution electromagnetic spectrometer covering a limited acceptance domain at central rapidity. The PHOS is capable to measure low-p_T photons emitted in the initial phase of the collision, in order to study its thermal and dynamical properties; moreover, it is designed to measure the high-p_T π^0 and γ-jet correlation in order to study the jet quenching effects.

It is one of the outermost detectors at a distance of 460 cm from the interaction point. The final configuration holds five modules with an angular coverage of

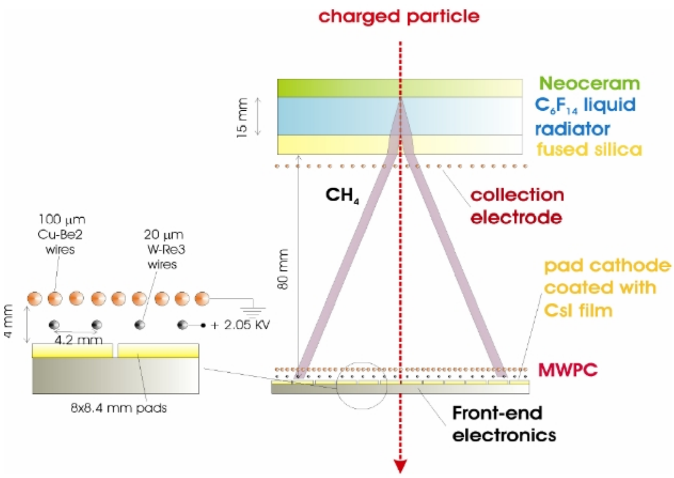

Figure 2.10: Schematic picture of the layout of a HMPID module and how it operates.

5×20 degrees, as shown in Fig. 2.11 (*right*). The pseudo rapidity coverage is -0.12 to 0.12.

Figure 2.11: *Left*: PHOS crystal detector unit with glued photo-detector; *right*: PHOS module.

Each PHOS module is built up of two different sub-detectors. The main detector is a highly segmented ElectroMagnetic Calorimeter (EMC), while the second detector is a Charged Particle Veto (CPV) detector. The EMC is measuring electromagnetic showers of up to 100 GeV via a large matrix of $PbWO_4$ crystals. The EMC for one PHOS module is segmented into 3584 detection cells, that each consists of a crystal and an avalanche photo diode (Fig. 2.3.6,*left*). To increase the light yield and hence the energy resolution of the $PbWO_4$ crystals, the nominal operating temperature of the EMC modules are set to -25°C. The crystal strips are located in a cold enclosure, whereas the front end cards are located outside this enclosure. The CPV detector is a Multi Wire Proportional Chamber that is placed on top of the EMC module with a distance of about 5 mm. The purpose is to discriminate charged particles from neutral particles.

2.3.7 The ElectroMagnetic Calorimeter

The construction of a large ElectroMagnetic Calorimeter (EMCal) [41] began in 2008 with the aim to enable ALICE to explore in detail the physics of jet quenching over the large kinematic range accessible in heavy ion collisions at the LHC [112]. The EMCal is a large Pb-scintillator calorimeter located adjacent to the ALICE magnet coil at a radius of ∼4.5 metres from the beam line. It covers $|\eta| \leqslant 0.7$ and $\Delta\phi$ =107°, and is positioned approximately opposite in azimuth to the ALICE Photon Spectrometer (PHOS) calorimeter. The overall design of the EMCal was heavily influenced by its location within the ALICE L3 magnet. Figure 2.12 shows a schematic integration drawing of the end view of the ALICE central barrel.

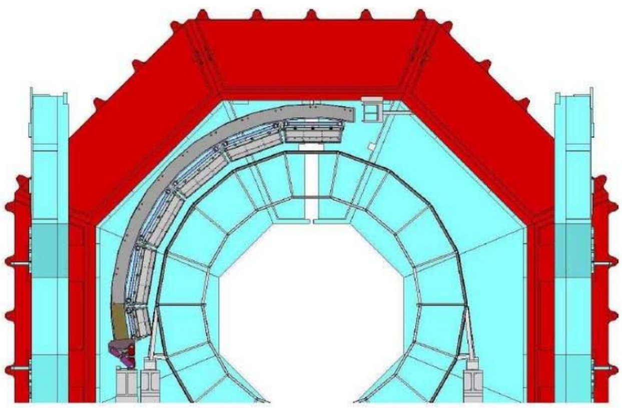

Figure 2.12: Schematic view of EMCal detector in the ALICE central barrel.

The choice of an electromagnetic calorimeter with large acceptance and moderate resolution provides a cost-effective pathway into jet physics in ALICE. The EMCal increases the electromagnetic calorimeter coverage of ALICE by nearly an order of magnitude. It provides a fast and efficient first level trigger for hard jets, photons and electrons, allowing ALICE to exploit fully the luminosity of the LHC. The EMCal also measures the neutral energy component of jets, enabling full jet reconstruction in all collision systems, from proton-proton to *Pb-Pb*. The combination of the EMCal with the excellent ALICE charged particle tracking capabilities and the modest ALICE magnetic field strength, is a preferred configuration for jet reconstruction in the high background environment of heavy ion collisions, allowing the optimisation of background rejection while preserving the crucial jet-quenching signals at moderate transverse momentum.

2.3.8 The ALICE COsmic Ray DEtector

The ALICE COsmic Ray DEtector (**ACORDE**) consists of 60 large scintillators placed on the upper surface of the L3 magnet, as showed in Fig. 2.13, that are used as fast level trigger on cosmic rays. The detection of single atmospheric muons and multi-muon events allows high-energy cosmic rays to be studied, which can provide insight into the energy region of the knee in the cosmic-ray spectrum.Furthermore, cosmic-ray events are used for calibration and alignment. ACORDE has been used during the detector commissioning in 2007, 2008 and 2009. The rate of muons reaching the ALICE detector is about 4.5 Hz/m^2 .
ACORDE's scintillators have been used before by the DELPHI (Detector with Lepton, Photon, and Hadron Identification) experiment.

2.3.9 The Muon Spectormeter

Muon detection is performed in the pseudo-rapidity region 4.0 $< \eta <$-2.5 by the Muon Spectrometer. With this detector, the complete spectrum of heavy quark vector mesons resonances (i.e. J/Ψ,Ψ', Υ,Υ',Υ''), as well as the ϕ meson, will be measured in the $\mu^+\mu^-$ decay channel. The simultaneous measurement of all the quarkonia species with the same apparatus will allow a direct comparison of their production rate as a function of different parameters such as transverse momentum and collision centrality. In addition to vector mesons, the unlike-sign dimuon continuum up to masses around 10 GeV/c^2 will be measured. Since at LHC energies the continuum is expected to be dominated by muons from the semi-leptonic decay of open charm and open beauty, it will be possible to study the production of open heavy flavour with the Muon Spectrometer. Heavy flavour production in the region -2.5 $< \eta <$-1 will be accessible through measurement of

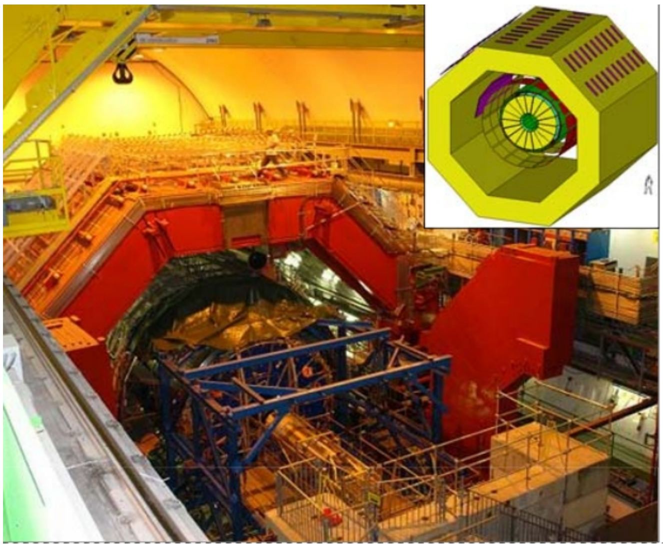

Figure 2.13: The ALICE Cosmic Ray Detector: the scintillator array is on the three top faces of the magnet.

e -μ coincidences, where the muon is detected by the Muon Spectrometer and the electron by the TRD. The layout of the Muon Spectrometer is shown in Fig.2.14.

The spectrometer consists of the following components: a passive front absorber to absorb hadrons and photons from the interaction vertex; a high granularity tracking system of 10 detection planes; a large dipole magnet; a passive muon-filter wall, followed by four planes of trigger chambers; an inner beam shield to protect the chambers from primary and secondary particles produced at large rapidities. The front absorber, whose length is 4.13 m, is located inside the solenoid magnet. The fiducial volume of the absorber is made predominantly out of carbon and concrete to limit small-angle scattering and energy loss by traversing muons. The spectrometer is shielded throughout its length by a dense absorber tube, surrounding the beam pipe, that is made of tungsten, lead and stainless steel. While the front absorber and the beam shield are sufficient to protect the tracking chambers, additional protection is needed for the trigger chambers. For this reason the muon filter, i.e. an iron wall 1.2 m thick is placed after the last tracking chamber, in front of the first trigger chamber.

The tracking chambers were designed to achieve a spatial resolution of about 100 μm, necessary for an invariant-mass resolution of the order of 100 MeV/c^2 at the

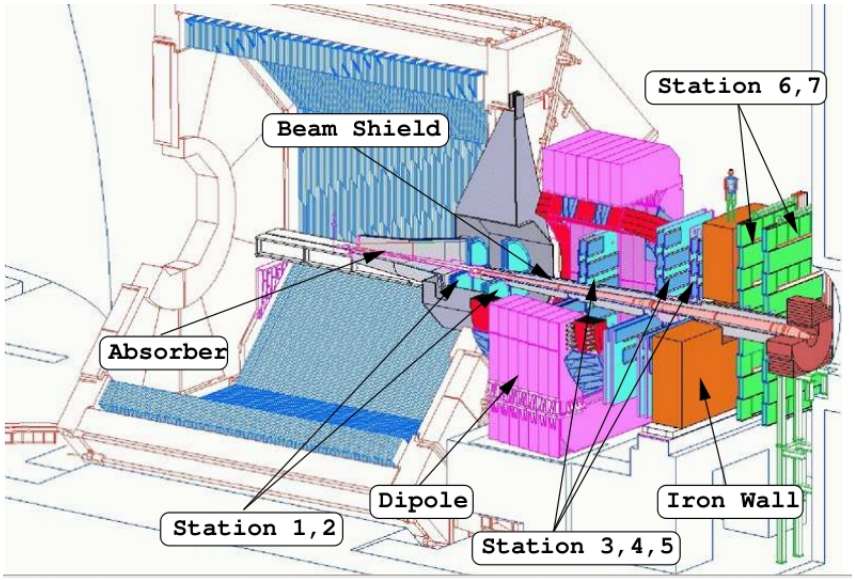

Figure 2.14: Schematic 3D view of ALICE Muon Spectrometer.

Υ mass [113]. In addition they have to be able to operate at a hit density of about 5×10^{-2} cm^{-2} expected in central PbPb collisions. All these requirements were fulfilled by the use of cathode pad chambers. They are arranged in five stations: two are placed before, one inside and two after the dipole magnet. Each station is made of two chamber planes. Each chamber has two cathode planes, which are both read out to provide two-dimensional hit information
The dipole magnet [114] is placed 7 m from the interaction vertex, at some 10 cm distance from the L3 solenoid. The size (free gap between poles 3.5 m, total weight about 900 t) is defined by the requirements on the angular acceptance of the spectrometer.
In table 2.2, the principal features of the so far described ALICE detectors have been summarized.

2.3.10 Forward and trigger detectors

Finally, some small specialized detectors are used for triggering the ALICE acquisition or to measure global properties of the events:

Photon Multiplicity Detector (PMD) is a preshower detector measuring the multiplicity and spatial ($\eta - \phi$) distribution of photons on an event-by-event basis, in the forward region ($2.3 < \eta < 3.7$). Placed at about 360 cm from the interaction point, in the side opposite to the Muon Spectrometer, the PMD provides estimates of the transverse electromagnetic energy and of the reaction plane on an event-by-event basis. It consists of two identical planes of detectors, made of gas proportional counters with honeycomb structure and wire readout, with a $3X_0$ thick lead converter in between them: the front detector plane is used for vetoing charged particles while the detector plane behind the converter is the preshower plane and registers hits from both photons and charged hadrons.

T0 detector consists of two arrays of Cherenkov counters, with a time resolution better than 50 ps, asymmetrically placed at 72.7 cm (Muon spectrometer side) and 375 cm (PMD side) from the interaction vertex, with a pseudo-rapidity coverage of $-3.28 < \eta < -2.97$ and $4.61 < \eta < 4.92$, respectively [41]. It is designed to provide a T0 signal for the TOF detector, to measure the vertex position with a precision of ± 1.5 cm, thus providing a first level trigger when the position is within the preset values, and to measure the particle multiplicity and generate a centrality trigger.

V0 detector, consisting of two arrays of segmented scintillator counters, located 90 cm (Muon Spectrometer side) and 340 cm (PMD side) from the interaction point. The detectors are segmented into 72 elementary counters distributed in 5 rings, with a pseudo-rapidity coverage of $-3.8 < \eta < -1.7$ and $2.8 < \eta < 5.1$. The measurement of the time-of-flight difference between the detectors allows to identify and reject the beam-gas events, thus providing a minimum bias trigger for the central barrel detectors and a validation signal for the muon trigger. Moreover, the V0 can measure the charged particle multiplicity, thus resulting in a centrality indicator providing two centrality triggers in *Pb-Pb* collisions.

Forward Multiplicity Detector (FMD), consisting in rings of silicon strip detectors located at three different positions along the beam pipe, provides a charged particle multiplicity information in the pseudorapidity range $-3.4 < \eta < -1.7$ (Muon Spectrometer side) and $1.7 < \eta < 5.1$ (PMD side). The FMD consists of 51200 silicon strips channels distributed over 5 ring counters of two types: the inner ring is composed by 20 sectors in azimuthal angle with 512 strips each; the outer by 40 sectors with 256 each. The design ensures, together with the ITS inner pixel layer, a full pseudo-rapidity coverage in the range -3.4 $< \eta <$ 5.1, and an overlap between the FMD and ITS pixel system of about 0.2 pseudorapidity units.

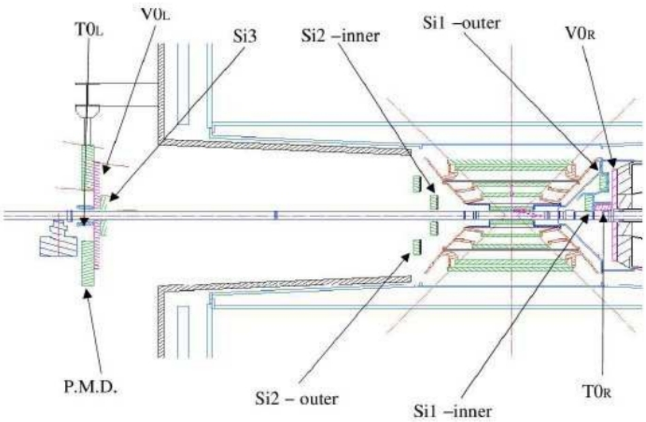

Figure 2.15: Location of the ALICE forward detectors V0, T0, PMD and of FMD modules Si1, Si2 and Si3 along the LHC beam line. The location of the PMD corresponds to the L3 magnet door.

Zero Degree Calorimeter (ZDC) provides a centrality estimation and trigger in *Pb-Pb* collisions by measuring the energy carried in the forward direction (at zero degrees relative to the beam direction) by non-interacting (spectator) nucleons. The detector consists of two pairs of quartz-fibers hadronic calorimeters (for neutron and protons), placed on both sides of the interaction point, at 116 m from it. The system is completed by two electromagnetic calorimeters (**ZEM**), both placed at about 7 m from interaction point (PMD side), which allow to resolve ambiguities in the determination of the centrality. Being placed between the beam pipes, the neutron calorimeter (**ZN**) has the most severe geometrical constraints: the transverse dimensions have to be smaller than 7 cm, requiring a very dense passive material (tungsten). The stringent space constraints do not hold for the proton calorimeter (**ZP**), which is made with a less dense material (lead). The ZN, segmented in four regions, can also provide an estimation of the reaction plane. The electromagnetic calorimeter (ZEM), made of lead and quartz fibres, is designed to measure the energy of particles, mostly photons generated from π^0 decays, at forward rapidities ($4.8 < \eta < 5.7$). Differently from the ZN and ZP, the ZEM fibres are oriented at 45°, a choice that maximizes the detector response.

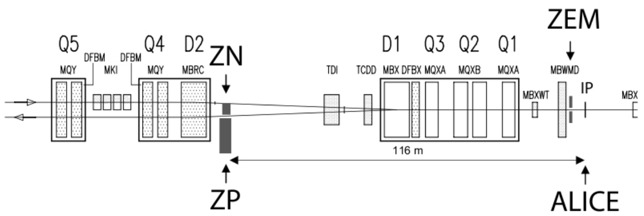

Figure 2.16: Location of the ALICE Zero Degrees Calorimeters ZN znd ZP along the LHC beam line.

2.3.11 The AliRoot Framework

The project for the ALICE offline framework, **AliRoot** [41, 115], started in 1998 [116] and has been continuously developed by the offline core team and collaboration members. AliRoot is entirely based on Object Oriented technology (C++) and depends on the **ROOT** [117] framework, which provides an environment for the development of software package for *event generator*, *detector simulation*, *event reconstruction*, *data acquisition* and *analysis*. The final objectives of the AliRoot framework are:

- the simulation of the primary hadronic collisions and the resulting detector response, i.e. the reconstruction of the physics data (raw data) coming from simulated and real events.

- the (distributed) analysis of reconstructed data.

The AliRoot design was guided by the basic principles of reusability and modularity, which minimize the amount of user code unused or rewritten and maximize the participation of the physicists in its development.

The core of the system is the STEER module, which provides steering, run management, interface classes and base classes. The codes from the different detectors are independent so that different detector groups can work concurrently on the system while minimizing the interference. The use of an Object Oriented programming language, allowing a defined class hierarchy, realizes the modularity structure in a natural way. The hadronic collision can be simulated with different Monte Carlo event generators, like, for example, **PYTHIA** [118] and **HIJING** [119], which are interfaced to the framework in a completely transparent way to the users. The detector response simulation follows the same logic, allowing the user to switch among different transport packages like **GEANT3** [120], **GEANT4** [121] and **FLUKA** [122], without changing the code: only a different shared library has to be loaded. The basic concept of the framework is shown schematically in Fig. 2.17.

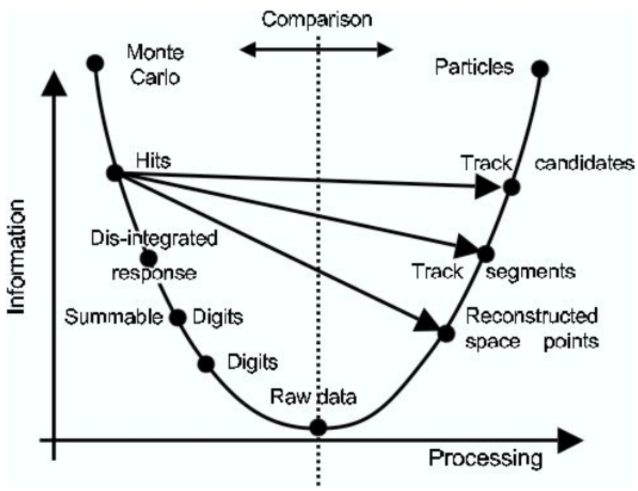

Figure 2.17: The role of AliRoot framework.

The left branch of the curve represent the *simulation phase*: the Monte Carlo truth is degraded to reproduce the detector response. On the contrary, the right branch is the *reconstruction phase*: the real or simulated data are reconstructed in order to retrieve back the kinematics of the detected particles.
The primary interactions are simulated via event generators and the resulting kine-

matic *tree*[1] is then used in the transport package. The tree contains the produced 'particles', defined through a set of kinematic variables, such as momenta and energies, and keeps track of the production history (in terms of *mother-daughters* relationship and production vertex). Each particle is then transported into the set of detectors: the point where the energy is deposited together with the amount of such energy constitutes an *hit*. The hits contain also information about the particle that generated them. At the next step the detector information is taken into account. The hits are '*disintegrated*': the information on the parent track is lost and the spatial position is translated into the corresponding detector readout element (e.g. strips, pads, etc.), thus generating the *digits*. There are two types of digits: the summable digits, where zero-thresholds are used and the results can be summed when different events are superimposed (event merging), and the digits, where real thresholds are used and the result is similar to what one would get in a real data taking. The digits are eventually converted in raw data, which are stored in binary format as a payload. The reconstruction chain can then start, allowing the creation of track candidates. The final output is an *Event Summary Data* (**ESD**), a root file containing all the output of the reconstruction relevant for physics studies.
Metadata information of reconstructed events in the ESD file are stored in the Tag database of AliRoot: this is important in the analysis since it allows to select only those events of interest for the specific analysis considered, with a fast query to the database. The selection, performed through a train of analysis tasks, results in the creation of *Analysis Object Data* (**AOD**) files, which contains all the information needed for a specific analysis and can be more easily handled by end users.

2.3.12 The AliEn Framework

With a data acquisition rate of 1.25 GB/s in the heavy ion progamme, about 5 PB/year of data stored on tape and an amount of CPU power equivalent to about 25000 PCs per each year, the ALICE experiment represents a challenge for data storage and processing. The picture is further complicated by the fact that, in an international collaboration, the computing resources and competences are naturally distributed, thus making a centralized solution almost impossible. The issue was addressed by the High Energy Physics (HEP) community to the Grid computing, that is the combination of computer resources from multiple administrative

[1]a tree is a widely-used dynamic recursive complex data structure that emulates a hierarchical tree structure with a set of linked nodes

domains for a common goal. Grids are usually used for solving scientific, technical or business problems that require a great number of computer processing cycles for processing of large amounts of data. One of the main strategies of Grid computing is to use 'middleware' to divide and apportion pieces of a program among several computers, sometimes up to many thousands. What distinguishes Grid computing from conventional high performance computing systems such as cluster computing is that Grids tend to be more loosely coupled, heterogeneous, and geographically dispersed: the Grid paradigm implies the unification of resources of distributed computing centers, in particular computing power and storage, to provide them to users all over the world. It allows computing centers to offer their resources to a wider community. This allows resources in large collaborations to be shared. ALICE has developed a Grid middleware called **AliEn** [123] since 2001. An ALICE user employs AliEn to connect to the ALICE Grid which is composed of a combination of general services that are provided by many Grid middleware solutions and ALICE specific services provided by AliEn. Part of the ALICE Grid is a global file catalog that is a directory of files in storage elements distributed over the Globe, automatic matching of jobs for execution to a suitable location in one of the connected sites and a shell-like user interface. Currently the ALICE Grid consists of about 80 sites located in 21 countries. The system has been tested extensively with up to 10 000 jobs running concurrently over several weeks. A part of the simulated data used in this thesis has been produced at these sites.

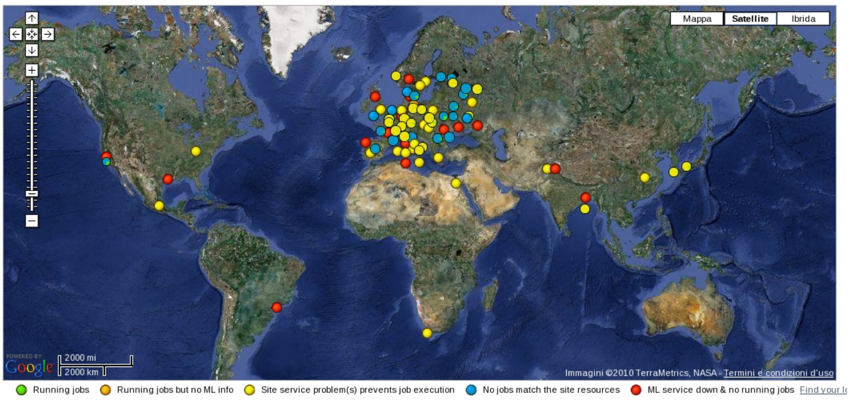

Figure 2.18: A global view of ALIEN site.

Detector	Acceptance (η,ϕ)	Position (m)	Dimension (m^2)	Channels
ITS				
SPD	$\pm$2, $\pm$1.4	0.039, 0.076	0.21	9.8 $\times 10^6$
SDD	$\pm$0.9, $\pm$0.9	0.150, 0.239	1.31	1.33 $\times 10^3$
SSD	$\pm$0.97, $\pm$0.97	0.380, 0.430	5.0	2.6 $\times 10^6$
TPC	$\pm$0.9 at r = 2.8 m $\pm$1.5 at r = 1.4 m	0.848, 2.466	r.o. 32.5 m^2 Vol. 90 m^3	557568
TRD	$\pm$0.84	2.90, 3.68	716	1.2 $\times 10^6$
TOF	$\pm$0.9	3.78	141	157248
HMPID	$\pm$0.6, 1.2° $< \phi <$ 58.8°	5.0	11	17920
PHOS	$\pm$0.12, 220° $< \phi <$320°	4.6	8.6	17920
EMCal	$\pm$0.7, 80° $< \phi <$187°	4.36	44	12672
ACORDE	$\pm$1.3, -60° $< \phi <$60°	8.5	43	120
MUON				
Trk S 1	-2.5$< \eta <$-4.0	-5.36	4.7	1.08 $\times 10^6$
Trk S 2		-6.86	7.9	
Trk S 3		-9.83	14.4	
Trk S 4		12.92	26.5	
Trk S 5		14.22	41.8	
Trg S 1	-2.5$< \eta <$-4.0	16.12	64.6	21 $\times 10^3$
Trg S 2		17.12	73.1	

Table 2.2: Summary table of the principal detector features in ALICE. Acceptance in η is estimated from the nominal interaction point and is in total azimuth, where is not specified. The position is the distance from the interaction point to detectors surface: it correspond to inner and outer radius for central barrel detectors and to z-position for the others. The dimensions is the effective sensitive area for each subsystem and the channels are the number of readout indipendent channels for each detector. (Trk S = Tracking Station; Trg S = Trigger Station)

Chapter 3

The Time Of Flight Detector

The Time-Of-Flight detector (TOF) has been designed in order to cover the central pseudo-rapidity region ($|\eta| <0.9$). This apparatus is, in the ALICE framework, the one dedicated to particle identification (PID), through time-of-flight measurement, in the intermediate and relatively high momentum region, below about 2.5 GeV/c for pions and kaons, up to 4 GeV/c for protons, with a π/K and K/p separation power better than 3σ [124]. Since most of charged particle will be emitted in this range, performances of this detector is a matter of crucial importance for the experiment. Charged particles measurements and identification in this range of momenta will provide observables that will be used in order to investigate the nature and dynamic evolution of the system that will be produced in the heavy ions collision at LHC. In addition, at the inclusive level, identified kaons will allow invariant mass studies, in particular the detection of open heavy-flavoured states and vector-meson resonances such as the ϕ meson ([126, 127, 128, 129]). In order to perform the identification, it exploit the informations on the tracks, which are extracted by TPC and ITS, comparing it with an extremely accurate measurement for the particle time of flight.

3.1 Particle IDentification with TOF detector

The identification of charged hadrons in ALICE is done combining the PID information provided by several detectors. The TOF detector is designed to identify charged particle at intermediate momenta using the time-of-flight technique measurement in the central rapidity region. Monte Carlo simulations of the apparatus, the commissioning with cosmic rays and first *p-p* collisions data have confirmed

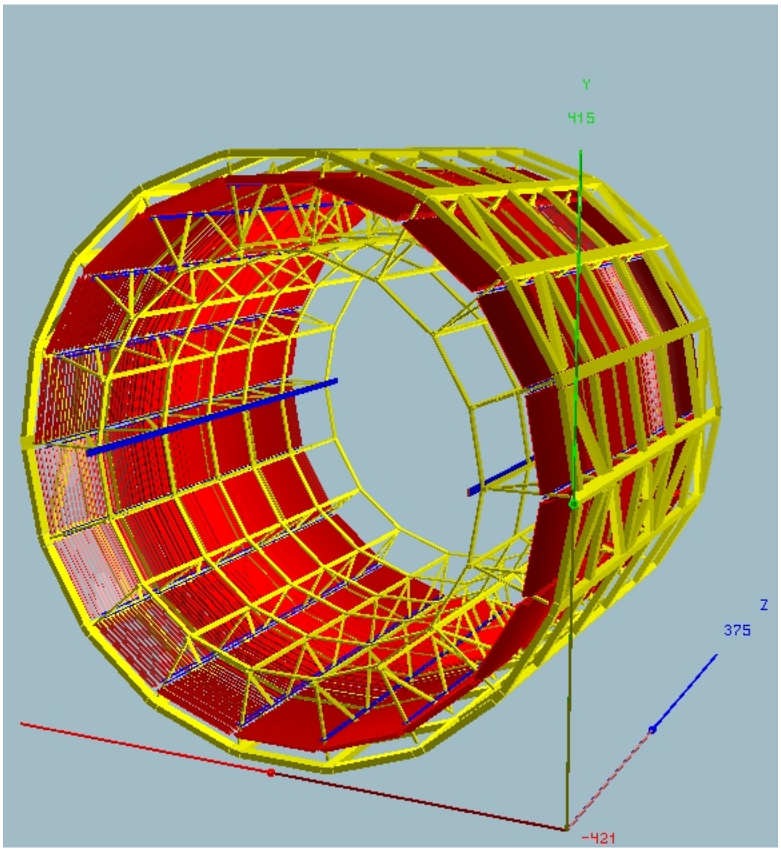

Figure 3.1: The Time-Of-Flight detector

the good performance foreseen for such device.
The identity of a particle can be only determined from its charge and mass. The particle charge can be directly measured, while particle mass cannot, so the simultaneous and independent measure of two different kinematic variables is needed, and one of them must depend on the particle mass. Usually, in high-energy physics experiments, particles are bent in a magnetic field to measure their momenta. Particle velocity measurement is often used together with momentum measurement for particle identification. Many techniques deal with particle velocity measurement, but the choice of the most suitable method is strongly related to the required momentum ranges. Cherenkov detectors, for example, measure θ angle of the

emitted light from a relativistic particle that cross a medium through the formula:

$$cos\theta = \frac{1}{\beta n}. \tag{3.1}$$

This relations connect the light emission angle (θ), the speed through the relativistic term $\beta = v/c$ and the refraction angle of the medium n. But, the emission take place only for $\beta \geq 1/n$, making impossible identification for low momenta particle. At LHC the expectation is for 97 % of particle with a momentum lower tha 2 Gev/c: it's necessary to use another method to determine the speed of the particles produced in the interaction.
The time-of-flight technique turns out to be well suited for particle identification in the mid-momentum region. This technique is based on the measurement of the particle time-of-flight t^{TOF} over a known trajectory length L. This leads to the measurement of the particle velocity $v = L/t$. Time-of-flight measurements for particle identification require that the momentum p of the particle is also measured. The particle mass m is calculated using:

$$m = p\sqrt{(\frac{t^{TOF}}{L})^2 - 1} \tag{3.2}$$

It is simple to show, starting from this expression, that the mass resolution is:

$$\frac{dm}{m} = \frac{dp}{p} + \gamma^2(\frac{dt^{TOF}}{t^{TOF}} + \frac{dL}{L}) \tag{3.3}$$

where γ is the particle Lorentz factor :

$$\gamma = \sqrt{1 + \frac{p^2}{m^2c^2}} \tag{3.4}$$

Equation 3.3 and 3.4 show that particle identification using TOF measurements becomes worse as the square of the particle momentum: to achieve the same mass resolution at twice the momentum requires four-fold improvement in time resolution. If it should be possible to know the track lenght with a resolution of 0.1% and momentum with 1%, the accuracy on mass is determined by time-of-flight detector time resolution. With a particle that traverse a lenght L=3m in a time t=10 ns, in order to achieve a time resolution $\Delta t/t \sim 1\%$, it's necessary a detector with a precision of $\sim$ 100 ps.

In Fig.3.2 there is a representation of the TOF PID capabilities, showing, for all the reconstructed tracks matched with a signal on TOF, the correlation between the track momentum and the mass for 200 Montecarlo central *Pb-Pb* collision with a TOF resolution equal to 80 ps. On the right there is the corresponding mass distribution for 0.5<p<4.2 GeV with logarithmic (up) and linear scale (down). The distribution for pions, kaons and protons are indicated with red, blue and green, respectively; the black histogram is the inclusive distribution for all the species.

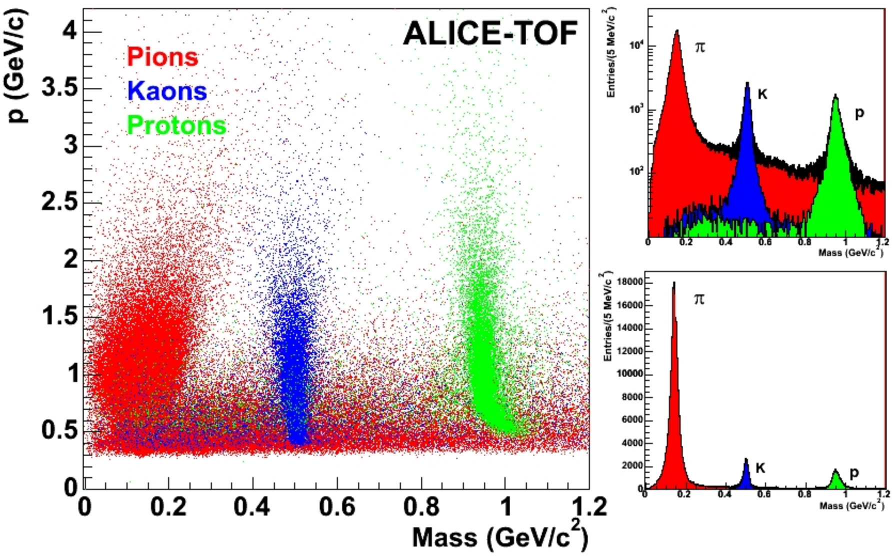

Figure 3.2: Mass separation as a function of momentum as obtained with the Time Of Flight detector in *Pb-Pb* central collisions. [112]

Identification probability of PID with TOF detector

The ALICE particle identification procedure relies on the Bayesian approach. The measured time-of-flight t^{TOF} is chosen as the PID discriminating variable for TOF detector, and the Gaussian

$$g_i(t^{TOF}) \sim \frac{1}{\sigma} exp \frac{-(t^{TOF} - t_i^{exp})^2}{2\sigma^2} \tag{3.5}$$

is used as the TOF *detector response function* for different mass hypotheses m_i (i = e, μ,π, K, p) . Besides the measured time-of-flight, the response function

g_i depends on other two parameters, the expected time-of-flight t^{exp} for the i-th mass hypothesis, and the overall time resolution σ that takes into account both the time resolution of the TOF system σ_{TOF} and the uncertainty σ_{reco} related to the reconstructed momentum and track length:

$$\sigma = \sqrt{\sigma_{TOF}^2 + \sigma_{reco}^2} \tag{3.6}$$

To be noted that $\sigma_{reco} \sim 30$ ps depends on the track momentum and track length [130]. The expected time-of-flight is calculated during track reconstruction summing up at each tracking step the time-of-flight increment:

$$\Delta t_k = \frac{\sqrt{p_k^2 + m_i^2}}{p_k} \Delta l_k \tag{3.7}$$

p_k being the local estimate of the track momentum, and Δl_k the track length increment along the trajectory [130].

On the basis of g_i , the conditional probability $P_i(t^{TOF})$ to be a particle of type i is then assigned to each track, weighting g_i by the *a priori* probability [1] C_i for a track to be an i-particle :

$$P_i(t^{TOF}) = \frac{C_i g_i(t)}{\sum_J C_j g_J(t)} \tag{3.8}$$

with i = e, μ,π, K, p. The probabilities $P_i(t)$ are often called PID weights. The identity of the track is then defined by the highest among the probabilities $P_i(t)$. This approach to particle identification allows to simply combine PID information coming from different detectors in a consistent way. Let us call $r(s_j|i)$ the generic detector response function, where s_j is the PID discriminating variable for the detector j and i is the mass hypothesis. The combined response function is the product of single detectors

$$R(\bar{s}|i) = \prod_j r(s_j|i) \tag{3.9}$$

The combined PID weights are then obtained, in the same way as for the single detector, from the combined response function

$$W(\bar{s}|i) = \frac{C_i R(\bar{s}|i)}{\sum_j C_j R(\bar{s}|j)} \tag{3.10}$$

with i = e, μ,π, K, p.

[1]The *a priori* probabilities C_i have to be determined. In the simplest approach they can be assumed to be equal

PID performance of TOF detector

The performance of the TOF PID procedure can be described in terms of efficiency ε^{PID} and contamination C^{PID} , defined as:

$$\varepsilon^{PID}(i) = \frac{N^t_{id}(i)}{N(i)} \tag{3.11}$$

$$C^{PID}(i) = \frac{N^w_{id}(i)}{N^t_{id}(i) + N^w_{id}(i)} \tag{3.12}$$

$N(i)$ being the number of particles of type i (i = π, K, p) associated with a signal on the TOF system, $N_{id}(i)$ the number of i-particles correctly identified, and $N^w_{id}(i)$ the number of non-i-particles misidentified as particles of type i(the superscript t stands for correctly identified, w for uncorrectly identified, and $t+w$ is the whole identified particle sample).

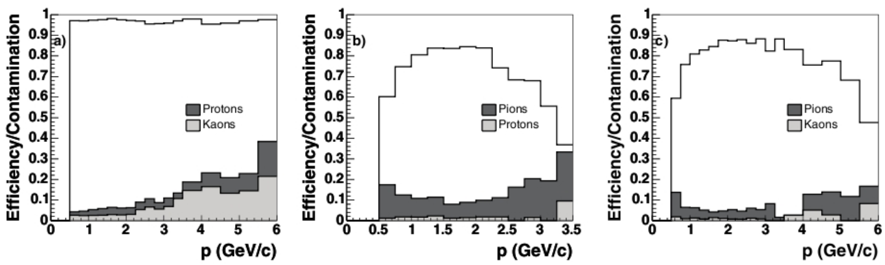

Figure 3.3: Momentum dependence of the efficiency (empty histograms) and contamination (shaded histograms) of the TOF PID procedure in *Pb-Pb* central events, for primary particles of different species (*left*: pions, *central*: kaons, *right*: protons). The dark/light-shaded histograms are aimed at distinguishing the contamination to each particle specie coming from the others. [126]

As can be seen from Fig.3.3, a very high ($>$ 95%) identification efficiency can be obtained for pions, almost constant over the whole momentum range 0.5 $< p <$6 GeV/c, while kaons and protons show a slightly worse and momentum-dependent performance (at most 85%). At low momenta, the particle identification for kaons and protons suffers from track-TOF signal mis-associations (and decays, for kaons), while at high momenta the results are affected by the decrease of the K/π and K/p separation power (pions are less sensitive to these effects, since

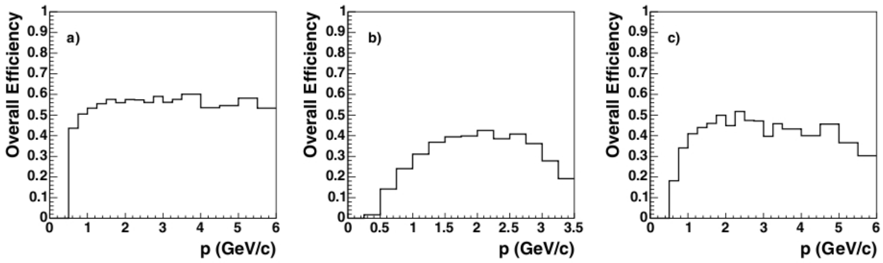

Figure 3.4: Momentum dependence of the overall efficiency of the TOF PID procedure for primary particles of different species generated in the region $|\theta$- 90°$| < 45°$(*left*: pions, *central*: kaons, *right*: protons). [126]

they are the most abundant particle type). On the other hand, the PID contamination varies from a few percents to ∼30% and to ∼ 15% for pions and protons (respectively) in the momentum range $0.5 < p < 6$ GeV/c, while for kaons, it ranges from 20% up to 10% (mostly from pions, as in the case of proton contamination), for momenta $0.5 < p < 3$ GeV/c. Analogously to what happens for efficiency, the main contribution to contamination in the low momentum region comes from track-TOF signal mis-associations, while at high momenta the time-of-flight separation power plays a crucial role.
Fig. 3.4 shows the corresponding overall TOF PID efficiencies with respect to primary tracks generated in the $|\theta - 90°|$ region. Here, the track reconstruction efficiency, the effect of the TOF dead zones, the losses due to particle decays and interactions affect the PID efficiency itself. It should be pointed out that the results presented here, especially for what concerns PID contamination, are strongly influenced by the relative particle concentrations adopted and may vary significantly at LHC. In particular, if the production rates of pions, kaons and protons become comparable at momenta $\geq$ 1.5 GeV/c, as suggested by RHIC results [131], then a substantial improvement in the kaon contamination will be expected.

3.1.1 PID performance of TOF detector with *p-p* collision

As already written, in November 2009 the first p-p collisions at LHC have performed. At the end of March 2010, the LHC come back to operate with *p-p* collisions at $\sqrt{s}$ = 0.9, 2.36 TeV and 7 TeV. With the last collected data , it has been possible to preliminary estimate the TOF detector performance in Particle

IDentification, as shown in Fig. 3.5.

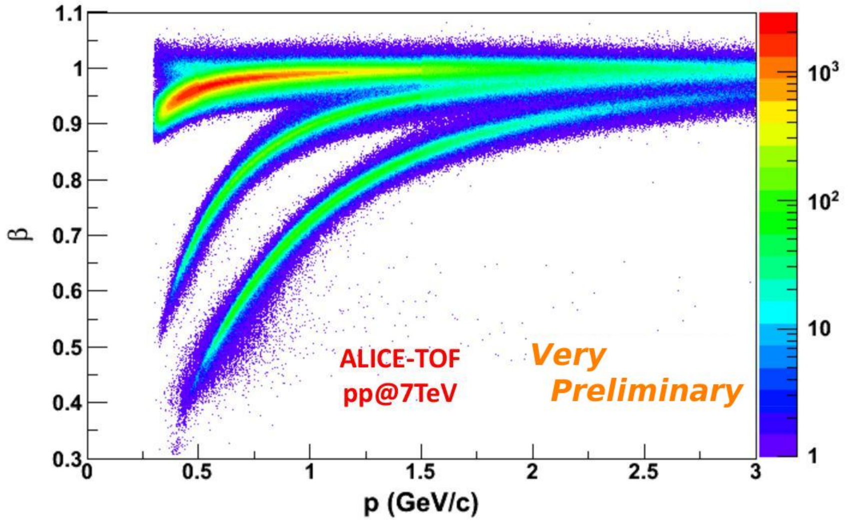

Figure 3.5: β vs momentum as obtained with the Time Of Flight detector in *p-p* collisions at 7 TeV. The analysis has been performed on 3.6×10^6 tracks reaching TOF detector. [132]

From this first evaluation, it's already possible a good discrimination of π, p and K: the TOF shows a very good PID capability.

3.2 Multigap Resistive Plate Chamber

A large-coverage ($\sim$150 m^2 active area) TOF detector has been constructed for the ALICE experiment with $\sim$157000 independent channels adopted to work in an environment with the highest expected charged-particle density (dN_{ch} /dη $\sim$8000). The required performance in terms of detection efficiency and time resolution has been obtained using as the basic detecting element the *Multigap Resistive Plate Chamber* (**MRPC**) strip detector. A solution based on fast scintillators and mesh photomultipliers would have been prohibitively expensive; so the choice was for a gaseous TOF detector.
An intensive R&D programme at CERN, carried out by the group of INFN and University of Bologna and Salerno with the collaboration of Institute for Theo-

retical and Experimental Physics, Moscow, and Kangnung National University, has led to the Multigap Resistive Plate Chamber [125] technology. In Fig. 3.6 a schematic diagram and principle of operation of a multigap RPC compared to a conventional single-gap RPC is shown.

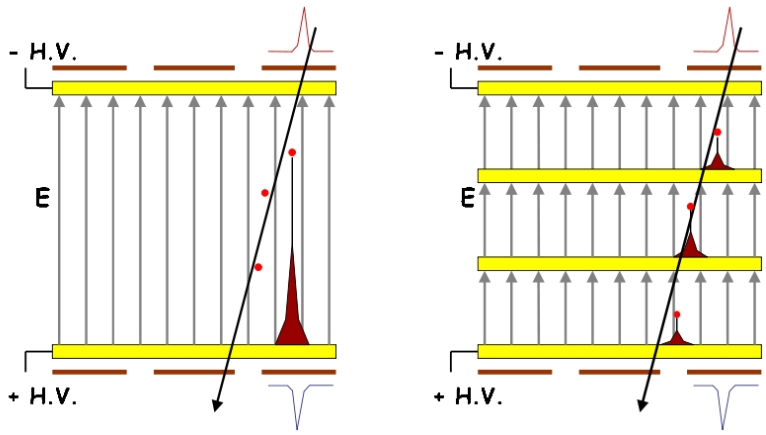

Figure 3.6: Avalanche formation in RPC and MRPC gap when a particle cross their sensitive volume.

A series of gas gaps with a single set of pickup pads reading out all gaps in parallel, combines the advantages of a wide-gap RPC (high efficiency) with the better time resolution performance of small gap chambers. A key issue in the operation of these detectors is the fact that the electric field is high and uniform and therefore the electrons produced by ionization start avalanching immediately; there is no drift time associated. There is also a further advantage of subdividing the gas gap into many small gaps. A through-going particle produces individual and separate clusters of primary ionization; each of these clusters will start an avalanche and the final signal will be the sum of all avalanches. In a single-gap device, these avalanches are not independent and the resulting signal is as if there should be only one large avalanche. On the contrary, for multigap chambers the signal is indeed the sum of independent avalanches, since the avalanches occur in independent subgaps. Moreover, with the single-gap RPC the avalanche mechanism is dominated by fluctuations, while an average of many avalanches is the resultant signal in MRPCs. Other main advantages of the MRPC technology are:

- the chamber operates at atmospheric pressure ;

- the signal induced on the pickup electrodes by the movement of electrons and ions in the avalanche is the sum of the signals from all gaps. There is no late tail in the time response and the charge spectrum has a peak well separated from zero, thus the setting of the threshold is far less critical with respect to exponential-shaped charged spectra;
- the resistive electrodes quench streamers so that they do not initiate a spark breakdown: this allows for high-gain operation;
- the construction technique is rather simple and based on commercially available materials.

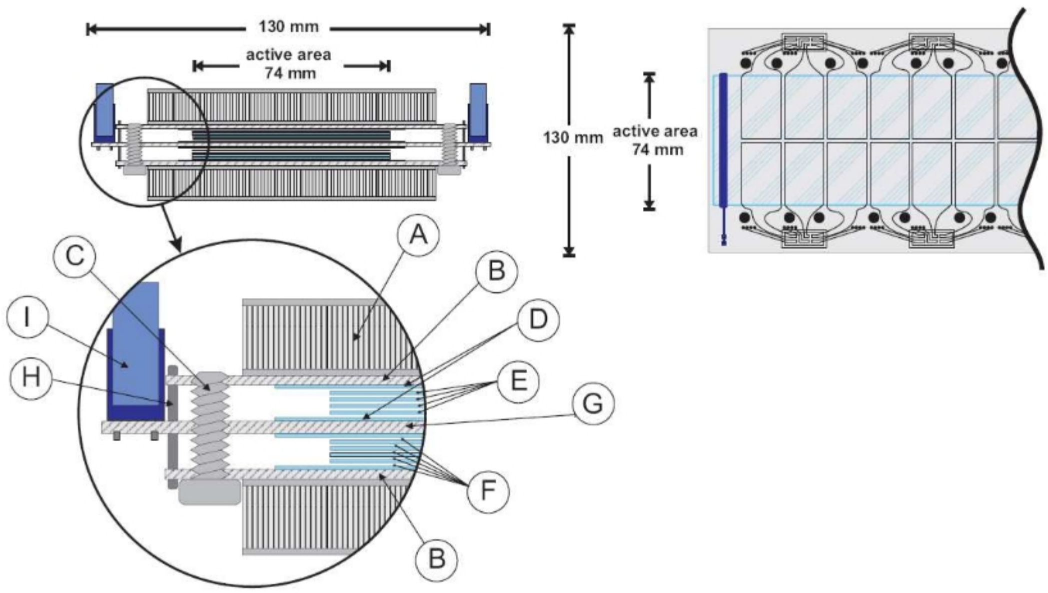

Figure 3.7: Schematic drawing (cross section and top view of the anode PCB) of the ALICE TOF MRPC strip. (A) 10 mm thick honeycomb panel; (B) PCB with cathode pads; (C) Nylon screw to hold fishing line; (D) 550 μm thick external glass plates with resistive coating; (E) 400 μm thick internal glass plates; (F) 250 μm wide gas gaps; (G) PCB with anode pads; (H) metallic pins to bring cathode signals to central PCB; (I) connectors for differential signal from MRPC to front-end electronics.

The Multigap Resistive Plate Chamber design used for the ALICE TOF detector operate with a $C_2H_2F_4$ / C_4H_{10} / SF_6 (90%/5%/5%) gas mixture; it has

demonstrated its excellent performance, with almost 100% efficiency and time resolution below 50 ps.
The basic detecting element used is the double-stack MRPC strip, shown in Fig. 3.7, 3.8 and 3.9.

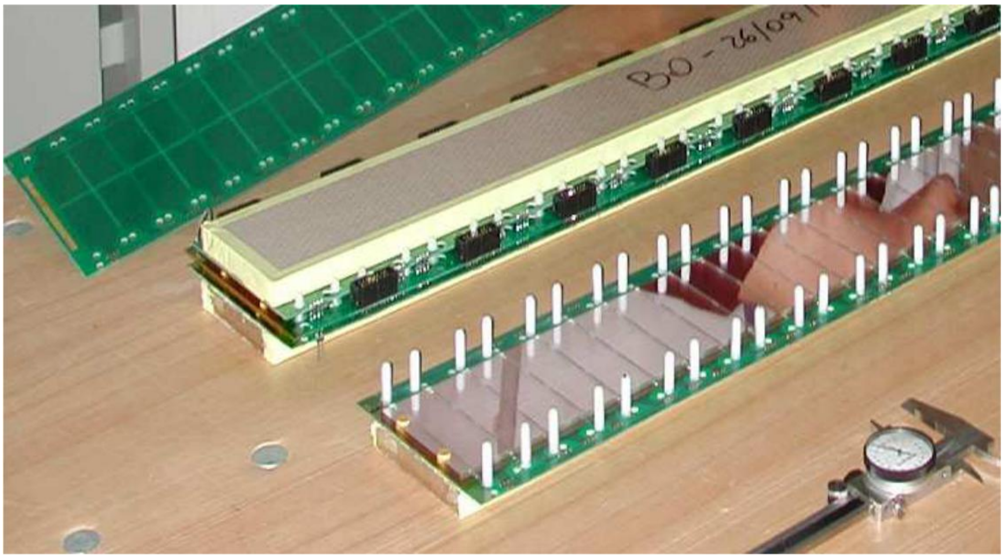

Figure 3.8: A phase of the MRPC TOF assembling. It's possible to see: the white plastic pins that hold the nylon fibersused to define the gap; the black connectors that transmit the differential signals to the front-end electronics; the green PCB.

The strip geometry has been chosen so that a differential signal can be directly derived from the pickup pads to feed the front-end electronics. Moreover, it allows the MRPCs to be oriented to the interaction point (in the $r-z$ plane). This reduces the number of very oblique transversal paths that can create a sharing effect of the signal among adjacent pads, thereby increasing the occupancy and the time resolution. The strip has a 120 $\times$ 7.4 cm^2 active area (122 cm long and 13 cm wide), segmented into two rows of 48 pickup pads of 3.5 $\times$2.5 cm^2 .
The double-stack design consists of two stacks of equally spaced resistive plates, creating 5 gas gaps of 250 μm each. Nylon fibres (fishing line) are used to define the size of the gas gap; these spacer fibres run across the width of the strip at the boundaries between pads (every 2.5 cm), held by plastic pins. The high voltage is applied to the outer surfaces of the stack of resistive plates (external plates). The

internal plates are electrically floating and take the voltage by electrostatic: they are kept at the correct voltage value by the flow of positive ions and electrons in the avalanches [133].
Two external (*cathode*-side) and one internal (*anode*-side) printed circuit boards (PCBs) define the two stacks. The PCBs contain the 96 pickup pads (to collect the avalanche signal) and two small high-voltage pads at the extreme ends (to provide the external plates with high voltage).
The resistive plates are made of glasses; the internal and external plates are 400 μm and 550 μm thick, respectively. The external surface (facing the PCB) of the outer plates is painted with high resistivity acrylic paint and is used to apply the high voltage.
Two honeycomb panels, glued on the external PCBs guarantee the mechanical stiffness. Connecting pins are soldered across the 3 PCB layers in order to bring cathode signals from the external PCBs to the central PCB, where anode signals are collected. Moreover these pins keep the stacks compressed. Two rows of 16 connectors are soldered on the central PCB to transmit the differential signals to the front-end electronics.

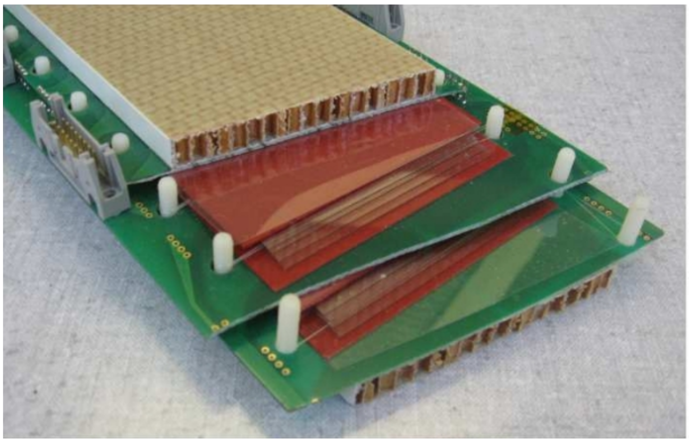

Figure 3.9: TOF MRPC section. The red painted glass and the hoenycomb panels are clearly visible.

Two pulse lines on one cathode PCB run along the length of the strip creating a capacitive coupling to the pickup pads used for monitor and calibration purposes.

3.3 Modules and Supermodules

The Time Of Flight (TOF) detector of ALICE has a modular structure corresponding to 18 sectors in the azimuthal angle ($0^\circ \leq \phi \leq 360^\circ$) and to 5 segments in the longitudinal coordinate along the beam axis z . The whole device is locate inside a cylindrical volume with an internal radius of 370 cm and an external radius of 399 cm. To cope with the structures of the space frame and minimize the dead zones, three different types of modules have been designed to cover the full lenght of the cylinder. They all have the same structure and width ($\sim$ 128 cm) but differ in lenght and in the MRPC strip contents and arrangements. The *central module* is 1.17 m long, the *intermediate* ones are 1.57 m long and the *external* ones are 1.77 m long; the first host 15 strip, the others two 19. The overall TOF barrel is $\sim$ 745 cm. The actual dimensions are defined in such a way that the joining areas of the modules are aligned with the dead regions of the other detectors projected from the interaction point, thus creating a configuration of minimal disturbance for the external detectors.

The TOF strips have been arranged inside the modules following, with respect to the interaction vertex, a particular geometry designed to minimize the transversal path of the incident particles through the MRPC strips and reduce the sharing of the charge, produced by the ionization taking place in the gas volume of the MRPC, among adjacent pads. The MRPC strips are then placed, in each sector, transversely to the beam direction. In particular their angle with respect to the axis of the cylinder is progressively increasing from 0° in the central part ($\theta = 90^\circ$) of the detector to 45° ($\theta = 45^\circ$ and 145°) in the extreme part of the external module.Moreover, to minimize the dead area within the module, adjacent strips are overlapped by about 2 mm.

The granularity of the TOF detector is determined by the requirement to identify, on an *event-by-event* basis, as many charged particles as possible up to the highest expected charged-particle multiplicity density (dN_{ch} /$d\eta$ = 8000). Detailed simulation studies have shown that, with the chosen pad size of 3.5×2.5 cm^2 and the tilted-strip geometry, the occupancy of the detector is $\sim$ 16%, at the highest charged particle density (including secondary particles) with a magnetic field of 0.2 T. Lower values of the particle or higher values of the magnetic field improve the occupancy ($\sim$ 7% for dN_{ch} /$d\eta$ = 4000 and B = 0.2 T; $\sim$13% for dN_{ch} /$d\eta$ =8000 and B = 0.4 T) as expected.

The TOF module is a box that defines and seals the MRPC strip gas volume and supports the external front-end electronics and services (high voltage, gas, pulser).

A 1.5 cm thick aluminium-honeycomb plate gives the mechanical stiffness to the chamber and is connected to a fibreglass 0.3 cm thick, that cover closes the gas volume, by means of sealing O-ring and screws. The inner surface of the fibreglass is covered with an aluminium layer for electromagnetic shielding (Faraday cage). Inside the module two plates are fixed perpendicularly to the honeycomb to support the strips. The MRPC are then attached to those plates at the required angle with plastic screws (see Fig. 3.10).

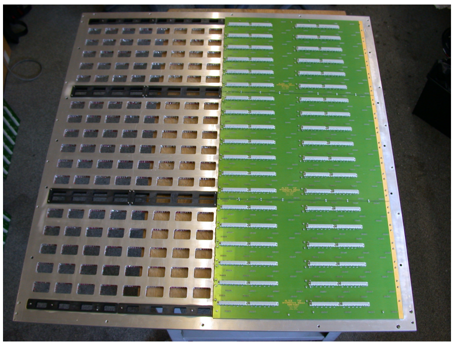

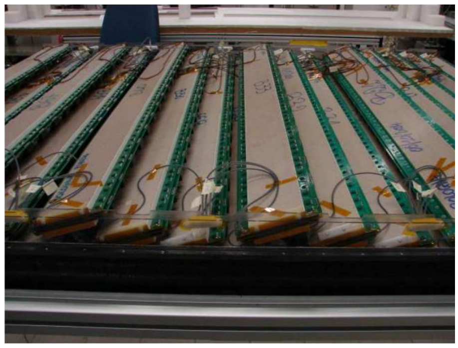

Figure 3.10: Parts of the module and an assembled module with the MRPCs inside.

Holes that can accommodate feed-through for signal cables, high-voltage connectors, gas inlet/outlet and pulser inputs are machined in the honeycomb plate. Large printed circuit boards, covering almost all the honeycomb surface, are glued to the plate: they provides the interface between the gas volume and front-end electronics; in fact, on the external side it houses the connectors where the front-end cards are plugged into, while on the internal side there are the connectors for the flat-cables coming from the MRPCs. In the gas volume the high voltage is distributed to groups of 3-4 MRPCs.

The modules with MRPCs inside has been assembled and put together to form **SuperModules**: five modules in a row (external, intermediate, central, intermediate, external) are aligned among themselves to lay in the same plane without gaps. Long aluminium beams bound them along their length with stainless steel screws, which fix the beams to the module honeycomb panel, on the opposite side of the gas volume. Transverse aluminium beams bound the modules at their joining area in the same way. The transverse beams at both sides of the external modules provide support for the readout crates, which are attached in pairs to both ends of the structure. The aluminium beams arranged in that way form five zones correspond-

Figure 3.11: A TOF supermodule ready to be installed in the ALICE spaceframe.

ing to the so-called *front-end* area of each module. In Fig. 3.11 a view of a TOF SuperModule is shown.

3.4 Electronics

3.4.1 Front End Electronics

For the full exploitation of the excellent time resolution power of the MRPC, front-end electronics with special characteristic has been designed: the FEA card, that hosts the NINO ASIC chips for amplification/discrimination of the MRPC signals, and the FEAC card, which acts as a service card for front-end electronics.

NINO ASIC chip [134], fabricated with 0.25 μm CMOS technology, is an 8-channel amplifier and discriminator chip. It has been specifically developed to match the requirements for the ALICE TOF MRPC-strip detector:

- differential input, to profit from the differential signal from the MRPC;
- fast amplifier, with less than 1 ns peaking time;
- input charge measurement by *Time-Over-Threshold* (**ToT**) for time-slewing correction.

The NINO ASIC encodes the charge of the input signal into the width of the output signal (Time-Over-Threshold). No further readout electronics is needed to measure the charge.
The NINO ASIC is a very low power-consumption (40 mW/channel) chip, a factor 10 less than the commercial discrete amplifier/discriminator solution used for the detector prototypes, and it is very compact (2 mm $\times$ 4 mm), thus reducing the size of the front-end card.

Front-End Analogue (**FEA**) cards host three NINO ASIC chips for a total of 24 channels. A picture of the FEA is shown in Fig. 3.12. These cards are

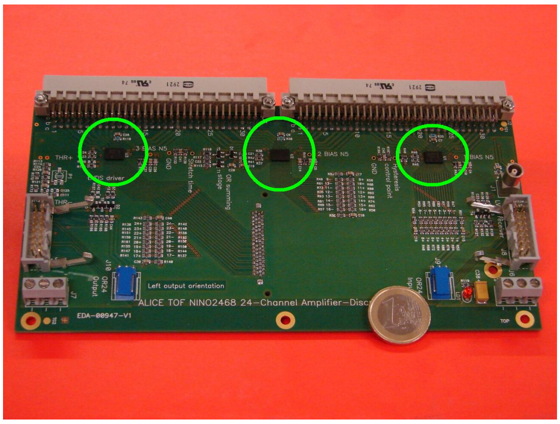

Figure 3.12: FEA with the three NINO ASIC chips.

mounted directly on the TOF module Interface Card printed circuit board.
The card collects the output signals from the NINO chips and connects them to the read-out electronics through 2-5 metres long cables. Moreover, it

forms a 24-channel OR output signal for trigger purposes. The FEA card receives from the FEAC card (see next paragraph) the low voltage (2.5 V) and an external threshold voltage to set the differential threshold of the NINO discriminator circuit.

Front-End Analogue Control (**FEAC**) cards serves 12 FEA cards with the required low voltage and threshold voltage. It is equipped with a temperature sensor to monitor the temperature of the region of the TOF SuperModule which houses the front-end electronics. Moreover, it has been designed to collect the OR signals from the FEA cards.

3.5 Read-out Electronics

A compact data acquisition and power supply system housed in a water cooled special crate has been designed for the read-out of the TOF detector of the Alice experiment. The Crate called Alice-TOF-box contains: 12 TDC Readout Module (TRM) a local Trigger Module (LTM), a Clock Distribution Module (CPDM) and a Data Read-out Module (DRM board) with two optical links and Ethernet. The whole system is used close to the TOF detector and work under moderate radiation and intense magnetic field (1.2 Gy/10 years TID, 5 KGauss). The TDC boards house TDC chips developed by CERN/ECP-MIC Division (HPTDC).

High-Performance Time-to-Digital Converter **(HPTDC)**. A relevant feature of the HPTDC is the signal leading and trailing-edge detection capability. This allows Time-Over-Threshold (TOT) measurements of the MRPC analog signal for time-slewing correction by measuring the width of the digital signal from the NINO (3.4.1). On the other hand, the minimum time between two consecutive time measurements is a critical parameter of the HPTDC: the FEA cards provide the TOT signal with a minimum width of 10 ns.

TDC Readout Module **(TRM)** is the basic block of the ALICE TOF readout system which has a total of 684 TRM boards. Each TRM hosts 30 HPTDC chips organized in two separate parallel readout chains, for a total of 240 TDC channels. The interface is implemented by a Field Programmable Gate Array (FPGA) which also acts as Readout Controller, Event Manager and online Data Processor.

Data Readout Module **(DRM)** acts as the main interface between the central ALICE data acquisition/trigger system and TOF electronics. The main task of the DRM is to read TRM and LTM data and arrange them following the data format common to all ALICE detectors and send them through an optical link (*Detector Data Link*, *DDL*).

Clock and Pulser Distribution Module **(CPDM)** distribute the LHC clock to TOF electronics and generate the pulser signal for calibration and monitoring purposes. The clock distribution guarantees the time synchronization among all TOF electronics and high-performance in time resolution, adding a negligible (17 ps) contribution to the global time resolution.

In Fig. 3.13 a view of the cabling phase of a TOF SuperModule: some elements are shown.

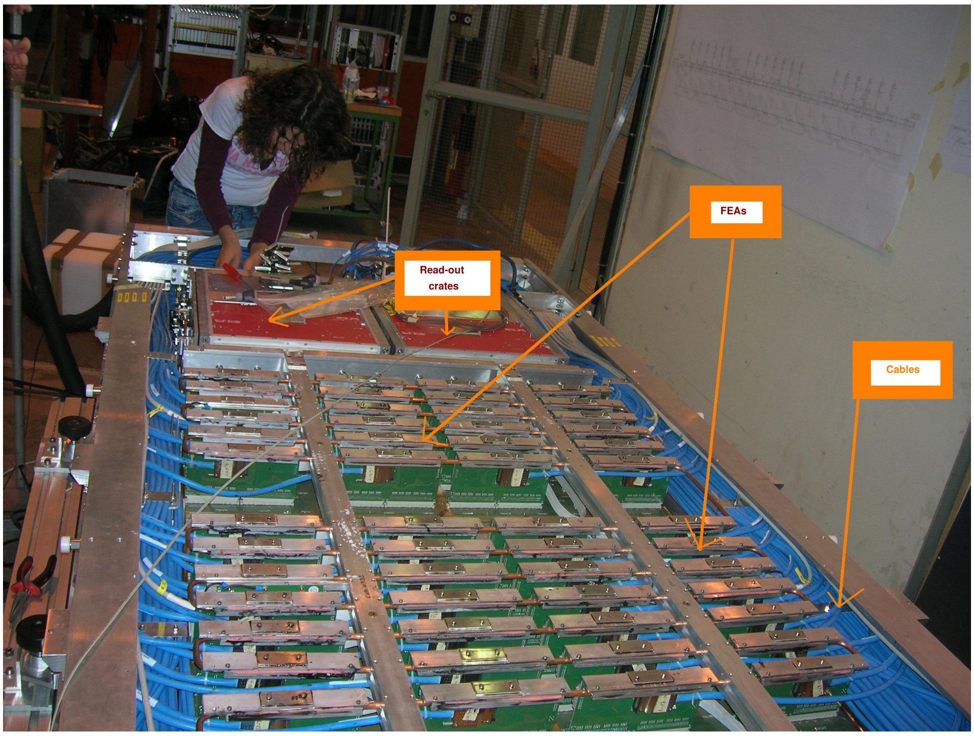

Figure 3.13: View of the cabling phase of a TOF SuperModule.

3.5.1 Tests on the FEACs

The tests of all ($\sim$ 600) FEAC cards used in the TOF detector of ALICE experiment has been performed in University of Salerno Laboratories. In Fig. 3.14 a picture of FEAC and its scheme is shown. FEACs have an important task in

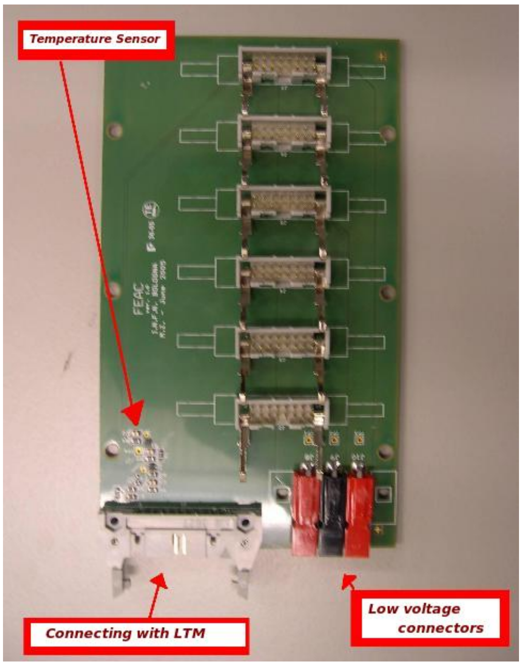

Figure 3.14: Front End ASIC Controller

the SM set-up; they provide the voltage to power on the FEAs and allow to comunicate with them, in order to set the threshold voltages on the discriminator and collect the OR signal from the channels of the daisy-chained FEAs: this is an important signal for the trigger of the experiment. Besides, they can monitor the temperature of different areas of the detector, by a temperature sensor inserted in the circuit. The tests performed on the FEACs are: circuit lines, transmission of the LVDS (Low Voltage Differential Signal) and temperature and calibration V(T,LV).
Circuit lines test has been useful to check open and short circuits in the circuit lines of FEAC, in order to ensure a good power supply working (test on ground and LV lines) and the right working of OR signals transmission line and thresh-

olds setting lines.
LVDS test has been carried out sending to FEAC a LVDS signal generated with a FPGA (Field Programmable Gate Array). The output is read with an oscilloscope

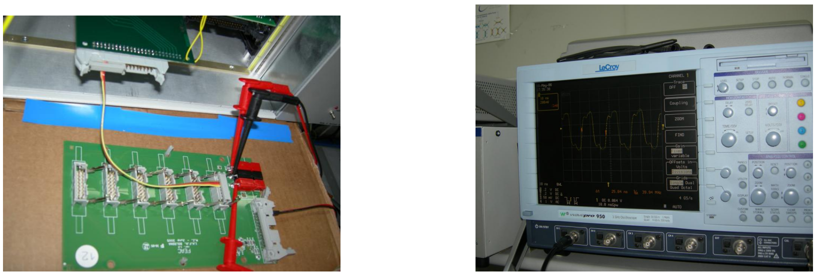

Figure 3.15: LVDS coming out from a FPGA and read with an oscilloscope

(see Fig. 3.15) in order to check the absence of distortions, reductions of the amplitude and crosstalk along the circuit lines.
Temperature tests have been performed in order to verify the FEAC low voltage analog temperature sensor, that works in a range of about fifty Celsius degrees. The test has been carried out reading the temperature sensor voltage, when the FEAC has been put at three different values of temperatures: $\sim 5^\circ$, $\sim 25^\circ$ and $\sim 35^\circ$ C. With the achieved data it is possible to check the right working of cards at dif-

Figure 3.16: Set-up to test the FEACs at different temperature values

ferent temperature values and to get a calibration curve, as showed in Fig. 3.17.

This test is *very* important to have a good temperature monitoring system inside

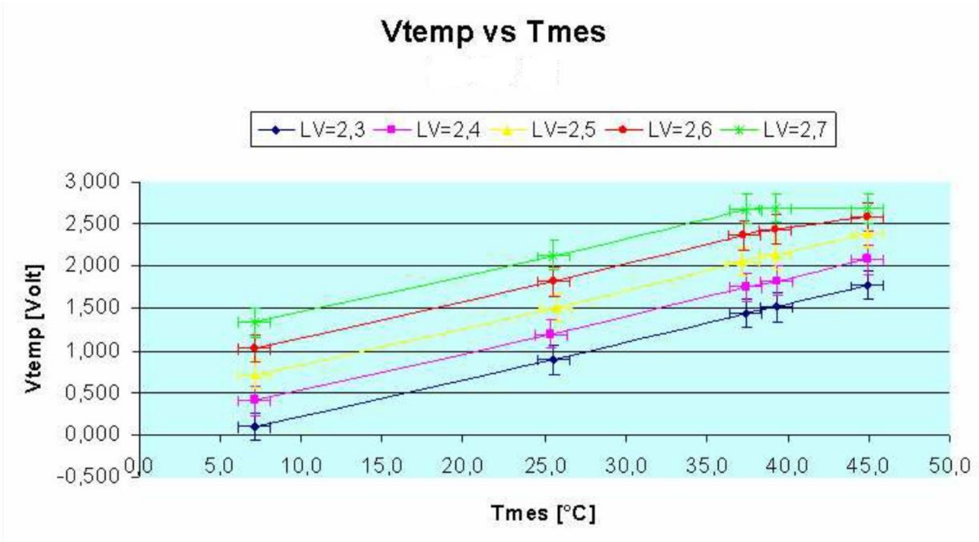

Figure 3.17: FEAC calibration curve.

the TOF supermodules, whose electronic cards will work hard for many years.

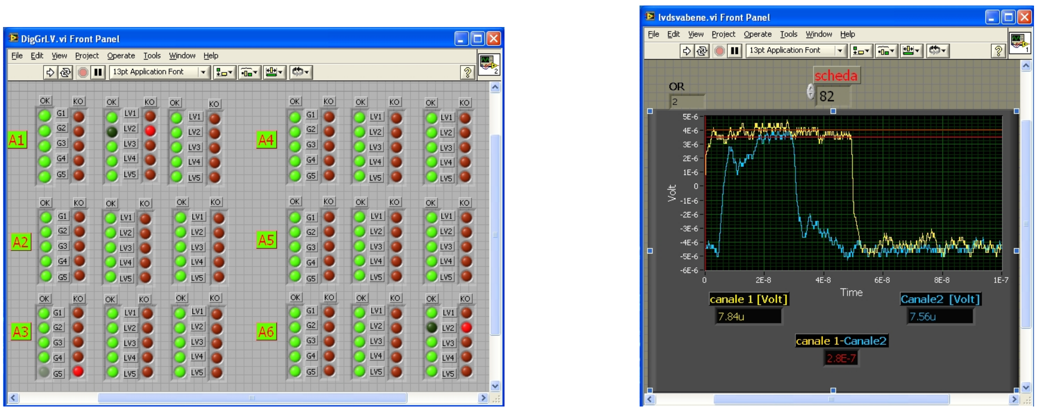

Figure 3.18: Labview application for circuit lines and LVDS transmission tests.

After a preliminary period of tests, three Labview applications have been made in

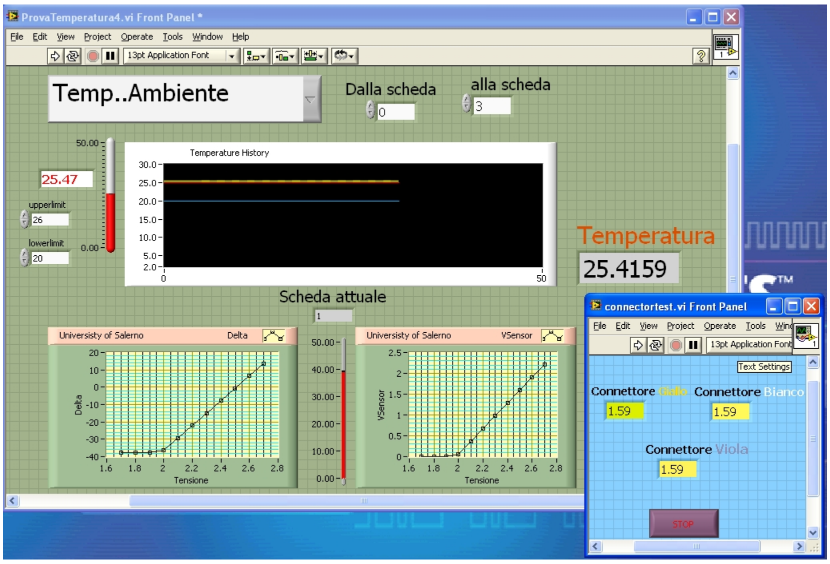

Figure 3.19: Labview application for temperature tests.

order to make the tests easier and faster. In Fig. 3.18 and 3.19 the applications for circuit lines, the LVDS and the temperature are respectively shown.

3.6 Analysis of the first cosmic data

The first global data-taking of ALICE with cosmic rays has been performed during December 2007. Several TOF SuperModules were already installed in ALICE at that time, but only two half-sectors were available with all the needed services to correctly collect data: Sector-00 and Sector-08.
The TOF geometrical configuration which characterized this commissioning phase, shown in a schematic drawing in Fig. 3.20, was not optimal with respect to the used trigger configuration: the ACORDE single-muon trigger. The two sectors, 00 and 08, according to the ALICE sector numbering as indicated in Fig. 3.20, are located in such a way that only almost horizontal particles could cross both of them. Unfortunately, these events were not included in the ACORDE acceptance and were not triggered. Nonetheless the sectors, considered as independent detectors, were sufficiently matched by the trigger acceptance to foresee that at least a few particles triggered by ACORDE could hit them.

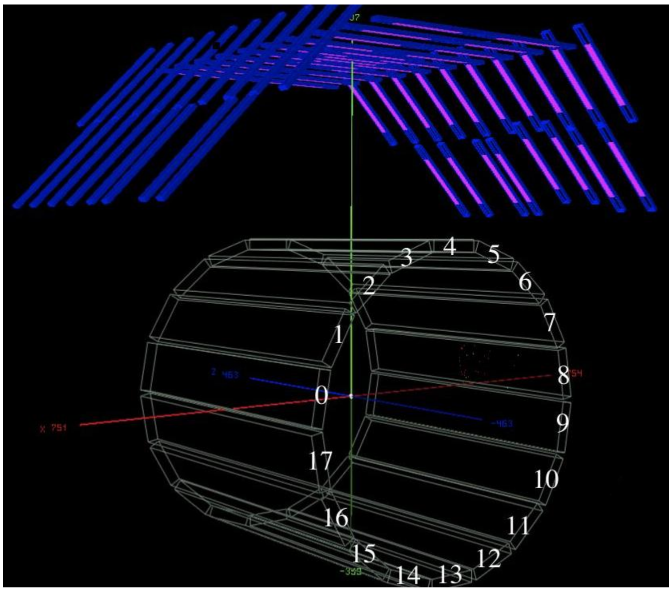

Figure 3.20: Visualization of the first recorded data with TOF detector (white) in December 2007 Cosmic runs. The active sectors were 0 and 8. In blue and pink the representation of the ACORDE detector.

Despite the non optimal geometrical configuration with respect to the ACORDE acceptance, the TOF has detected cosmic rays triggered by ACORDE. Moreover, a few particles which traversed one of the TOF sectors producing easily recognizable tracks have been reconstructed.
A simulation of the trajectory of a muon, crossing the active areas of the operating TOF sectors during the first and second cosmic runs, has been performed. The simulation showed that, with such trigger configuration, a single muon, crossing few adjacent TOF MRPC strips belonging to the same sector, could be revealed (Fig. 3.21).

As a matter of fact, during these two cosmic runs, several events of this kind have been registered: few particles had the correct angle to traverse several MRPCs of the same sector and the ultimate evidence that the TOF detector has seen cosmic rays triggered by the ACORDE single-muon trigger was the reconstruction of such tracks. An example is shown in Fig. 3.6. The particle has passed across the sector width, traversing several MRPC strips. All the MRPCs which have been hit by the particle have released a signal, therefore the detector efficiency must be

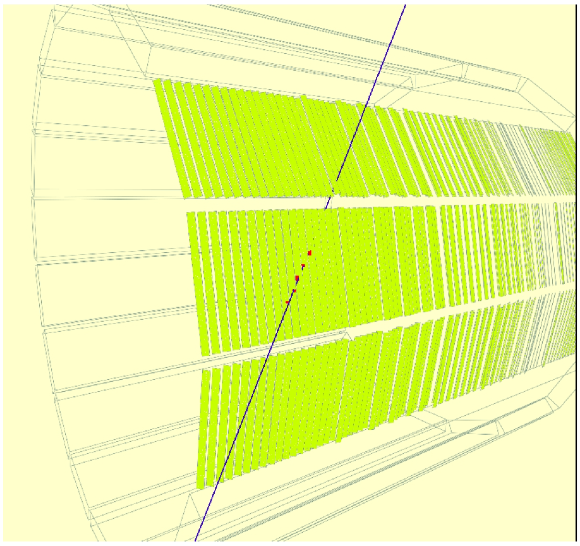

Figure 3.21: Visualization of the trajectory of a simulated muon crossing through the TOF sensitive volume

high. Using these first data a preliminary study of TOF time resolution has been performed: it will be shown in the next paragraph.

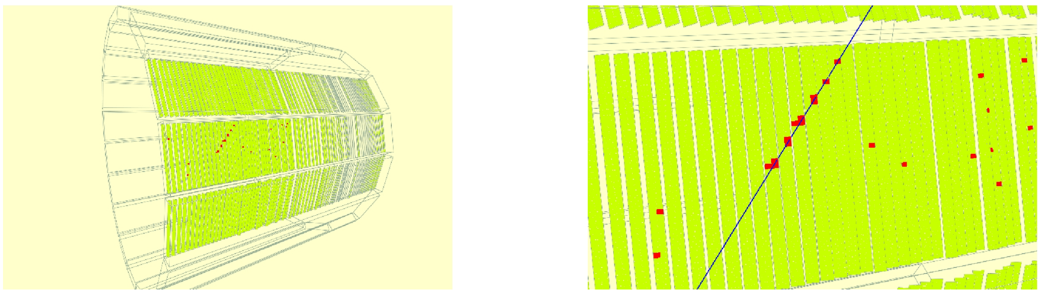

Figure 3.22: Visualization of the hit TOF pads by a cosmic muon. The line is the fit of their positions

3.6.1 Time resolution: a first approach

In the first step of the analysis a set of pads hit by a single muon has been taken into account and the deviation of the time measured on each pad with respect to the average measured time has been calculated. These deviations have been plotted and fitted with a Gaussian function (Fig. 3.23).

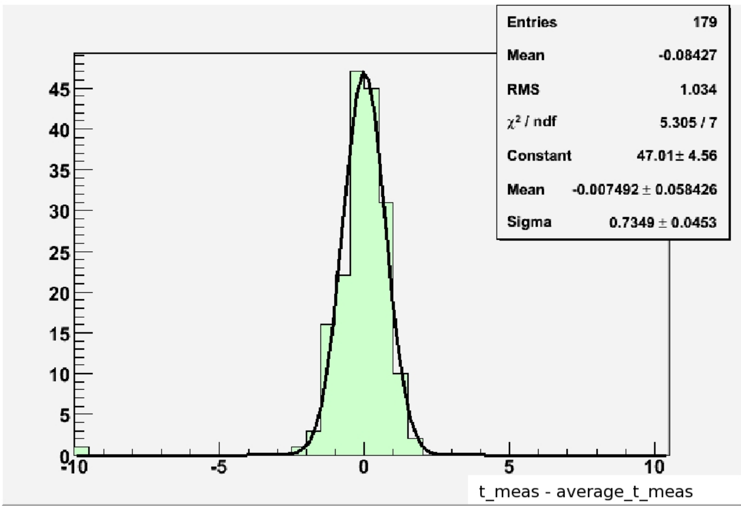

Figure 3.23: Distribution of the difference between measured time on each pad with respect to the average time of the set of pads hit by a single muon. The black line is gaussian fit.

The first estimate of time resolution with this method is 730±50 ps.
In order to improve this evaluation, for every set of hit pad (corresponding to a cosmic muon), the measured time (t_{meas}) on each pad has been plotted versus the strip number; then a linear fit has been performed with the function (Fig. 3.24, *left*).

$$y = a + b * x$$

So, the expected time for each strip has been calculated using the estimated parameter *a* and *b* from the linear fit:

$$t_{exp} = a + b * (strip\ number) \quad .$$

Furthermore, the t_{exp} - t_{meas} deviation(Fig. 3.24, *right*) has been calculated for each point of the graph and the distribution of these deviations (for all cosmic revealed) has been plotted and fitted with a Gaussian function (Fig. 3.25). The result for the

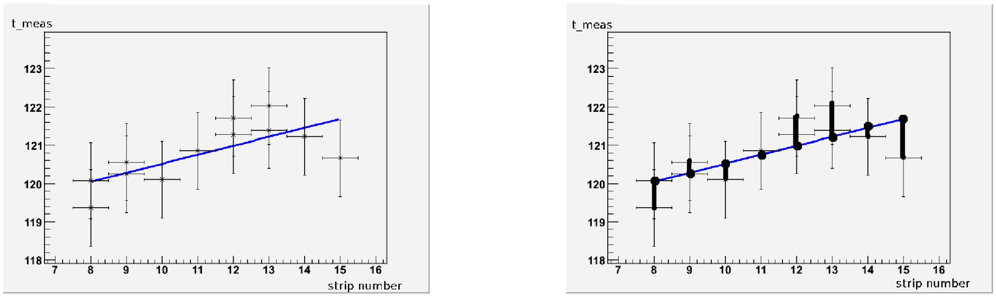

Figure 3.24: Measured time versus strip number method

TOF time resolution with this method is 530±30 ps.

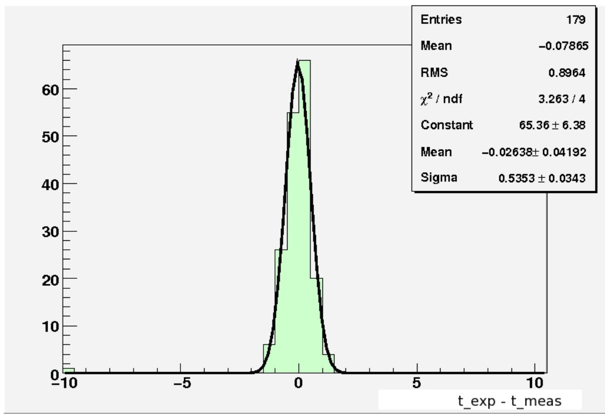

Figure 3.25: Deviation t_{exp} - t_{meas} distribution obtained with measured time versus strip method. The black line is gaussian fit.

In the following step of the analysis, for every set of hit pad (a cosmic muon), the measured time on each pad *versus* the three Cartesian coordinates of the pad, separately, has been plotted and a linear fit has been performed with the function

$$y = a + b * k$$

where k was in turn the X, the Y and the Z coordinate.
So, the expected time for each coordinate has been calculated in this way:

$$t_{expX} = a_X + b_X * X$$
$$t_{expY} = a_Y + b_Y * Y$$
$$t_{expZ} = a_Z + b_Z * Z$$

Then the mean (t_{exp}) of the three values t_{expX}, t_{expY}, t_{expZ} has been calculated and the deviation t_{exp} - t_{meas} has been extracted for each point of the graph. Moreover, the distribution of these deviations (for all cosmic muons revealed) has been plotted and fitted with a Gaussian function (Fig. 3.26). The result for the TOF resolution with this method is 530±30 ps .

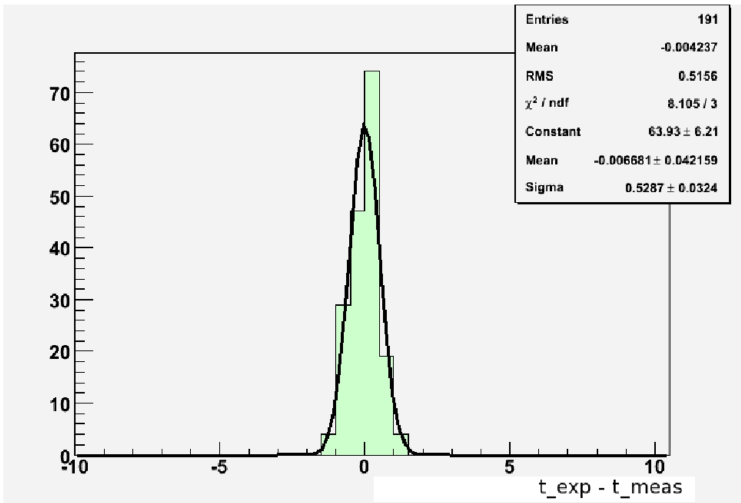

Figure 3.26: Deviation t_{exp} - t_{meas} distribution obtained with measured time versus spatial coordinates method. The black line is gaussian fit.

We can conclude that there isn't any improvement using spatial coordinates instead of strip number to estimate the TOF time resolution.

TOF clustering

As already mentioned, the TOF system consists of long MRPC strips with an active area subdivided into two rows of 48 pads, individually read-out. A particle crossing an MRPC can produce hits on more than a single pad. In fact, the charge produced in the ionization occurring in the gas gaps can release a footprint on several neighboring pads (up to four) sharing in this way the total charge on a *cluster* of pads. This peculiarity has been exploited to produce an algorithm of weighted mean both of spatial position of hit pads and registered times by each hit pad. The weight used is the Time over Threshold measure, i.e. the time interval in which the signal overcomes the threshold (which is strictly related to the measurement of the signal amplitude). With this method, it is possible to obtain, for each strip, a unique value of time and a unique value for the spatial coordinates of the cluster. For every set of hit pads (a cosmic muon), the weighted mean time on each pad has been plotted versus the three Cartesian coordinates, separately, and a linear fit has been performed, as above, with the function

$$y = a + b * k$$

where k was in turn the X, the Y and the Y coordinate of the cluster.
the expected time for each coordinate was calculated in this way:

$$t_{expX} = a_X + b_X * X$$
$$t_{expY} = a_Y + b_Y * Y$$
$$t_{expZ} = a_Z + b_Z * Z$$

Then the mean (t_{exp}) of the three values t_{expX}, t_{expY}, t_{expZ} has been evaluated and the t_{exp} - t_{meas} deviation has been calculated for each point of the graph, i.e. for each cluster. The distribution of these deviations (for all cosmic revealed) has been plotted and fitted with a Gaussian function (Fig. 3.27). The TOF time resolution obtained with this method is significantly improved to a value of 380±40 ps.

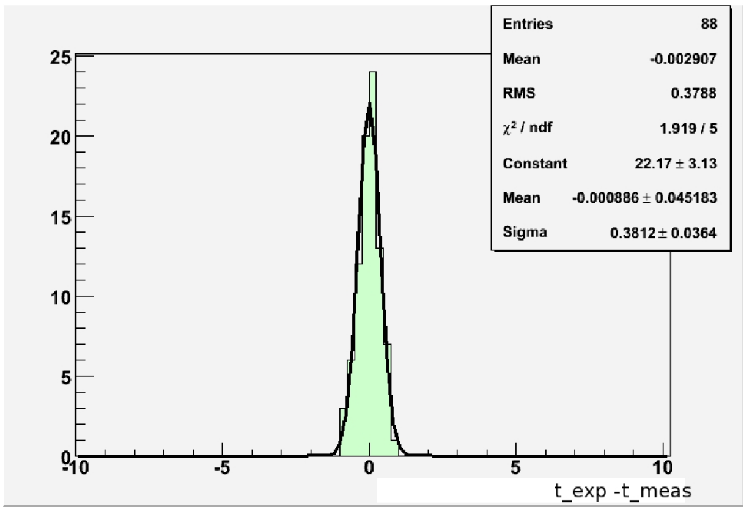

Figure 3.27: Deviation t_{exp} - t_{meas} distribution obtained with cluster method. The black line is gaussian fit.

It's possible to conclude that even neglecting some signal trasmission delay corrections, track momentum, TOF strip alignment and time slewing corrections the obtained very first result for the TOF detector time resolution is 380±40 ps.

3.6.2 TOF trigger

The ALICE TOF MRPC detector is a fast-response device, well suited for triggering purposes. The TOF trigger system, whose fundamental element is the LTM described in section 3.5, contributes to the first levels trigger decision of the ALICE Central Trigger Processor. During the February-March 2008 commissioning period, 8 TOF SuperModules were ready to taking data and could participate in the ALICE global data-taking. In particular, Sector-00, Sector-01, Sector-07, Sector-08, Sector-09, Sector-10, Sector-16 and Sector-17 where used to setup a coincidence in order to provide a muon trigger based on the TOF detector. The TOF cosmic-muon trigger described in this section has been widely used during ALICE commissioning with cosmic rays. It is often referred to as the TOF *back-*

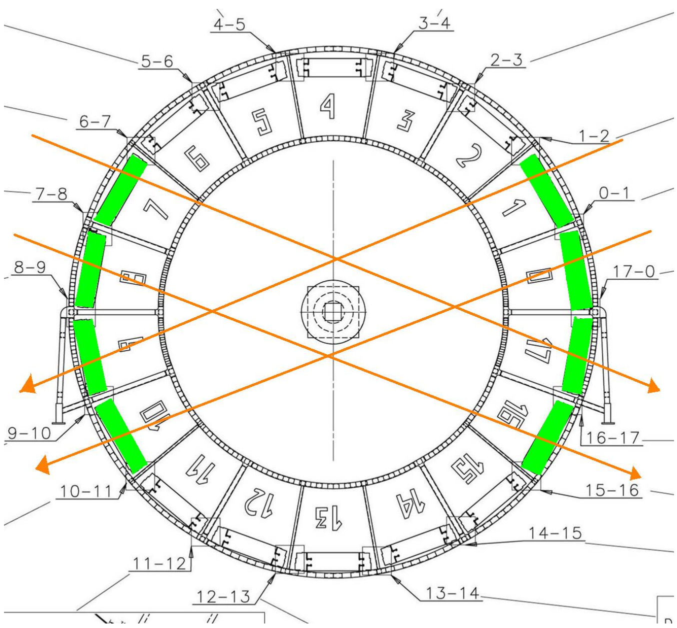

Figure 3.28: Schematic drawing of the TOF muon trigger configuration during February-March 2008 data-taking with cosmic rays.

to-back muon trigger, because of the selection criteria used. The *back-to-back* trigger has been set up to select cosmic muons traversing the ALICE central detectors following a diagonal trajectory.
The following sector coincidences contributed to the trigger, as shown in Fig.3.28:

Sector-00 and Sector-10;
Sector-01 and Sector-09;
Sector-07 and Sector-17;
Sector-08 and Sector-16.

The goal of this first analysis was to evaluate the correct functioning of both the trigger logic and the read-out system. The first step has been to plot the measured time for each crate. In Fig. 3.30 are showed the distribution for each crate included in the TOF setup: it's really clear the peack due to trigger signal.

A rough event selection on the data was performed using only the information coming from the TOF detector. The selected events must satisfy only one of the defined trigger conditions, Sector-00 and Sector-10, with the further constraint that the event must contain one to four hits per sector. This ensures that the selected events should contain the hit which have generated the trigger coincidence and allow to take also into account multiple signal related to the same muon. Per each couple of hits (one per sector) the time-of-flight between the two trigger sectors has been computed:

$$t_{TOF} = t_{SM10} - t_{SM0} \tag{3.13}$$

where t_{SM0} and t_{SM10} are the time measured of the hit on SM0 and SM10, respectively. Clearly, the choice of the order for the difference has been made in accordance with the physical content of the data: muon coming from the atmosphere cross Sector-00 before Sector-10. The time-of-flight depends on the muon trajectory length L, that is the distance between the TOF pads which have given the signal. Another quantity has been introduced to take into account the different trajectory lengths and put all the collected muon events on the same ground. This takes into account the expected time-of-flight, assuming that all selected muons travel at the speed-of-light

$$\Delta_{TOF} = t_{TOF} - \frac{L}{c} \tag{3.14}$$

where L is the distance between the TOF pads which have given the signal and c is the speed of light. In Fig. 3.30 the distribution of the measured time-of-flight with respect to the expected value L/c obtained from a rough analysis on TOF triggered data is presented. Cosmic muons crossing two different sectors have been triggered by the TOF detector and are represented by the clear peak at zero in the distribution. The measured time-of-flight is in accordance with the expected value and it is another clear evidence that the TOF readout electronics is correctly working and ready for physics data-taking.

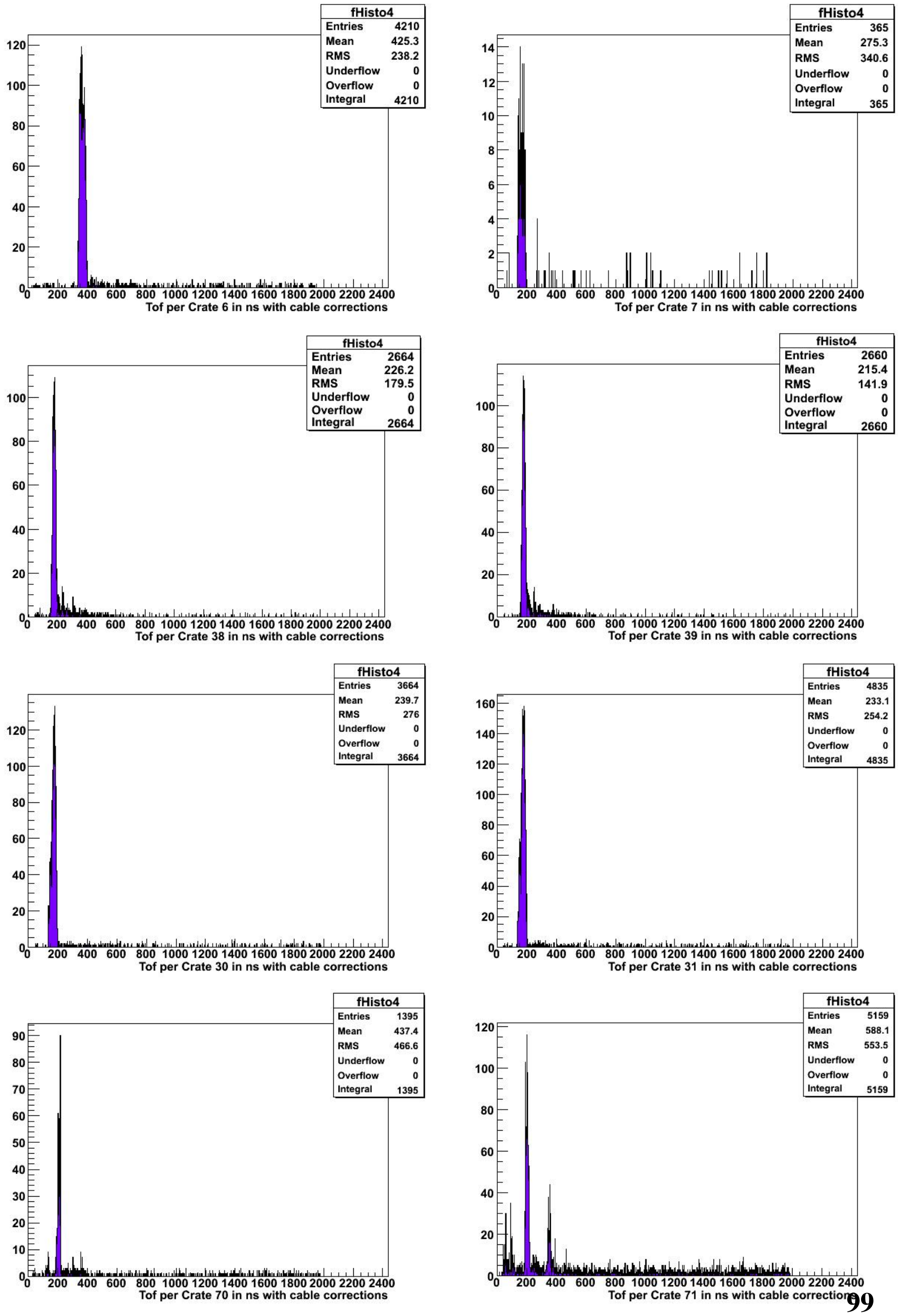

Figure 3.29: Time measured distribution for crate SM1, SM9, SM7, SM17.

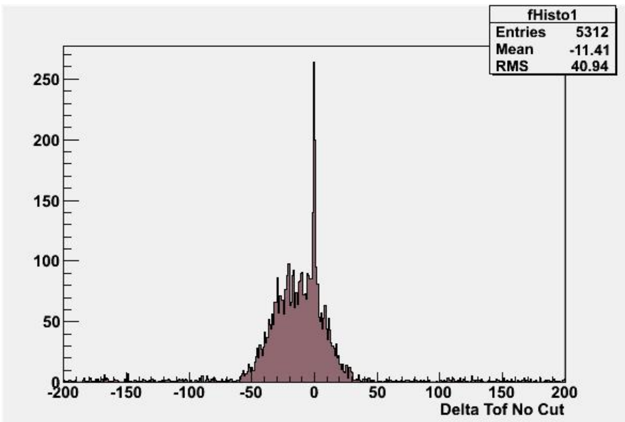

Figure 3.30: Measured time-of-flight with respect to the expected value in events triggered by the TOF. The peak at zero signals that muons have been triggered.

The TOF detector is not a tracking device, therefore a trigger based only on TOF detector information cannot select muon events without introducing some background, as it can be noticed when looking at the distribution outside the muon signal. In fact, it is not possible to tell whether two TOF signals in coincidence have been actually generated by the same particle unless computing the time-of-flight and comparing it with the expected value. Unfortunately, this is not possible at the trigger level, since the only selection can be made on the basis of poor timing requirements to flag the coincidence as a valid trigger signature. The shape of the distribution outside the muon signal is related to the time window for the coincidence. When looking at the distribution in Fig. 3.30 it seems evident that the background rate is by far larger than the muon rate with this TOF trigger configuration. It has to be kept in mind, nonetheless, that the configuration aimed to select cosmic muons with large zenithal angles and that the flux of muons at large angles is low: the probability of having a good coincidence due to a very inclined muon (large angle) crossing both sectors is suppressed with respect to the probability of random coincidences due to two almost vertical muons.

Chapter 4

Elliptic Flow

4.1 Geometry of heavy-ion collisions

In a heavy-ion collision, a probability distribution governs the degree of overlap of the two colliding nuclei from head-on (most central) down to collisions in which the nuclei barely graze each other in passing (ultra-peripheral). The degree of overlap or centrality of a collision is determined by the impact parameter b which

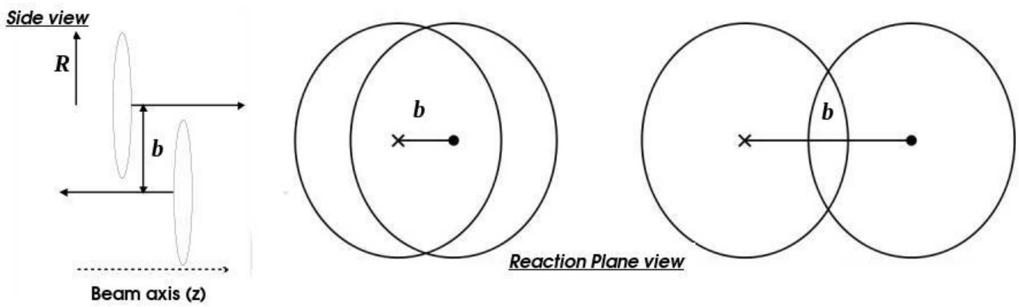

Figure 4.1: Diagram of the collision: the left panel shows the contracted nuclei in a non-central collision. R is the radius of the nucleus and b is the impact parameter or distance between the centers of the nuclei. The nucleons that lie inside the overlapping region are called *participants*, the ones that are outside, *spectators*. The central and right panels show the collision with the beam axis going into the page for a midcentral (central panel) and a peripheral (right panel) collision of two nuclei. The directions of motion of the target and projectile nuclei are into ($\times$) and out of ($\bullet$) the page respectively.

is defined as the perpendicular distance from the centre of the two colliding nuclei (illustrated in Fig. 4.1). Therefore $b = 0$ describes the most central of collisions, and $b = 2R$ describes very peripheral collisions.
Within the multiple-scattering Glauber model formalism [135, 136], the nuclear overlap function for nuclei A and B and impact parameter b is given by

$$T_{AB}(\overrightarrow{b}) = \int d^2 s T_A(\overrightarrow{s}) T_B(\overrightarrow{b} - \overrightarrow{s}) \tag{4.1}$$

where T_A and T_B are the nuclear thickness functions for nuclei A and B respectively and are given by:

$$T_A(\overrightarrow{s}) = \int dz \rho_A(z, \overrightarrow{s}) T_B(\overrightarrow{s}) = \int dz \rho_B(z, \overrightarrow{s}) \tag{4.2}$$

Here z is the beam direction and $\rho_{A(B)}$ is the nuclear density profile which is usually described by a Woods-Saxon distribution. The inclusive, inelastic cross-section, σ_{AB}, for the collision of nucleus A with nucleus B can then be related to the overlap function as:

$$\sigma_{AB} = \int d\overrightarrow{b} [1 - e^{-\sigma_{NN} T_{AB}(\overrightarrow{b})}], \tag{4.3}$$

where σ_{NN} is the nucleon-nucleon cross-section (assumed to be given by the p-p cross-section). The collision centrality in experiments is determined by relating the produced charged particle multiplicity (within an interval of pseudorapidity) to σ_{AB} . A more central collision (with small impact parameter b) will correspond to a large overlap area of the two colliding nuclei and a larger cross-section for interactions. Therefore, events with higher produced particle multiplicities correspond to more central collisions.
In the experiment, the total charged particle multiplicity distribution is measured, corrected for trigger inefficiencies, and is then divided into intervals or bins according to the percentage of the total cross-section.
When investigating experimental observables as a function of the collision centrality, a variety of variables are used to denote the centrality. For example, the variable $dN_{ch}/d\eta$, the number of charged hadrons per unit pseudorapidity, is often used due to its direct correspondence to T_{AB}. Another variable which is commonly used and which has a close connection to T_{AB} is the number of participants, N_{part}, defined as the number of nucleons (protons and neutrons) contained within

the overlap region of the two nuclei. For symmetric nucleus-nucleus collisions (i.e $A = B$):

$$N_{part}(b) = 2A \int d\overrightarrow{s} T_A(\overrightarrow{s} - \overrightarrow{b})(1 - (1 - \sigma_{NN} T_A(\overrightarrow{b}))) \tag{4.4}$$

A related quantity, used to describe the scaling of hard, perturbative processes, is the number of binary collisions, N_{bin} . In nucleus-nucleus collisions at relativistic energies where the collision can be thought of as two nuclei passing through each other, the nucleons in each nucleus have a probability of interacting more than once before traversing the full width of the other nucleus. The number of binary nucleon-nucleon interactions for the colliding nuclei A and B can be calculated as:

$$N_{bin}(b) = \sigma_{NN} \int \rho_A(z', \overrightarrow{s}) \rho_B(z'', \overrightarrow{b} - \overrightarrow{s}) d\overrightarrow{s} dz' dz'' = \sigma_{NN} T_{AB} \overrightarrow{b} \tag{4.5}$$

4.2 Elliptic flow

Non-central nucleus-nucleus collisions give rise to an elliptic overlap area. The spatial eccentricity, ε, of the reaction region is given by:

$$\varepsilon = \frac{< y^2 > - < x^2 >}{< y^2 > + < x^2 >} \tag{4.6}$$

where x and y are the Cartesian coordinates of the particles in the transverse plane. It can be calculated using Monte Carlo Glauber calculations based on the average N_{part} spatial distributions using an assumed nuclear density profile (usually a Woods-Saxon distribution). This initial spatial anisotropy which is produced at the initial collision time, can be converted into a momentum-space anisotropy (see Fig. 4.2) if the produced particles interact with each other sufficiently to produce pressure gradients (i.e in the thermodynamic limit, the system would be in local thermal equilibrium). As a result of these pressure gradients, the system expands more strongly along the short axis of the ellipse, quenching the anisotropy signal with time. Therefore, measuring the anisotropic distribution of particles can provide information on the system dynamics from the earliest stage of the system evolution.

Collective flow can be quantified in heavy-ion collisions by studying the Fourier decomposition of the azimuthal angular dependence of the particles produced.

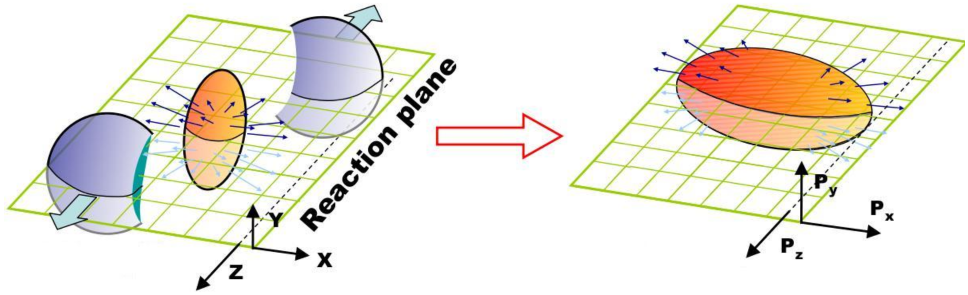

Figure 4.2: *Left*: Initial spatial anisotropy; *right*: final momentum anisotropy.

The formalism for this analysis is outlined in [154]. The particles distribution is given as:

$$E\frac{d^3N}{d^3p} = \frac{1}{2\pi}\frac{d^2N}{p_T dp_T dy}(1+\sum_{n=1}^{\infty} 2v_n cos(n(\phi - \Psi_R))) \tag{4.7}$$

where p_T and y are the transverse momentum and rapidity of a particle, ϕ is its azimuthal angle, v_n are the Fourier coefficients (anisotropy parameters) and Ψ_R is the reaction plane azimuthal angle. The **reaction plane** is defined as the plane described by the vector between the centres of the colliding nuclei and the direction of the beam axis (see Fig.4.3).

The first harmonic coefficient, v_1, is known as the **directed flow** and reflects an overall shift of the produced particles in one direction in the transverse plane. Momentum is conserved, so this shift is in opposite directions on the two sides of midrapidity in the longitudinal direction. The second harmonic coeffcient, v_2, is known as the **elliptic flow**, since in polar coordinates, for small values of v_2 , the azimuthal distribution with non-zero second harmonic describes an *ellipse* (when v_2 is large, the distribution appears dumbbell-shaped).
The Fourier coefficients can also be written as

$$v_n =< cos(n(\phi - \Psi_R)) > \tag{4.8}$$

where the average is taken over all particles in all events.
Significant elliptic flow has been observed for a large variety of hadrons by the experiments running at RHIC [138, 139] and results for identified particles from *Au-Au* collisions at $\sqrt{s_{NN}}$ = 200 GeV measured by the STAR and PHENIX experiments are presented in Fig.4.4 [49].

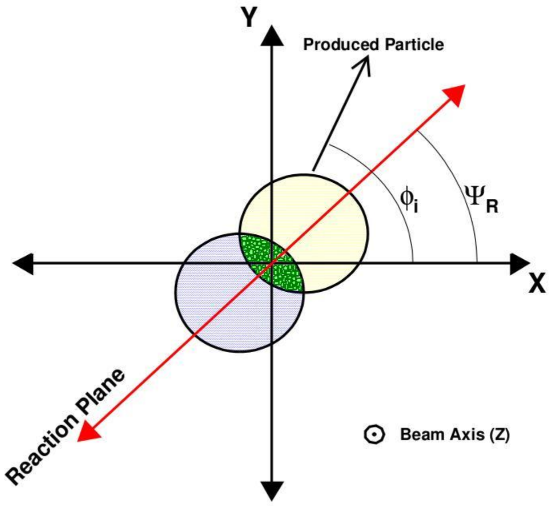

Figure 4.3: Schematic view of a collision between two heavy ions. The reaction plane angle, Ψ_R, is shown, as well as the azimuthal coordinate, ϕ_i , of a produced particle.

Several models have been used to explain and fit these data. In the next paragraphs the one that fit them better in low range, **Hydrodynamics**, and a relevant behavior at higher p_T, **Quark mass scaling**, will be shown.

4.3 Hydrodynamical models

Hydrodynamics has a long history in the study of strongly-interacting systems. Coupled with the intense interest in statistical and thermal model calculations in the early 1950's, spearheaded by Fermi and Landau [140], this led to a large body of strong interaction phenomenology which was refined throughout the years.
Hydrodynamical models have certain advantages over transport model calculations in describing heavy ion collisions. One of the most important is that, once the equation of state and initial conditions of the matter are specified, the evolution of the system is determined. No knowledge of the underlying microscopic processes is required. This is especially important when studying the predicted phase transition from hadronic to partonic degrees of freedom (and vice versa) - a process for which details are still unknown.
The hydrodynamical description is relatively simple and fulfills the conservation

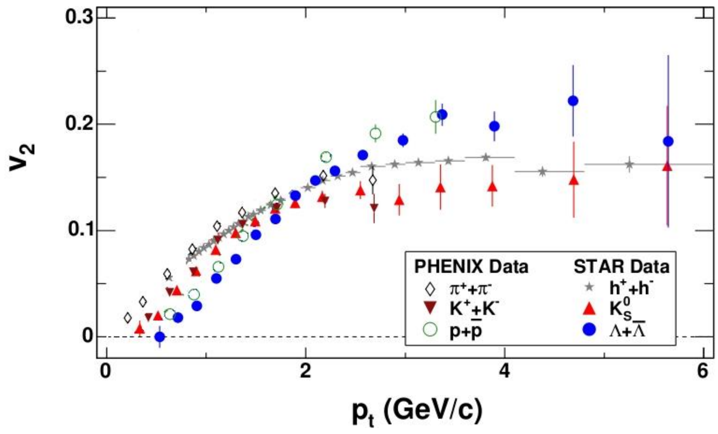

Figure 4.4: Measurements of $v_2(p_T)$ for identified particles measured by the STAR and PHENIX experiments at RHIC [49].

laws without additional constraints. The use of familiar concepts like temperature, pressure and flow velocity, also provides an intuitive and transparent picture of the evolution. The price to be paid for these advantages is a set of bold assumptions: local kinetic and chemical equilibrium and lack of dissipation. This set of assumptions may or may not be valid in such a small system as that formed in a heavy ion collision.

In a hydrodynamical description the evolution is assumed to proceed as follows. In the initial collision a large fraction of the kinetic energy of the colliding nuclei is used to create many secondary particles in a small volume. These particles will collide with each other sufficiently often to reach a state of local thermal equilibrium. When the system has reached local equilibrium, it is characterized by the fields of temperature, $T(x)$, chemical potentials associated with conserved charges, $\mu_i(x)$, and flow velocity, $u^\mu(x)$. The evolution of these fields is then determined by the hydrodynamical equations of motion until the system is so dilute that the assumption of local thermal equilibrium breaks down and the particles begin to behave as free particles instead.

The numerical solution of hydrodynamical equations of motion in all three spatial dimensions is a tedious problem. In most approaches some approximate symmetry is applied to reduce the number of spatial dimensions, where numerical solution is needed, to two dimension or one.

In the so-called Bjorken model (see Section 1.6) the main idea is the boost invari-

ance of the longitudinal flow. The longitudinal flow is assumed to be given by $v_z = z/t$ at all times. This leads to particularly simple solutions of the equations of motion since the longitudinal expansion can be solved analytically. Also it is sufficient to solve the equations of motion in the transverse plane at $z = 0$ since the solution is independent of the boosts along the beam axis. The obvious drawback in this approximation is that the observables are independent of rapidity.
In central collisions of spherical nuclei, the expansion can be simplified by assuming cylindrical symmetry. Of course this symmetry can not be applied to non-central collisions where the shape of the source has a crucial role in the buildup of elliptic anisotropy.

4.3.1 Hydrodynamic description of elliptic flow

If the dense matter formed in the nuclear collision thermalizes locally on a time scale much shorter than any macroscopic dynamical scale, its evolution can be described by ideal fluid dynamics. For large deviations from local thermal equilibrium the macroscopic hydrodynamic approach must be replaced by a microscopic kinetic one which evolves the distribution functions in both coordinate and momentum space.
Ideal fluid dynamics does not work during the initial collision stage, when the two colliding nuclei penetrate each other, converting some of their initial kinetic energy into creation of new matter, and it is also inapplicable during the last stage of the collision when the expanding matter becomes so dilute that interactions among its constituents are rare and local equilibrium breaks down. The hydrodynamic model therefore needs initial conditions (supposedly the result of an early pre-equilibrium quantum kinetic evolution leading to initial thermalization) and final conditions (a freeze-out criterium describing the transition from a locally thermalized fluid to an ensemble of free-streaming, noninteracting hadrons). The elliptic flow which is driven by the spatial anisotropy of the reaction zone in non-central collisions and the resulting anisotropic pressure gradients: as shown in [141], at RHIC energies, for not too peripheral *Au-Au* collisions, the momentum anisotropy saturates before the completion of hadronization, due to the disappearance of the spatial deformation of the fireball. The measured v_2 thus reflects almost exclusively the early QGP dynamics and the phase transition region. Figure 4.5 [142] shows that the corresponding hydrodynamic predictions work very well, at least for transverse momenta below about 1.5-2 GeV/c where most ($> 99\%$) of the particles are emitted.

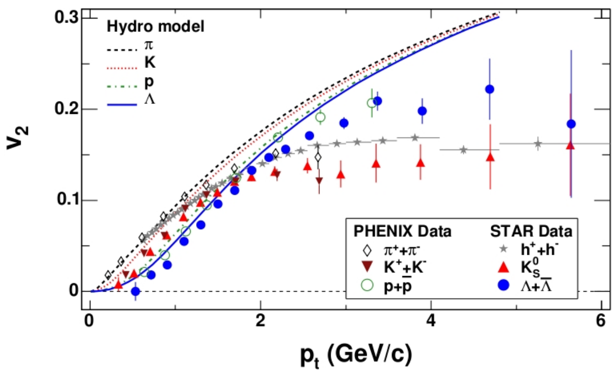

Figure 4.5: Differential elliptic flow $v_2(p_T)$ for several identified hadron species from minimum bias *Au-Au* collisions at 200 A GeV compared with hydrodynamic predictions [142].

Hydrodynamics predicts a characteristic rest mass dependence of v_2 [143] which is nicely reproduced by the data in Fig. 4.5. This *fine structure* constitutes compelling evidence that the hot matter produced at RHIC behaves like a thermalized fluid. The *mass scaling* of v_2 seen at low p_T is quite distinct from the *quark number scaling* of v_2 seen at larger transverse momenta $p_T \gtrsim 2-4$ GeV/c; the latter is characteristic of a quark-coalescence mechanism for hadron production which dominates in that p_T range [145] and will be described in section 4.4.

4.3.2 Limit of hydrodynamic

The elliptic flow coeffficient $v_2(p_T)$ is a measure for the (relatively small) differences between the transverse momentum spectra with momenta pointing into and perpendicular to the reaction plane. As such, it is more sensitive to deviations from ideal hydrodynamic behaviour than the overall shapes (slope parameters) of the transverse momentum spectra. Several model studies [146] shown that v_2 reacts particularly strongly to shear viscosity: this connection has been allowed to answer the question how large the QGP viscosity might be.
The upper limit for η/s looks like $\eta/s > 3(\eta/s)_{min}$, where $(\eta/s)_{min} = 1/4\pi \sim 0.08$ is a conjectured absolute lower limit on the specific shear viscosity for any fluid, derived for strongly coupled conformally invariant supersymmetric field theories using the AdS/CFT correspondence [147]. Since all known classical fluids

have $\eta/s \gg 1$ at all temperatures, even at their boiling points where η/s typically reaches a minimum [147], this makes the QGP the most perfect fluid of any studied so far in the laboratory [148]. The increasing deviation from the ideal fluid limit for growing p_T is qualitatively consistent with the expected influence of sheart viscosity: it has been shown that viscous corrections to the local thermal equilibrium distribution function increase in first oredr quadratically with p_T, leading to stronger and stronger reduction of v_2 below the ideal fluid limit as p_T grows [142]. These arguments show that deviations from ideal fluid dynamics at high p_T must be expected, and that they can be large even for fluids with very low viscosity.
Figure 4.5, however, shows that mesons seem to deviate from the ideal fluid dynamical prediction earlier than baryons which follow the hydrodynamic curves to considerably larger p_T , thereby reaching significantly larger saturation values for v_2. Why should viscous effects be different for baryons and mesons? In fact, both the p_T-value where v_2 begins to drop below the hydrodynamic prediction and the asymptotic saturation values of v_2 appear to be independent of the hadron mass and only care about whether the hadron is a meson or a baryon. This behaviour will be presented deeper in the next paragraph.

4.4 Quark mass scaling

At transverse momentum $1.5 < p_T < 5$ GeV/c the elliptic flow of different particle species starts to deviate significantly from the mass ordering schematics discussed above, see Fig.4.5 and 4.6. Interestingly, different particle species seem to exhibit a different value of saturation for v_2, while they fall on top of each other if grouped into mesons and baryons. While at low p_T the lighter mesons have a larger v_2 for a given p_T , at intermediate p_T the elliptic flow of mesons is smaller than that of baryons.

Quark coalescence models provide an elegant explanation for this observed feature. These models assume that in this p_T range, particle production is dominated by coalescing quarks: two quarks moving with the same momentum make up a meson with twice the momentum of the original quarks, three quarks coalesce into a baryon with three times the quark momentum [104]. Therefore, by scaling the observed v_2 signal and the transverse momentum by the number of constituent quarks n one obtains the underlying quark flow. The results, as shown in Fig. 4.7, are very intriguing. In the region $0.6 < p_T/n < 2$ GeV/c of scaled

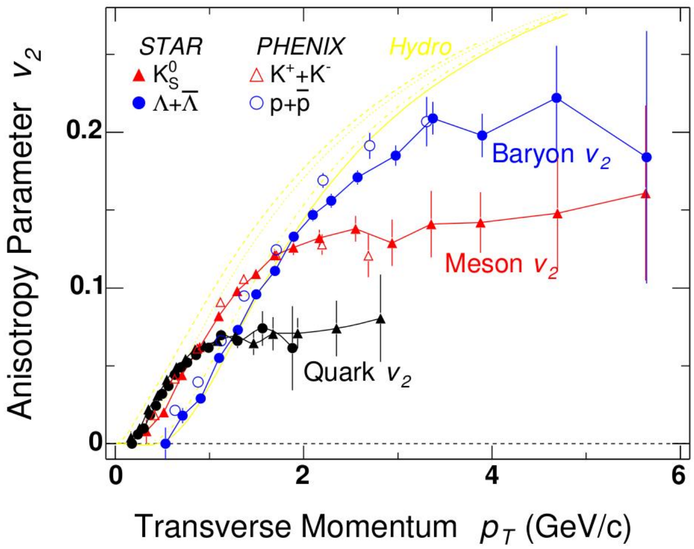

Figure 4.6: Identified particle v_2 , hydrodynamic predictions, and elliptic flow of quarks derived from number-of-constituent quark scaling [144].

particle momentum, elliptic flow for different particles is literally the same. Only the pions deviate from the universal curve, which can be explained by feed-down from resonances.

The success of these quark coalescence models in describing the measured v_2 is a strong hint that the observed large anisotropic flow builds up at the partonic stage of the system's evolution already. On one hand this suggests that the system evolves through a state of partonic degrees of freedom, which, on the other hand, suffer a lot of rescattering and therefore should be close to local thermal equilibrium.

Hadronic transport models, *Relativistic Quantum Molecular Dynamics* (**RQMD** [150]) and *Ultra-relativistic Quantum Molecular Dynamics* (**UrQMD** [151]), can also qualitatively reproduce the observed mass ordering of v_2 (p_T) at low p_T [152] and quark-number scaling at higher p_T [153] based on rescattering of hadrons. The quark number scaling is due to the model calculations dependence on the additive quark model for hadronic interaction cross-sections. However, although these models can qualitatively reproduce the observed trends, the calculated $v_2(p_T)$ values are only $\sim 60\%$ of the experimentally observed values. This may indicate

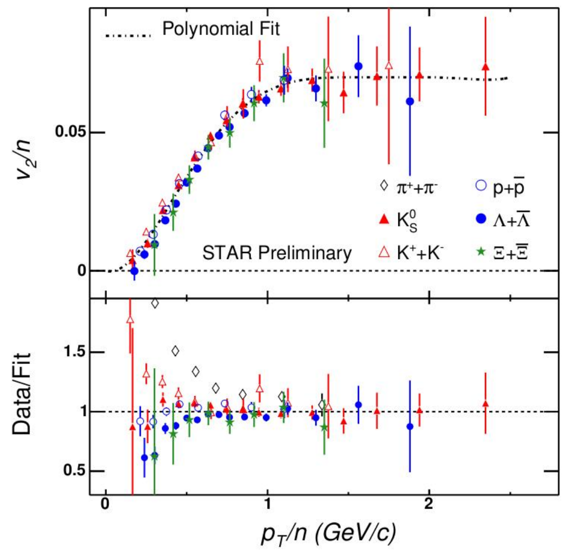

Figure 4.7: *Top panel*: v_2/n *vs* p_T/n where n is the number of constituent quarks for identified particles measured by the STAR experiment [49]. The dash-dotted line is a polynomial fit to the data. *Bottom panel*: Data from the top panel divided by the polynomial fit as a function of p_T/n. [49]

that significant flow is built up prior to hadronization in the partonic stage, since hadronic scatterings alone cannot reproduce the large experimentally observed values.
Therefore in the context of both coalescence models and hadronic transport models, the observed v_2 values seem to indicate that elliptic flow is built up prior to hadronization in the partonic phase.

4.5 Description of the sample

The study earned on during this thesis work is aimed to set up analysis tools for the measurement of phi meson elliptic flow in the ALICE experiment at LHC. As before pointed up, heavy-collisions at LHC will start in Fall 2010 so it is not yet possible to perform this analysis on real data. For this reason the GeVSim MC Event Generator has been utilized to produce a sample of simulated data.
GeVSim [1] is a fast and simple to use Monte-Carlo event generator implemented

in AliRoot, the ALICE offline framework (see section 2.3.11). It can provide events that can be configured by the user according to the specific needs of a simulation project, in particular that of flow and event-by-event fluctuation studies. GeVSim is written in C++ and extensively uses the capabilities of Root [117]. It generates a list of particles by randomly sampling a distribution function with no intention to describe the space-time evolution of the system. The azimuthal distribution is factored from the transverse momentum and rapidity distribution. Momentum spectra can be either selected from a menu of predefined distributions or provided by the user. The parameters of single particle spectra and their fluctuations are explicitly defined by the user for each particle type separately. Those include the flow coefficients, inverse slope parameter of p_T distributions, rapidity width and particle multiplicity.
The azimuthal distribution is described by two Fourier coefficients representing directed and elliptic flow, which can either be set to a constant value or parametrized as a function of p_T and rapidity. The parameterizations provided are based on the results obtained by STAR experiment at RHIC.
The multiplicity, the flow coefficients, the particle species and all the other parameters that the user can provide to the generator have been set following the latest experimental results in order to allow a good cross-check for a future measurement.
In particular the maximum elliptic flow parameter v_2 has been fixed at 0.05 (it differs for each particle and for each p_T).
The needed statistic for a proper estimate, requested to guarantee that each bin in centrality and p_T be sufficiently populated, is of the order of 10^7 events. Each event occupies a memory space of $5Gb$ and the time computation to produce it is of 3 minutes: such MC production should be performed in something like 114 years!!! ...taking up to $10^5 Tb$ of memory space. Even performing the estimate integrating all centrality and p_T, the production would have lasted almost 6 years on $5000Tb$.
In order to perfom a first study without waiting real data, a data sample of 975530 events of *Pb-Pb* collisions with the same multiplicity (almost central collisions, $dN/d\eta = 2000$) has been generated on a computer farm of 'Dipartimento di Fisica E.R. Caianiello' of Salerno University and INFN Gruppo Collegato: the particles inserted in the simulations are $\pi^{\pm}, K^{\pm}, p, \overline{p}, \phi$ with the same particle ratio of Hijing generator.
To avoid further waste of CPU, the simulation has not been propagated in the detector reducing in this way the time consumption to 30 s. At this step the generator

doesn't let decay the ϕ meson so another step of simulation has been added just for this kind of particle: the propagation in the detector.
The information on the recostruction has been added during the analysis step using cuts based on TOF detector acceptance and efficiency with Hit Or Miss method; the values for cuts have been taken from results already exposed in Fig. 3.4 in section 3.1. Moreover an η dependence has been applied, using reference values taken from [126].
In this way the total used space has been $2Mb$ for event, i.e. $\sim 2Tb$ for the total production that has taken place in nine months with the use of up to 32 processors.
In the following sections the method for the elliptic flow extraction and the results on this sample will be shown.

4.6 Measuring Fourier Harmonics with Event Planes

In order to measure the elliptic flow as described in section 4.2, the reaction plane angle, Ψ_R, (which is unknown) has to be estimated on an event-by-event basis. The estimated reaction plane is usually called the **event plane**.
Once the event plane is determined using the detected particles in an event, the flow is determined by correlating the azimuthal coordinates of the particles with this event plane and extracting the Fourier coefficients that best describe the pattern.
We follow the method and equations derived in [154] which uses the anisotropic flow itself to determine the event plane. The event plane is reconstructed from the n^{th} order *event flow vector* $\vec{Q}_n$ [155], defined as

$$\vec{Q}_n = (X_n, Y_n), \tag{4.9}$$

where the index n refers to the n^{th} component of the Fourier series. Given as a function of the azimuthal coordinates of the produced particles in the transverse plane of the collision, the flow vector components are:

$$\vec{X}_n = Q_n cos(n\Psi_n) = \sum_i w_i cos(n\phi_i) \tag{4.10}$$

and

$$\vec{Y}_n = Q_n sin(n\Psi_n) = \sum_i w_i sin(n\phi_i) \tag{4.11}$$

where w_i are weights and i is the index of particles used in the determination of the event plane. Given these relations, the event plane angle, Ψ_n, can be found by solving equations (4.10) and(4.11) for Ψ_n from the components of the flow vector according to

$$\Psi_n = tan^{-1}\left(\frac{Y_n}{X_n}\right) = \frac{1}{n}tan^{-1}\left(\frac{\sum_i w_i sin(n\phi_i)}{\sum_i w_i cos(n\phi_i)}\right) \quad (4.12)$$

Notice that an event plane angle, Ψ_n, can be found for each harmonic, n, of the azimuthal distribution, and that the angular range of Ψ_n is $0 \leq \phi \leq 2\pi/n$. Each n^{th} order event plane angle represents a similar angular estimate of the true reaction plane angle, but modulated by a phase of $2\pi/n$. An usual weighting is such that $w_i = p_{Ti} \times w_\phi$. The ϕ-weight factor, w_ϕ, is necessary to correct for detector acceptance effects which can lead to anisotropic particle distributions in the lab frame which are not due to anisotropic flow. Therefore it is necessary to ensure that the event plane angle distribution over all events is isotropic (i.e. flat with respect to azimuthal angle ϕ).
The method has been used to estimate the reaction plane angle for the following analysis of elliptic flow (n=2) on a sample of 975530 generated heavy ions collisions events (see section 4.5), the result are shown in Fig. 4.8, where the estimated

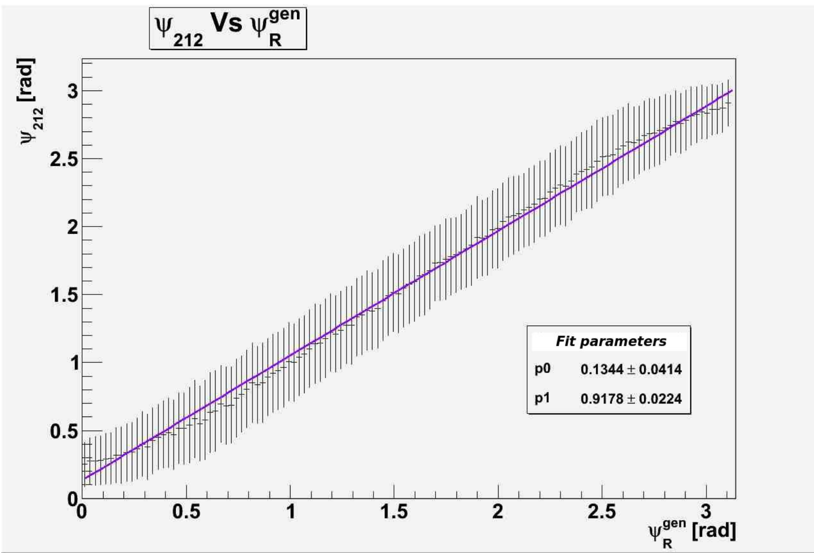

Figure 4.8: The reaction plane angle estimated with the method described in the text (Ψ_{212}) vs the generated one (Ψ_R^{gen}).

reaction plane angle has been plotted vs the generated value, for all the events.

It's clear that there is a very good accordance between the two values; in fact for each event, the reconstructed event plane is consistent, within errors, with the generated one, that here represent the real one. This means that, with this method, it will be possible to obtain a reliable estimate of reaction plane angle of the collisions that will occurr in the ALICE experiment. A fit of the points of the plot with a linear function

$$y = p0 + p1 * x \tag{4.13}$$

has been performed; the obtained values for the fit parameters are

$$p0 = 0.13 \pm 0.04 \qquad\qquad p1 = 0.92 \pm 0.02 \tag{4.14}$$

The plot points are distributed throughout a parallel (and very close) to the bisector of the first quadrant angle, confirming the good agreement of the reconstructed reaction plane angle and the generated one, for each event.

4.6.1 Transverse sphericity tensor method

Another method that is possible to use to estimate the reaction plane angle and the v_2 of an ultrarelativistic collision is described in [156]. From the measured momenta in a collision with multiplicity M, it's possible to construct the transverse sphericity tensor defined in the center-of-mass frame as

$$S_{ij} = \sum_{k=1}^{M} w(k) p_i(k) p_j(k) \tag{4.15}$$

where $p_i (i = 1, 2)$ is the i^{th} component of the momentum in the trasverse plane and w(k) a weight related to the particle's mass. In this way, the ratio between the two eigenvalues ($\lambda_2 > \lambda_1$)

$$\frac{\lambda_2 - \lambda_1}{\lambda_2 + \lambda_1} \tag{4.16}$$

is equal to v_2 and one of the eigenvectors is the reaction plane angle.
In Fig. 4.9 is shown the result obtained on the data sample described in section 4.5 compared with the generated event plane (top panel) and with the value obtained with the method explained in section 4.6 (bottom panel), for all the events. Also with this method, as for the one described in the previous subsection, there is a very good agreement between the reconstructed event plane and the generated

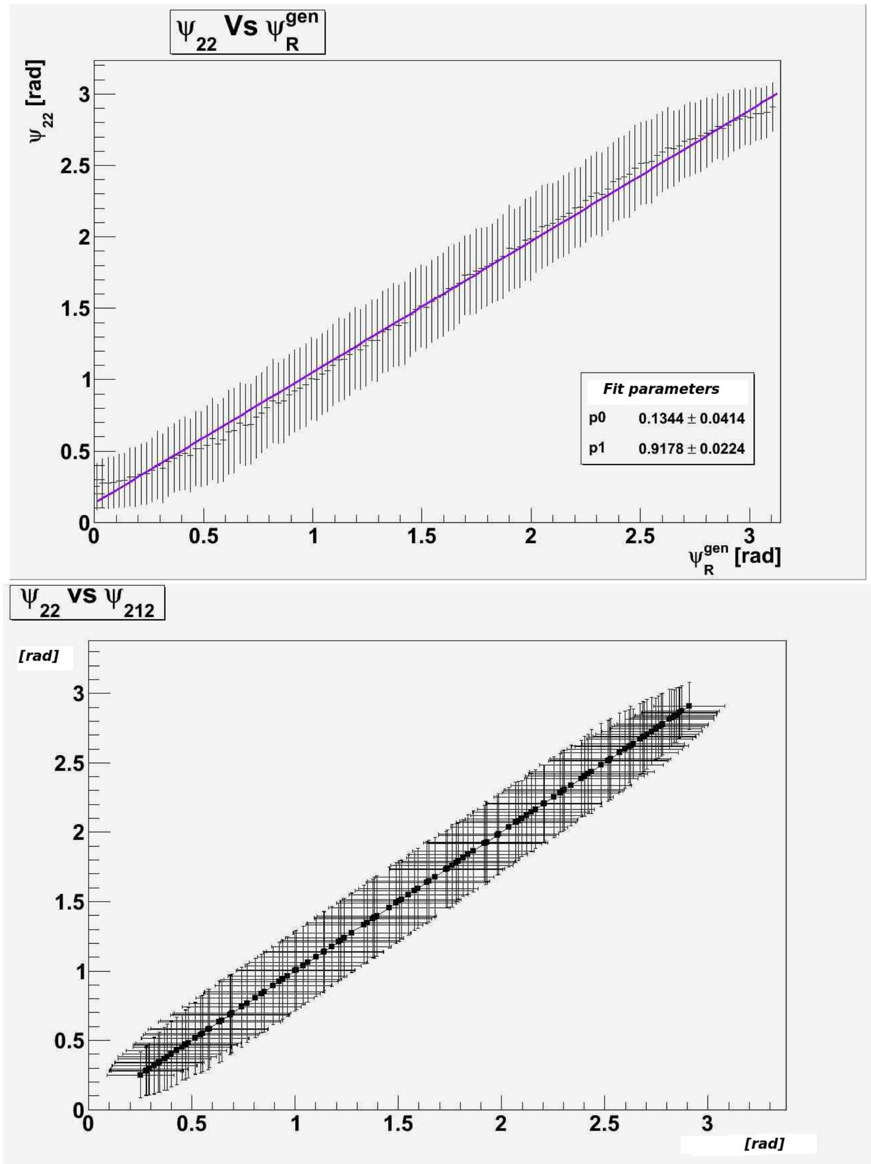

Figure 4.9: *Top panel*: the reaction plane angle estimated with the transverse sphericity tensor method (Ψ_{22}) vs the generated one (Ψ_R^{gen}); *Bottom panel*: the reaction plane angle estimated with the transverse sphericity tensor method (Ψ_{22}) vs Ψ_{212} (see Fig.4.8).

one, for each event, within errors. For the upper plot of Fig. 4.9, a linear fit has been performed with a linear function

$$y = p0 + p1 * x \tag{4.17}$$

the obtained values for the fit parameters are

$$p0 = 0.13 \pm 0.04 \qquad p1 = 0.92 \pm 0.02 \tag{4.18}$$

We can notice that this values are the same obtained in the previous subsection: also in this case the plot points are distributed throughout a parallel (and very close) to the bisector of the first quadrant angle, showing a good accordance between the result of this methods with the waiting values (the generated ones). This method constitute a second way to obtain a reliable estimate of reaction plane angle of the collisions that will occurr in the ALICE experiment and a cross check for the results that will be obtained with the method exposed in section 4.6.

4.6.2 Elliptic Flow analysis

Given the previous discussion, in order to measure the elliptic flow parameter, v_2, one uses the n=2 case for Eq. 4.12 to estimate the event plane angle.
The observed flow signal, v_2, using the 2^{th} harmonic event plane, Ψ_2, is then obtained fitting the $\phi_i - \Psi_2$ distribution with the function [154]:

$$\frac{dN}{d(\phi_i - \Psi_2)} = P_0 \frac{1}{2\pi}[1 + 2v_2^{obs} cos(\phi_i - \Psi_2)] \tag{4.19}$$

As mentioned before, two separate subevents, a and b, are used to find the event plane resolution and the error on the v_2 estimate. The results of this method on the sample described in section 4.5 are shown in Fig. 4.10, 4.11 and 4.12. In particular, the analysis has been performed using the angle of all charged particlesthat can be directly detected with ALICE (no resonances), after already mentioned cuts. on the left, Ψ_{gen} is the generated reaction plane angle, taken directly from the generator, Ψ_{212} and Ψ_{22} have been calculated, respectively, with the Eq. 4.12 and with transverse sphericity tensor method. The results agree within the errors: the estimate elliptic flow using the reaction plane angle with both methods

$$v_2 = 0.019 \pm 0.06 \tag{4.20}$$

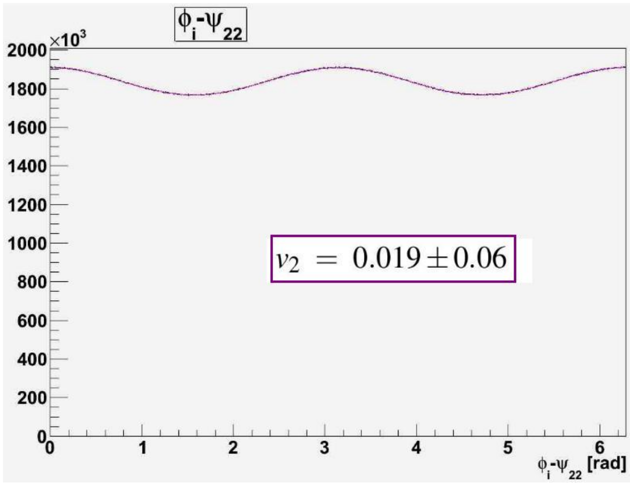

Figure 4.10: The $\phi_i - \Psi_2$ distribution fitted in order to extract the v_2. In this plot the reaction plane angle (Ψ_2), here called Ψ_{212}, has been estimated with the event flow vector method (see section4.6).

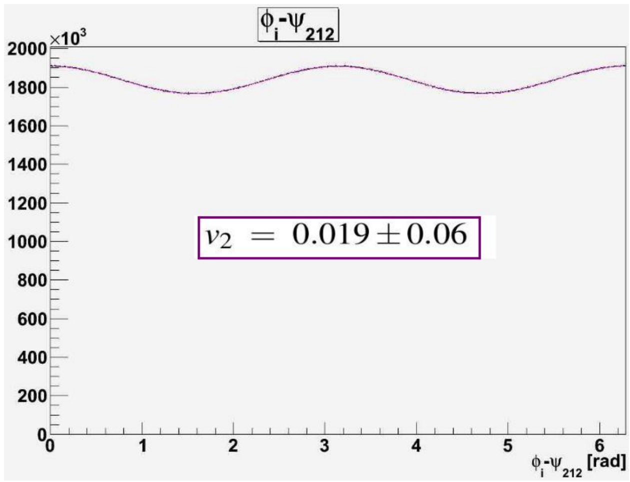

Figure 4.11: The $\phi_i - \Psi_2$ distribution fitted in order to extract the v_2. In this plot the reaction plane angle (Ψ_2), here called Ψ_{22}, has been estimated with the transverse sphericity tensor method (see subsection 4.6.1).

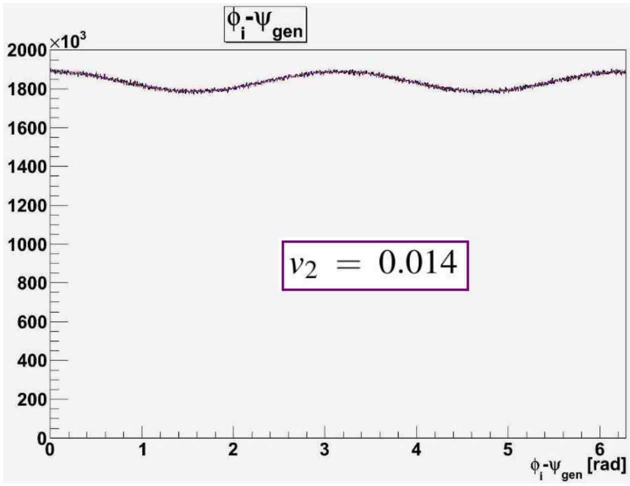

Figure 4.12: The $\phi_i - \Psi_2$ distribution fitted in order to extract the v_2. In this plot the reaction plane angle (Ψ_2), here called Ψ_R^{gen}, is the generated one.

is consistent with the generated one

$$v_2 = 0.014. \tag{4.21}$$

This method can be used to measure the elliptic flow coefficient of all charged particles with the ALICE detector.

4.7 Phi meson's Elliptic Flow

The ϕ vector meson is the lightest bound state of hidden strangeness, consisting of a ($s\bar{s}$) quark-antiquark pair. Although it is a meson, it is heavy in comparison with mesons consisting of u and d quarks, having a mass (m_ϕ = 1019.455 $\pm$ 0.020 MeV/c^2) [157] comparable to the proton and Λ baryons. Due to the ϕ being composed solely of s and $\bar{s}$ quark, phenomenologically it is expected to have a very small cross-section for interactions with non-strange hadrons [158] and therefore, its observables should remain largely undisturbed by the hadronic rescattering phase of the system evolution. Measurements of ϕ-photoproduction from various nuclei [159, 160] have reported a range of values for the extracted ϕ-nucleon cross-section but yet remain to be conclusive. However, experimental evidence for the small interaction cross-section of the ϕ has been presented in

Fig. 1.15 where the values for the freeze-out temperature T_{fo} and mean velocity β extracted from blast-wave fits to the central ϕ-meson p_T spectrum differ from those extracted for π, K, p and ϕ seems to freeze out at a higher temperature and lower β [49]. This is also observed for the multistrange Ω baryon. The ϕ also has a relatively long life-time of $\sim$46 fm/c which means that it will mostly decay outside the fireball and therefore its decay daughters will not have much time to rescatter in the hadronic phase. Experimental measurements of the ϕ/K^- ratio as a function of centrality have also ruled out the possibility of ϕ production via K^+K^- coalescence in the hadronic stage [161]. The observed ratios are flat as a function of centrality in contradiction to expectations from hadronic rescattering models which include kaon coalescence as a ϕ-meson production mechanism and which therefore predict the ϕ/K^- ratio to increase as a function of centrality. These properties make the ϕ-meson an excellent probe of the hot and dense medium created in nucleus-nucleus collisions.

Measurements of the ϕ-meson in terms of the bulk observables discussed in the first chapter, can provide important information on the properties of the medium and particle production mechanisms in ultra-relativistic collisions.

The degree of collectivity of the medium that has been produced at RHIC has been further probed by measuring the elliptic flow of the ϕ-meson. Since multistrange hadrons and particles with hidden-strangeness are assumed to freeze out early and undergo fewer interactions in the hadronic stage, their v_2 signals should provide a clean signal from the early stage of the system evolution. First measurements of the Ξ (ssd) and Ω(sss) elliptic flow have indicated that these particles flow at least as much as particles consisting of the lighter u and d quarks alone [162] which implies that collectivity of the system is built up in the partonic stage, one of the considtions of QGP formation. Measurements of the ϕ-meson v_2 and whether it also scales according to its number of constituent quarks as other identified particles are seen to do, provide important information on the collectivity and possible deconfinement of the system in the early stage and serve to constrain different dynamical models of elliptic flow (e.g. hydrodynamical and hadron transport models) and particle production. The ϕ-meson with its mass comparable to Λ and p, and low interaction cross-section, can be exploited as an ideal tool to probe the bulk properties of the medium produced in nucleus-nucleus collisions. In addition to the wealth of data on other identified particles, ϕ-meson observables help to distinguish further between different physical models of the dense medium and help to open the way towards further understanding of the system created in ultra-relativistic heavy-ion collisions.

In Fig 4.13 the measurement of ϕ-meson $v_2(p_T)$ is compared to the v_2 results for Λ and K^0_S, all measured by STAR [163]. At low p_T ($p_T < 2GeV/c$), one can observe a mass-ordered hierarchy (within the errors) in the v_2 values of the studied particles. The ϕ-meson v_2 trend falls between that of the lighter K^0_S and heavier Λ. This is consistent with the expectation from hydrodynamics where particles boosted with a common velocity will appear shifted in the p_T variable due to their different masses. As mentioned in section 4.4, the phenomenon of quark number scaling, where the $v_2(p_T)$ of mesons and baryons scales according to their number of valence quarks, has been observed in *Au-Au* collisions at RHIC at intermediate p_T , $2 < p_T < 5$. The dotted and dashed lines in Fig. 4.13 are parameterizations for baryon (NQ = 3) and meson-scaling (NQ = 2). One can see that in the intermediate p_T range, the $v_2(p_T)$ of the ϕ-meson is consistent with that of the K^0_S and the parameterization for meson-scaling (NQ = 2). Within the errors, the values obtained (NQ=2.3 ± 0.4) have shown that the v_2^{ϕ} results follow the meson-scaling trend.

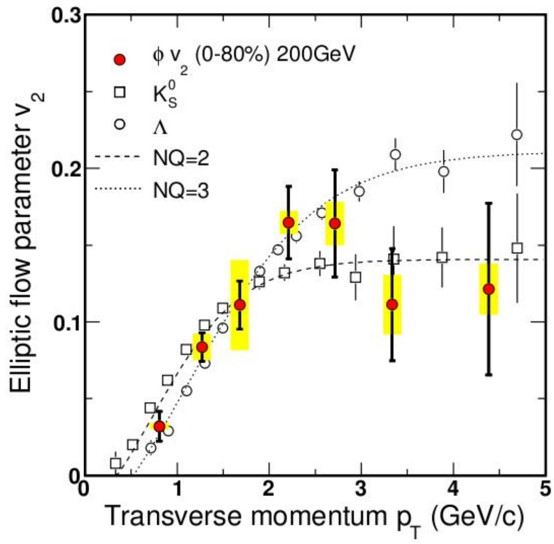

Figure 4.13: Minimum bias (0-80% centrality bin) $v_2(p_T)$ for *Au-Au* collisions at $\sqrt{s_{NN}}$ = 200 GeV for ϕ-meson, Λ and K^0_S. The dashed and dotted lines represent parameterizations for number of quark (NQ) scaling equal to 2 and 3 respectively. Data from the STAR experiment.

This measurement has confirmed both hydrodynamical models, that describe a transition to a nearly ideal fluid QGP, and quark coalescence models, that assume that particle production, and v_2 behaviour, is dominated by coalescing quarks in the QGP. Since the hypothesis of ϕ-meson production from coalescence of s and $\bar{s}$ quarks, is still open, a measure of ϕ-meson elliptic flow at LHC energies with ALICE experiment could clarify such a pictures, with a more evident probe of QGP formation or open new fascinating scenarios.
The greatest difficulty in such measurement lies in the impossibility of a direct knowledge of ϕ-meson kinematics informations. In the ALICE experiment analysis framework, AliRoot (introduced in section 2.3.11), there are several tools for the study of charged particles flow but there isn't any instrument to measure flow for a resonance like ϕ-meson, for which it's possible to identify only the presence of the signal over the background with recostruction of the decay fragment.
In the next section the method for the first measurement of this parameter within the ALICE experiment will be illustrated and a result on the MC sample, described in section 4.5, will be presented.

4.8 Extracting the ϕ-meson elliptic flow

There are different variations of the event plane method that is possible to use in order to extract the ϕ-meson elliptic flow: here we will show the details of the ϕ-binning method [154] and the v_2 *vs* m_{inv} method [164]. The v_2 *vs* m_{inv} method is the newer of the two methods and the results using this method are presented in the next section. As a second step, the ϕ-binning method will be used as cross-check for the other method.

4.8.1 The ϕ-binning method

The ϕ-binning method for extracting the v_2 of identified particles consists of measuring the raw yield of the chosen particle in bins of the angle $(\phi - \Psi)$ where ϕ is the azimuthal angle of the particle in the lab-frame and Ψ is the event plane angle. The distribution can then be fitted with the functional form:

$$\frac{dN}{d(\phi_i - \Psi_2)} = P_0 \frac{1}{2\pi}[1 + 2v_2^{obs} cos(\phi_i - \Psi_2)] \qquad (4.22)$$

where v_2 is one of the fit parameters. The p_T dependence of the elliptic flow can be measured by repeating the procedure for fixed ranges in p_T. A first estimate of

v_2 with this method on all the particle has been shown on section 4.6.2.
For the case of resonances, where the signal typically consists of a small particle mass peak sitting above a large combinatorial background (i.e. the signal to background ratio is less than unity), it is already a difficult task to extract raw yields accurately. This method of extracting v_2 requires that, for each bin in p_T, the already small signal is further divided into bins as a function of $(\phi - \Psi)$ angle which can lead to large systematic errors in extracting the raw yields since the fits to the invariant mass peak are difficult to constrain. The result is that large systematic errors, due to uncertainties in the raw yields, are propagated into the final v_2 result. For this reason, the method described in this section will not be used as first check of a measure of ϕ meson elliptic flow, it should need more statistic as already explained in section 4.5. It has been used in order to extrapolate the generated phi meson elliptic flow, using directly the azimuthal angle of phi meson as provided from the generator.
In Fig. 4.14 the result for one p_T bin is shown.

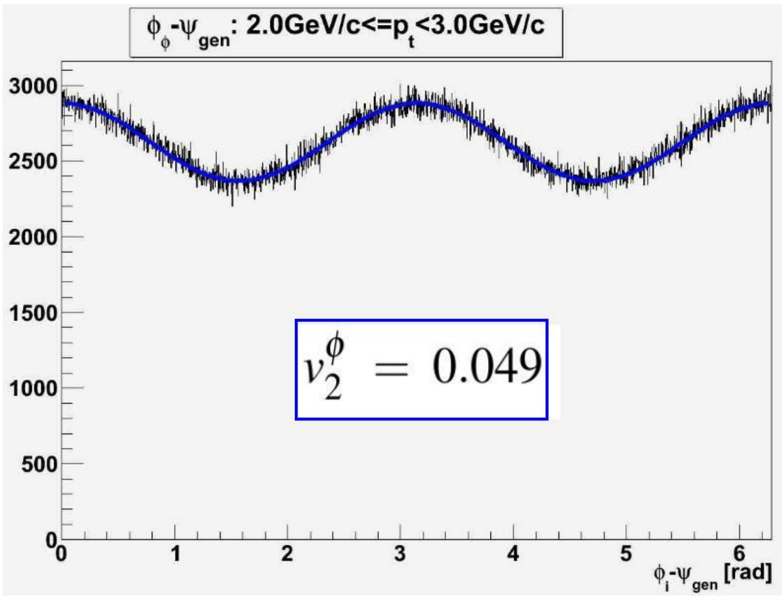

Figure 4.14: The $\phi_\phi - \Psi_{gen}$ distribution has been fitted with 4.22 in order to extrapolated the generated value for phi mesons elliptic flow.

Therefore the reference values for the generated ϕ meson elliptic flow for three p_T bins in the following analysis will be:

p_T (GeV/c)	[0.5,1[	[1, 2]	[2,3[
v_2	0.018	0.033	0.049

4.8.2 The v_2 *vs* m_{inv} method

The v_2 *vs* m_{inv} method was inspired by [164] and a brief description of the phenomenology is outlined below. For single particles, in the laboratory frame, the probability distribution in terms of the azimuthal angle ϕ can be written as:

$$p(\phi - \Psi_R) = \frac{1}{2\pi} \sum_{n=-\infty}^{+\infty} v_n e^{in(\phi - \Psi_R)} \tag{4.23}$$

where ϕ is the angle of the particle measured in the laboratory frame and Ψ_R is the reaction plane angle. In the case of a symmetric system with real v_n , equation 4.23 reduces to:

$$p(\phi - \Psi_R) = \frac{1}{2\pi}[1 + 2\sum_{n=1}^{\infty} v_n cos(n(\phi - \Psi_R)] \tag{4.24}$$

which is just the probability analogue of equation 4.7. Following [164], equation 4.23 can be extended for pairs of particles as:

$$p(\phi_{pair} - \Psi_R) = \frac{1}{2\pi} \sum_{n=-\infty}^{+\infty} v_n^{pair} e^{in(\phi_{pair} - \Psi_R)} \tag{4.25}$$

where ϕ has been replaced with ϕ_{pair} .
In the case of a resonance particle (e.g. the ϕ-meson) which decays to two daughter particles (e.g. $\phi \to K^+K^-$), ϕ_{pair} is the azimuthal angle of the parent resonance particle.
In equation 4.25, v_n^{pair} are called the *pair-flow* coefficients, but unlike in the previous case of single particles, v_n^{pair} are not necessarily real numbers with the result that the sine terms become part of the Fourier expansion such that:

$$p(\phi_{pair} - \Psi_R) = \frac{1}{2\pi}[1 + 2\sum_{n=1}^{\infty} (v_{c,n}^{pair} cos(n(\phi_{pair} - \Psi_R) + v_{s,n}^{pair} sin(n(\phi_{pair} - \Psi_R))] \tag{4.26}$$

where $v_{c,n}^{pair} = cos\ n(\phi_{pair} - \Psi_R)$ and $v_{s,n}^{pair} = sin\ n(\phi_{pair} - \Psi_R)$.
For a resonance particle which is identified through its mass peak in an invariant mass distribution consisting of all combinations of candidate decay daughter

particle pairs, the invariant mass distribution can be separated into:

$$N_{pairs}(m_{inv}) = N_b(m_{inv}) + N_s(m_{inv}) \tag{4.27}$$

where N_b is the number of combinatorial background pairs and N_s is the number of signal pairs (i.e. the number of real particles). In a similar way, for the ϕ-meson, we can write the contributions to the pair-flow coefficients as:

$$N_{pairs}(m_{inv})v_{c,n}(m_{inv}) = N_b(m_{inv})v_{c,n}(m_{inv}) + N_{\phi,n}(m_{inv})v_{c,n} \tag{4.28}$$

$$N_{pairs}(m_{inv})v_{s,n}(m_{inv}) = N_b(m_{inv})v_{s,n}(m_{inv}) + N_{\phi,n}(m_{inv})v_{s,n} \tag{4.29}$$

Symmetry of ϕ-mesons production with respect to the reaction plane implies that $v^{\phi}_{s,n} = 0$ and if the background is composed of uncorrelated particles, then $v^{b}_{s,n} = 0$ [164].
Experimentally, the v_2 *vs* m_{inv} method as it is applied here, involves estimating the event plane angle in the same way as explained in section 4.5 and then measuring the $v_2 = cos2(\phi - \Psi_R)$ of all same-event combinations of positive and negative kaon pairs as a function of invariant mass. For this reason, the performance of TOF detector in the kaon identification play a crucial role in such measurement in the ALICE experiment.
Based on equation 4.28, the v_2 distribution as a function of m_{inv} can then be fitted using:

$$v_{2Tot}(m_{inv}) = v_{2S}\alpha(m_{inv}) + v_{2B}(m_{inv})[1 - \alpha(m_{inv})] \tag{4.30}$$

where v_{2Tot} is the total v_2, v_{2S} is the v_2 of the signal (i.e. the ϕ-meson), and v_{2B} is the background v_2. $\alpha(m_{inv}) = S/(S+B)$ is ratio of the signal over the sum of the signal plus background m_{inv} distributions. The ratio is function of invariant mass and is extracted (once only per p_T bin) by fitting the distribution using a Breit-Wigner function (to describe the ϕ-meson mass peak shape) plus a polynomial (to parameterize the background shape).
Therefore, in this method, the raw yield of ϕ-mesons needs to be extracted once per p_T bin. In Fig. 4.15, the mass invariant distribution for phi meson obtained analyzing the sample described in section 4.5, after the cut of the background, is shown.
In the fit of Eq. 4.30, v_{2S} is a parameter in the fit and v_{2B} is parameterised using a polynomial in m_{inv}; the coefficient of this polynomial are taken from the result of the background fitting.
In order to check the validity of the v_2 results obtained using this method, the

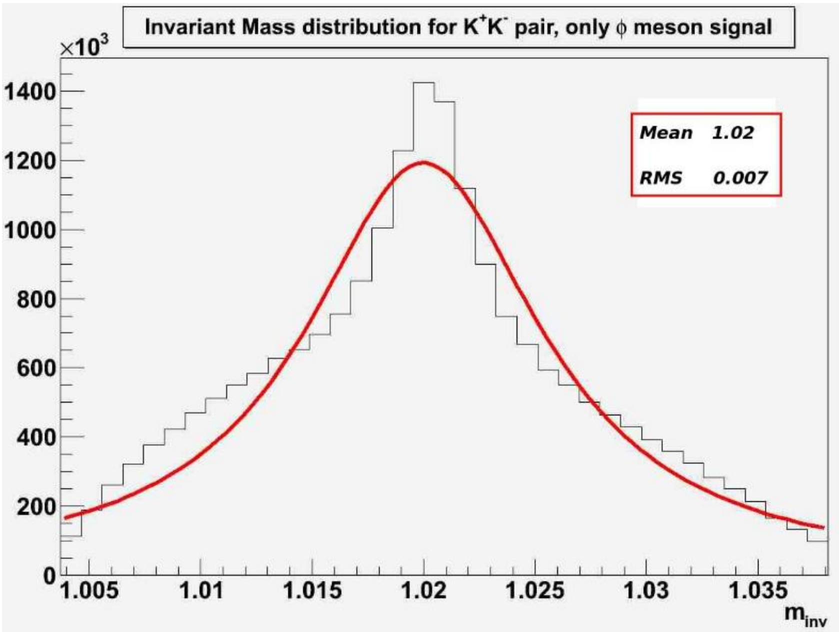

Figure 4.15: Invariant mass distribution for ϕ meson for all the bin of p_T after the cut of the background.

$v_{s,2} = sin2(\phi - \Psi_R)$ distributions can be measured and fitted in a similar manner to ensure that the expected identities, $v^b_{s,2} = 0$ and $v^\phi_{s,2} = 0$, hold.
Figures 4.17 and 4.18 illustrates the method by presenting the fits to the $v_2 = cos2(\phi - \Psi_R)$ (left panel) and $v_{s,2} = sin2(\phi - \Psi_R)$ (right panel) distributions for a bin in p_T. The right panel illustrates the identity, $v^\phi_{s,2} = 0$ for the same p_T bin.

The measured values for ϕ meson elliptic flow for three p_T bins, performed on the sample described in section 4.5, are:

p_T(GeV/c)	[0.5,1[	[1, 2]	[2,3[
v_2	0.021	0.038	0.057
error on v_2	0.003	0.005	0.008

The comparison between this estimate and the generated value, as extrapolated in section 4.8.1 are shown in Fig. 4.16.

Figure 4.16: v_2 measurement (red square) extrapolated for three p_T bin compared with the same measure extrapolated from generated azimuthal angle of phi mesons (green square).

The analysis on a MC sample have produced a result that is consistent, within errors, with the introduced value of v_2 in the simulation, as a consequence this method and the tools that have been developed for this analysis will be used when experimental *Pb-Pb* collisions data will be collected with ALICE experiment at LHC in order to measure ϕ-meson elliptic flow as signature for QGP formation.

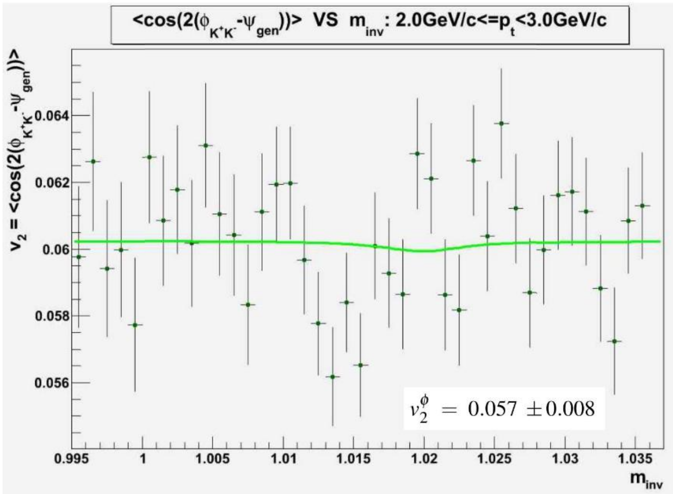

Figure 4.17: $v_2 = cos2(\phi - \Psi_R)$ distributions for $2 \leq p_T < 3GeV/c$: the fit has been performed in order to extrapolate the v_2 for ϕ meson.

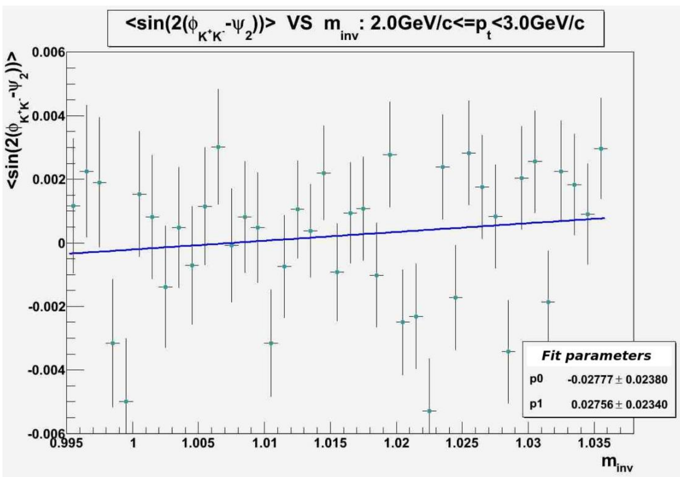

Figure 4.18: $v_{s,2} = sin2(\phi - \Psi_R)$ distributions with a linear fit.

Conclusion

The work of this thesis has been focused to the set up of appropriate the tools in order to measure ϕ meson elliptic flow, v_2 , with the aim of learning more about the characteristics of the medium that could be create in *Pb-Pb* collisions at LHC.
In order to do this, the ALICE Time-Of-Flight (TOF) detector performance in term of Particle Identification will play an important role in the identification of kaons, through which will be possible to reconstruct the behaviour of ϕ mesons products after the collisions.
The TOF detector has been constructed and is presently fully installed and operative at ALICE experimental site. During the construction a wide set of tests has been carried out on the apparatus to guarantee its optimal performance and to acquire a deep experience in the detector characteristics and functioning.
A preliminary study on cosmic-ray track matching with the TOF detector signals, collected during the commissioning runs in 2007 and 2008, shows the good performance of the apparatus.
Considering the estimated efficiency of this apparatus during the approaching Pb-Pb collisions runs, a preliminary study for ϕ-meson elliptic flow measurement on a MC sample has been performed; the results are fully consistent with the expectations.
Therefore, it's possible to conclude that the tools developed in this thesis work are ready to be used to measure ϕ meson elliptic flow when data, coming from *Pb-Pb* collisions, will be collected with ALICE experiment at LHC.

Bibliography

[1] C. Amsler *et al.* [Particle Data Group], Review of particle physics, *Phys. Lett.* B 667 (2008) 1.

[2] D. H. Perkins, Introduction to High-Energy Physics, 4th edition, Cambridge University Press (2000).

[3] P. W. Higgs, Broken Symmetries and the Masses of Gauge Bosons, *Phys. Rev. Lett.* 13 (1964) 508.

[4] F. Englert and R. Brout, Broken Symmetry and the Mass of Gauge Vector Mesons, *Phys. Rev. Lett.* 13 (1964) 321.

[5] G. S. Guralnik, C. R. Hagen and T. W. B. Kibble, Global Conservation Laws and Massless Particles, *Phys. Rev. Lett.* 13 (1964) 585.

[6] H. Fritzsch, M. Gell-Mann and H. Leutwyler, *Phys. Lett.* B47, (1973) 365.

[7] D. J. Gross and F. Wilczek, *Phys. Rev. Lett.* 30 (1973) 1343; Phys. Rev. D8 (1973) 3633.

[8] H. D. Politzer, *Phys. Rev. Lett.* 30 (1973) 1346.

[9] M. Gell-Mann, The Eightfold Way: A Theory of Strong Interaction Symmetry, DOE Technical Report, March 15, 1961.

[10] S. Bethke, The 2009 World Average of α_s, *Eur. Phys. J.*C64: 689-703,2009.

[11] R. Gupta, Introduction to Lattice QCD, arXiv: hep-lat/9807028v1.

[12] O. Aharony, S. S. Gubser, J. Maldacena, H. Ooguri and Y. Oz, Large N Field Theories, String Theory and Gravity, *Phys. Rept.* 323:183-386,2000.

[13] R. K. Ellis, W. J. Stirling and B. R. Webber, QCD and collider physics, Cambridge University Press, 2003.

[14] Y. Aoki, Z. Fodor, S. D. Katz and K. K. Szabo, The QCD transition temperature: Results with physical masses in the continuum limit, *Phys. Rev. Lett.* B 643 (2006) 46.

[15] M. Cheng *et al.*, The transition temperature in QCD, *Phys. Rev.* D 74 (2006) 054507.

[16] A. Chodos, R. L. Jaffe, K. Johnson, C. B. Thorn and V. F. Weisskopf, *Phys. Rev.* D9, 3471 (1974).

[17] C. Y. Wong, Introduction to high-energy heavy ion collisions (World Scientific, Singapore, 1994).

[18] J. F. Grosse-Oetringhaus, Measurement of the Charged-Particle Multiplicityin Proton-Proton Collisions with the ALICE Detector, PhD Thesis, 2009.

[19] PHENIX Collaboration, Formation of dense partonic matter in relativistic nucleus-nucleus collisions at RHIC: Experimental evaluation by the PHENIX collaboration, *Nucl.Phys.* A757:184-283, 2005.

[20] H. Satz, *Rept. Prog. Phys.* 63, 1511 (2000), [hep-ph/0007069].

[21] M. Nguyen, Two Particle Correlations with Direct Photon and π^0 Triggers in 200 GeV p+p and Au+Au Collisions, PhD Thesis, 2009.

[22] J. D. Bjorken, Highly relativistic nucleus-nucleus collisions: The central rapidity region, *Phys. Rev.* D, Vol. 27, No.1 (1983) 140-150.

[23] U. Heinz, The Little Bang: Searching for quark-gluon matter in relativistic heavy-ion collisions, arXiv:hep-ph/0009170v2.

[24] H. Satz, The Search for the QGP: A Critical Appraisal, *Nucl.Phys.Proc.Suppl.* 94 (2001) 204-218.

[25] E. V. Shuryak, *Phys. Lett.* 78 B (1978) 150.

[26] K. Kajantie and H. I. Miettinen, Z. *Phys.* C 9 (1981) 341.

[27] J. D. Bjorken, Fermilab-Pub-82/59-THY (1982) and Erratum, unpublished.

[28] R. Baier, D. Schiff, B. G. Zakharov, *Ann. Rev. Nucl. Part. Science*, Vol.50 (2000) 37-69.

[29] T. Matsui and H. Satz, *Phys. Lett.* 178B (1986) 416.

[30] D. Kharzeev and H. Satz, *Phys. Lett.* B 334 (1994) 155.

[31] R. Pisarski, *Phys. Lett.* B 110 (1982) 155.

[32] V. Bernard *et al.*, *Phys. Lett.* 227 B (1989) 465.

[33] G. E. Brown *et al.*, *Phys. Rev.* C 43 (1991) 1881.

[34] J. Rafelski and B. M*ü*ller, *Phys. Rev. Lett.* 48 (1982) 1066.

[35] J. Rafelski, *Phys. Reports* 88 (1982) 331.

[36] J. Rafelski, *Phys. Lett.* B 262 (1991) 153.

[37] L. Van Hove, *Phys. Lett.* B 118 (1982) 138.

[38] M. Kataja *et al.*, *Phys. Rev.* D 34 (1986) 811 and 2755.

[39] K. J. Eskola, On predictions of the first results from RHIC, *Nucl.Phys.* A698 (2002) 78-87.

[40] L. Evans and P. Bryant, LHC Machine, *J. Inst.* 3, S08001 (2008).

[41] K. Aamodt *et al.*, (ALICE Collaboration), The ALICE experiment at the CERN LHC *J. Instrum.* 3, S08002 (2008).

[42] K. Aamodt *et al.*, (**ALICE** Collaboration), First proton-proton collisions at the LHC as observed with the ALICE detector: measurement of the charged-particle pseudorapidity density at $\sqrt{s}$ = 900 GeV, *Eur. Phys. J.* C (2010) 65: 111-125.

[43] K. Aamodt *et al.* (**ALICE** Collaboration) Charged-particle multiplicity measurement in proton-proton collisions at $\sqrt{s}$ = 0.9 and 2.36 TeV with ALICE at LHC, arXiv:1004.3034v2 (2010)

[44] G. J. Alner *et al.*, (UA5 Collaboration), *Z. Phys.* C 33, 1 (1986).

[45] K. Alpgard *et al.*, (UA5 Collaboration), *Phys. Lett.* B 112, 183 (1982).

[46] M. Ambrosio *et al.*, AIP Conf. Proc. 85, 602 (1982).

[47] W. Thome *et al.*, Nucl. Phys. B 129, 365 (1977); C. Albajar *et al.*, (UA1 Collaboration), *Nucl. Phys.* B 335, 261 (1990); G. J. Alner *et al.*, (UA5 Collaboration), *Phys. Rep.* 154, 247 (1987); F. Abe *et al.*, (CDF Collaboration), *Phys. Rev.* D 41, 2330 (1990).

[48] J. Cleymans and K. Redlich, Chemical and thermal freeze-out parameters from 1-A-GeV to 200-A-GeV, *Phys. Rev.* C60 (1999) 054908, nucl-th/9903063; P. Braun-Munzinger, D. Magestro, K. Redlich and J. Stachel, Hadron production in Au Au collisions at RHIC, *Phys. Lett.* B518 (2001) 41-46, hep-ph/0105229; N. Xu and M. Kaneta, Hadron freeze-out conditions in high energy nuclear collisions, *Nucl. Phys.* A698 (2002) 306-313, nucl-ex/0104021.

[49] J. Adams *et al.*, (**STAR** Collaboration), Experimental and theoretical challenges in the search for the quark gluon plasma: The STAR collaborations critical assessment of the evidence from RHIC collisions, *Nucl. Phys.* A757 (2005) 102-183.

[50] J. Cleymans, B. K*ä*mpfer, M. Kaneta, S. Wheaton and N. Xu, Centrality dependence of thermal parameters deduced from hadron multiplicities in Au + Au collisions at $\sqrt{s_{NN}}$ = 130 GeV, *Phys. Rev.* C71 (2005) 054901, hep-ph/0409071.

[51] P. Braun-Munzinger, K. Redlich and J. Stachel, Particle production in heavy-ion collisions, Quark gluon plasma 3, World Scientific Publishing (2004), arXiv: nucl-th/0304013.

[52] (**STAR** Collaboration) and O. Y. Barannikova, Probing collision dynamics at RHIC, nucl-ex/0403014.

[53] K. Adcox *et al.*, (**PHENIX** Collaboration), Formation of dense partonic matter in relativistic nucleus nucleus collisions at RHIC: Experimental evaluation by the PHENIX collaboration, *Nucl. Phys.*. A757 (2005) 184-283.

[54] B. I. Abelev *et al.* (**STAR** Collaboration), Identified particle production, azimuthal anisotropy, and interferometry measurements in Au+Au collisions at $\sqrt{s_{NN}}$ = 9.2 GeV, *Phys. Rev.* C 81 (2010) 24911.

[55] E. Schnedermann, J. Sollfrank and U. W. Heinz, Thermal phenomenology of hadrons from 200-A/GeV S+S collisions, *Phys. Rev.* C48 (1993) 2462-2475, nucl-th/9307020.

[56] S. A. Bass and A. Dumitru, *Phys. Rev.* C61 (2000) 064909.

[57] H. van Hecke, H. Sorge and N. Xu, *Phys. Rev. Lett.* 81 (1998) 5764.

[58] A. Dumitru and S. A. Bass, *Phys. Lett.* B460 (1999) 411.

[59] J. Adams *et al.*, [(**STAR** Collaboration) *Phys. Rev. Lett.* 92, (2004) 182301.

[60] P. Braun-Munzinger, J. Stachel, J. Wessels and N. Xu, *Phys. Lett.* B344 (1995) 43.

[61] P. Braun-Munzinger, I. Heppe and J. Stachel, *Phys. Lett.* B465 (1999) 15.

[62] S. A. Bass *et al.*, *Phys. Rev.* C60 (1999) 021902.

[63] E. L. Feinberg, Direct Production of Photons and Dileptons in Thermodynamical Models of Multiple Hadron Production, *Nuovo Cimento* A 34, 391 (1976).

[64] T. Peitzmann and M. H. Thoma, Direct Photons from Relativistic Heavy-Ion Collisions, *Phys.Rept.* 364 (2002) 175-246.

[65] F. Fleuret, Recent RHIC results on photon, dilepton and heavy quarks, X Whorkshop on High Energy Physics Phenomenology , Jan 2-13, 2008.

[66] M. C. Abreu *et al.*, *Phys. Lett.* B477 (2000) 28.

[67] A. Capella, E. G. Ferreiro and A. B. Kaidalov, *Phys. Rev. Lett.* 85 (2000) 2080; A. Capella, A. B. Kaidalov, and D. Sousa, *Phys. Rev.* C65 (2002) 054908.

[68] G. Usai *et al.*, (**STAR** NA60 Collaboration), *Eur. Phys. J.* C 43, 415 (2005).

[69] R. Arnaldi *et al.*, (**STAR** NA60 Collaboration), J/Ψ Production in Indium-Indium Collisions at 158 GeV=Nucleon, *Phys. Rev. Lett.* 99, 132302 (2007).

[70] A. Adare *et al.*, *Phys. Rev. Lett.* 98, 232301 (2007).

[71] M. C. Abreu *et al.*, *Phys. Lett.* B 499, 85 (2001).

[72] H. Satz, J. Phys. G 32, R25 (2006); F. Karsch, D. Kharzeev and H. Satz, *Phys. Lett.* B 637, 75 (2006).

[73] P. Braun-Munzinger and J. Stachel, *Phys. Lett.* B 490, 196 (2000).

[74] L. Grandchamp and R. Rapp, *Phys. Lett.* B 523, 60 (2001).

[75] M. I. Gorenstein *et al.*, *Phys. Lett.* B 524, 265 (2002).

[76] R. L. Thews, M. Schroedter and J. Rafelski, *Phys. Rev.* C 63, 054905 (2001).

[77] M. Asakawa *et al.*, *Prog. Part. Nucl. Phys.* 46, 459 (2001); M. Asakawa and T. Hatsuda, *Phys. Rev. Lett.* 92, 012001 (2004); S. Datta *et al.*, *Phys. Rev.* D 69, 094507 (2004).

[78] H. Liu, K. Rajagopal and U. A. Wiedemann, *Phys. Rev. Lett.* 182301 (2007).

[79] T. Gunji *et al.*, *J. Phys.* G 35, 104137 (2008).

[80] A. Adare *et al.*, *Phys. Rev. Lett.* 101, 122301 (2008).

[81] L. Ruan (for the **STAR** Collaboration), Production and energy loss of strange and heavy quarks, arXiv: 1001.3347v1 [nucl-ex] (2010).

[82] S. Wicks *et al.*, *Nucl. Phys.* A 784, 426 (2007).

[83] A. Adil and I. Vitev, *Phys. Lett.* B 649, 139 (2007).

[84] D. d'Enterria, Jet quenching, arXiv: 0902.2011v2 [nucl-ex].

[85] M. Gyulassy and M. Plumer, *Phys. Lett.* B243, 432 (1990); X. N. Wang and M. Gyulassy, *Phys. Rev. Lett.* 68, 1480 (1992).

[86] D. A. Appel, *Phys. Rev.* D 33, 717 (1986); J. P. Blaizot, L. D. McLerran *Phys. Rev.* D 34, 2739 (1986).

[87] A. Adare *et al.*, (**PHENIX** Collaboration), *Phys. Rev.*. C 77, 011901 (2008).

[88] A. Adare *et al.*, (**PHENIX** Collaboration), *Phys. Rev.*. C 78, 014901 (2008).

[89] C. Adler *et al.*, (**STAR** Collaboration), *Phys. Rev. Lett.* 90, 082302 (2003).

[90] C. A. Salgado and U. A. Wiedemann, *Phys. Rev. Lett.* 93, 042301 (2004); N. Borghini and U. A. Wiedemann, arXiv: hep-ph/0506218; N. Armesto, L. Cunqueiro and C. A. Salgado, arXiv: 0809.4433 [hep-ph]; N. Armesto, C. Pajares and P. Quiroga-Arias, arXiv: 0809.4428 [hep-ph]; R. Perez-Ramos, arXiv:0811.2418 [hep-ph]; R. Perez-Ramos, arXiv:0811.2934 [hep-ph].

[91] H. Satz, Color Screening and Quark Deconfinement in Nuclear Collisions, *Adv. Ser. Direct. High-Energy Phys.* 6 (1990) 593.

[92] B. I. Abelev *et al.*, (**STAR** Collaboration), Enhanced strange baryon production in Au+Au collisions compared to p+p at $\sqrt{s_{NN}}$= 200 GeV, *Phys. Rev.* C77, 044908, (2008).

[93] J. Rafelski and J. Letessier, *J. Phys. Conf. Ser.* 50, 176-191 (2006).

[94] G. G. Barnafoldi *et al.*, *J. Phys. G35*, 044057 (2008).

[95] S. Margetis *et al.*, *Ann Rev. Nucl. Part. Sci.* 50 (2000).

[96] M. K. Mitrovski *et al.*, Strangeness production at SPS energies, *J. Phys.*, G32 (2006).

[97] E. Andersen *et al.*, Strangeness enhancement at mid-rapidity in Pb Pb collisions at 158 A GeV/c. *Phys. Lett.*, B449 (1999).

[98] G. E. Bruno, NA57 main results, *J. Phys.*, G35 (2008) 044005.

[99] A. Tounsi and K. Redlich, Strangeness enhancement and canonical suppression (2007), arXiv: hep-ph/0111159.

[100] J. Rafelski, Strange and hot matter, *Nucl. Phys.*, A544 (1992).

[101] N. Armesto, Predictions for the Heavy-Ion Programme at the Large Hadron Collider, arXiv: 0903.1330 (2009).

[102] N. Ahmad *et al.*, (ALICE Collaboration), preprint CERN/LHCC 1995-071.

[103] N. Armesto and C. Pajares, *Int. J. Mod. Phys.* A 15 (2000) 2019.

[104] P. F. Kolb and U. W. Heinz, Hydrodynamic description of ultrarelativistic heavy-ion collisions, in Quark gluon plasma 3, World Scientific Publishing (2004), arXiv: nucl-th/0305084.

[105] The **ALICE** Collaboration, Alignment of the ALICE Inner Tracking System with cosmic-ray tracks, *J. Inst.* 5 P03003 (2010).

[106] http://aliceinfo.cern.ch.

[107] The **ALICE** Collaboration, TPC Technical Design Report, CERN-LHCC-2000-001, 2000; H. R. Schmidt, The ALICE Time Projection Chamber, CERN-ALICE-PUB-2002-027, 2002.

[108] The **ALICE** Collaboration, Technical Design Report of the Transition-Radiation Detector, CERN/LHCC/2001-21.

[109] M. Kweona for the ALICE TRD Collaboration, The Transition Radiation Detector for ALICE at LHC, *Nucl.Phys.* A830: 535c-538c, 2009.

[110] The **ALICE** Collaboration, Technical Design Report of the High-Momentum Particle Identification Detector, CERN/LHCC/1998-19.

[111] A. Di Mauro, 2000 CERN-EP-2000-58.

[112] F. Carminati *et al.*, *J. Phys. G. Nucl. Part. Phys.* 30 (2004) 1517.

[113] A. Rimai *et al.*, ALICE Internal Note, ALICE-INT-1997-23; R. Wurzinger, Y. Le Bornec and N. Willis, ALICE Internal Note, ALICE-INT-1997-10.

[114] D. K. Swoboda *et al.*, Proceedings of the 19th International Conference on Magnet Technology Genua, Italy, IEEE Trans. on Applied.

[115] http://aliceinfo.cern.ch/Offline.

[116] F. Carminati, C. W. Fabjan, L. Riccati and H. de Groot, ALICE computing: Technical Design Report (CERN, Geneva, 2005), CERN-LHCC-2005-018.

[117] http://root.cern.ch/.

[118] T. Sjostrand, L. Lonnblad and S. Mrenna, hep-ph/0108264.

[119] M. Gyulassy and X. N. Wang, Comput. Phys. Commun. 83, 307 (1994), [nucl-th/9502021].

[120] R. Brun, F. Bruyant, M. Maire, A. C. McPherson and P. Zanarini, CERN-DD/EE/84-1.

[121] GEANT4, S. Agostinelli *et al.*, *Nucl. Instrum. Meth.* A506, 250 (2003).

[122] A. Ferrari, P. R. Sala, A. Fass and J. Ranft, FLUKA: A multi-particle transport code (program version 2005) (CERN, Geneva, 2005), CERN-2005-10.

[123] S. Bagnasco *et al.*, AliEn: ALICE environment on the GRID, *J. Phys.*: Conf. Ser. 119 Volume 119 (2008) 062012.

[124] ALICE Coll. Technical Design Report of the Time Of Flight Detector CERN/LHCC/2000-12; Addendum CERN/LHCC/2002-016.

[125] E. Cerron Zeballos *et al.*, 'A new type of resistive plate chamber: the Multigap RPC' , *Nucl. Instrum. Meth.* A374, 132 (1996).

[126] **ALICE** Collaboration *et al.*, ALICE: Physics Performance Report, Volume II,J. *Phys. G. Nucl. Part. Phys.* 32 (2006) 1295.

[127] **ALICE** Collaboration,'Technical Proposal for a large ion collider experiment at the CERN LHC', CERN/LHCC/95-71.

[128] A. Akindinov *et al.*,Particle identification with the ALICE TOF detector at very high particle multiplicity', *Eur. Phys. J.* C32S1(2004).

[129] A. Akindinov *et al.*, Study of QGP signatures with the Phi –> K^+ K^- signal in Pb Pb ALICE events,*Eur. Phys. J.* C45(2004).

[130] S. Radomski *et al.*, ALICE Internal Note 2003-008.

[131] J. Velkovska for the **P**HENIX Collaboration, *Nucl. Phys.* A698 (2002) 507.

[132] F.Noferini, PWG2 meeting@CERN, 27 April 2010.

[133] M. C. S. Williams, 'The multigap RPC: the time-of-flight detector for the ALICE experiment', *Nucl. Instrum. Meth.* A478, 183 (2002).

[134] F. Anghinolfi *et al.*,'NINO: An ultrafast low-power front-end amplifier discriminator for the time-of-flight detector in the ALICE experiment', *Nucl. Instrum. Meth.* A533, 183 (2004).

[135] R. J. Glauber and G. Matthiae, High-energy scattering of protons by nuclei, *Nucl. Phys.* B21 (1970)

[136] P. Shukla, The Glauber model and the heavy ion reaction cross section, *Phys. Rev.* C67 (2003) 054607, nucl-th/0302030.

[137] M. D. Oldenburg for the **STAR** Collaboration, Scaling of anisotropic flow in the picture of quark coalescence, *J. Phys.* G31 (2005) S437S442, nucl-ex/0412001.

[138] J. Adams *et al.*, (**STAR** Collaboration), Azimuthal anisotropy in Au+ Au collisions at $\sqrt{s_{NN}}$ = 200 GeV, *Phys. Rev.* C72 (2005) 014904, nucl-ex/0409033.

[139] S. Adler *et al* (**PHENIX** Collaboration) ,Elliptic flow of identified hadrons in Au + Au collisions at sN N = 200 GeV, *Phys. Rev. Lett.* 91 (2003) 182301, nucl-ex/0305013.

[140] E. Fermi, *Prog. Theor. Phys*. 5, 570 (1950), S. Z. Belenkij and L. D. Landau, *Nuovo Cim.* Suppl. 3S10, 15 (1956)

[141] Kolb P F, Sollfrank J and Heinz, *Phys. Rev.* C 62 054909 (2000)

[142] U. Heinz, Hydrodynamics at RHIC: how well does it work,where and how does it break down?, *J. Phys. G: Nucl. Part. Phys.* 31 (2005)

[143] P. Huovinen,P. F. Kolb,U Heinz,P. V. Ruuskanen and Voloshin *Phys. Lett.* B 503 58, 2001

[144] X. Dong, S. Esumi, P. Sorensen, N. Xu, and Z. Xu, Resonance decay effects on anisotropy parameters,*Phys. Lett.* B597 (2004), nucl-th/0403030.

[145] V. Greco, C. M. Ko and P. L*é*vai, *Phys. Rev. Lett.* 90 202302, 2003 V. Greco, C. M. Ko and P. L*é*vai, *Phys. Rev.* C 68 034904, 2003 R. J. Fries, B. M*ü*ller, C. Nonaka and S. Bass S *Phys. Rev. Lett.* 90 202303, 2003 R. J. Fries, B. M*ü*ller, C. Nonaka and S. Bass *Phys. Rev.* C 68 044902, 2003 D. Molnar and S. Voloshin *Phys. Rev. Lett.* 91 092301, 2003

[146] U. Heinz and S. Wong, *Phys. Rev.* C 66 014907, 2002 D. Teaney, *Phys. Rev.* C 68 034913, 2003

[147] P. Kovtun, D. T. Son and A. Starinets,Viscosity in Strongly Interacting Quantum Field Theories from Black Hole Physics, *Phys. Rev. Lett.* 94 (2005),111601

[148] U. Heinz, The strongly coupled quark-gluon plasma created at RHIC, *J. Phys.* A: Math. Theor. 42 (2009) 214003

[149] J. Adams *et al* (**STAR** Collaboration) *Phys. Rev. Lett.* 92 052302, 2004 S. Adler *et al* (**PHENIX** Collaboration) *Phys. Rev. Lett.* 91 182301, 2003

[150] H. Sorge, Flavor Production in Pb(160AGeV) on Pb Collisions: Effect of Color Ropes and Hadronic Rescattering,*Phys. Rev.* C52 (1995), nucl-th/9509007.

[151] M. Bleicher *et al.*, Relativistic hadron hadron collisions in the ultra-relativistic quantum molecular dynamics model,*J. Phys.* G25(1999), hep-ph/9909407.

[152] M. Bleicher and H. Stöcker, Anisotropic flow in ultra-relativistic heavy ion collisions,*Phys. Lett.* B526 (2002), hep-ph/0006147

[153] Y .Lu *et al.*, Anisotropic flow at RHIC: How unique is the number-of-constituent-quark scaling?,*J. Phys.* G32 (2006), nucl-th/0602009.

[154] A. M. Poskanzer and S. A. Voloshin, Methods for analyzing anisotropic flow in relativistic nuclear collisions, *Phys. Rev.* C 58, 1671 (1998)

[155] P. Danielewicz and G. Odyniec, *Phys. Lett.* 157B, 146 (1985)

[156] J. Ollitrault, Anisotropy as a signature of transverse collective flow, *Phys. Rev.* D46 (1992) 229-245.

[157] W. M. Yao *et al.*, The Review of Particle Physics, *J. Phys.* G 33 (2006) 1.

[158] A. Shor, Phi Meson Production As a Probe of the Quark Gluon Plasma, *Phys. Rev. Lett.* 54 (1985) 1122-1125.

[159] T. Ishikawa *et al.*, Phi photo-production from Li, C, Al, and Cu nuclei at E(gamma) = 1.5-GeV - 2.4-GeV, *Phys. Lett.* B608 (2005) 215-222, nucl-ex/0411016.

[160] A. Sibirtsev, H. W. Hammer, U. G. Meissner, and A. W. Thomas, Phi-meson photoproduction from nuclei, *Eur. Phys.* J. A29 (2006) 209-220, nucl-th/0606044.

[161] J. Adams *et al.*, (**STAR Collaboration**), Phi meson production in Au+Au and p+p collisions at $\sqrt{s_{NN}}$ = 200 GeV, *Phys. Lett.* B612 (2005) 181-189, nucl-ex/0406003.

[162] J. Adams *et al.*, (**STAR Collaboration**), Multi-strange baryon elliptic flow in Au + Au collisions at $\sqrt{s_{NN}}$ = 200 GeV, *Phys. Rev. Lett.* 95 (2005) 122301, nucl-ex/0504022.

[163] J. Adams *et al.*, (**STAR Collaboration**),Partonic Flow and ϕ-Meson Production in Au+Au Collisions at $\sqrt{s_{NN}}$=200 GeV, *Phys. Rev. Lett.*. 99, 112301 (2007)

[164] N. Borghini and J. Y. Ollitrault, Azimuthally sensitive correlations in nucleus nucleus collisions, *Phys. Rev.* C70 (2004) 064905, nucl-th/0407041.